

*"I guess our wishes don't do dishes, or brake repairs.  
Make them something somebody can use."*

*The Weakerthans*



**University of Alberta**

**Optical Characterization of Thin Films Produced by Glancing Angle Deposition Using  
Spectroscopic Ellipsometry**

by

**James Paul Gospodyn**



**A thesis submitted to the Faculty of Graduate Studies and Research  
in partial fulfillment of the requirements for the degree of**

**Doctor of Philosophy  
in  
Electromagnetics, Photonics, and Plasmas**

**Department of Electrical and Computer Engineering**

**Edmonton, Alberta  
Spring 2008**



Library and  
Archives Canada

Published Heritage  
Branch

395 Wellington Street  
Ottawa ON K1A 0N4  
Canada

Bibliothèque et  
Archives Canada

Direction du  
Patrimoine de l'édition

395, rue Wellington  
Ottawa ON K1A 0N4  
Canada

*Your file* *Votre référence*  
*ISBN: 978-0-494-45438-1*  
*Our file* *Notre référence*  
*ISBN: 978-0-494-45438-1*

**NOTICE:**

The author has granted a non-exclusive license allowing Library and Archives Canada to reproduce, publish, archive, preserve, conserve, communicate to the public by telecommunication or on the Internet, loan, distribute and sell theses worldwide, for commercial or non-commercial purposes, in microform, paper, electronic and/or any other formats.

The author retains copyright ownership and moral rights in this thesis. Neither the thesis nor substantial extracts from it may be printed or otherwise reproduced without the author's permission.

**AVIS:**

L'auteur a accordé une licence non exclusive permettant à la Bibliothèque et Archives Canada de reproduire, publier, archiver, sauvegarder, conserver, transmettre au public par télécommunication ou par l'Internet, prêter, distribuer et vendre des thèses partout dans le monde, à des fins commerciales ou autres, sur support microforme, papier, électronique et/ou autres formats.

L'auteur conserve la propriété du droit d'auteur et des droits moraux qui protègent cette thèse. Ni la thèse ni des extraits substantiels de celle-ci ne doivent être imprimés ou autrement reproduits sans son autorisation.

---

In compliance with the Canadian Privacy Act some supporting forms may have been removed from this thesis.

Conformément à la loi canadienne sur la protection de la vie privée, quelques formulaires secondaires ont été enlevés de cette thèse.

While these forms may be included in the document page count, their removal does not represent any loss of content from the thesis.

Bien que ces formulaires aient inclus dans la pagination, il n'y aura aucun contenu manquant.

  
**Canada**

## **Abstract**

The glancing angle deposition (GLAD) process produces films with highly porous micro- and nano-structures. Resultant films of suitable materials have many useful optical properties. To optimize these properties, a full characterization of optical GLAD films was performed in this work using spectroscopic and Mueller matrix ellipsometry. GLAD films composed of dielectric, organic, and semiconductor materials were examined first by using spectroscopic ellipsometry to characterize the material itself, followed by an examination of the porous GLAD films. Since these films are composed of a mixture of air and material, they must be described using effective medium approximations. By applying appropriate effective medium approximations, film parameters such as the indices of refraction, the birefringence, and film density as a function of deposition angle could be examined for a variety of materials in a number of GLAD film structures. These characterization techniques were then used to examine index of refraction gradients within GLAD films composed of vertical columns using dynamic effective medium theory that accounts for finite wavelength effects. Further studies using these techniques were applied to an examination of the effect that periodic arrangement of the columns in the substrate plane has on the overall index of refraction of the films. Finally, the aforementioned optical characterization techniques were used to successfully predict the photoluminescent behavior of periodically layered GLAD films composed of photoluminescent  $\text{Y}_2\text{O}_3:\text{Eu}$ .

*To my wife Catherine,  
who had the courage to quit grad school;  
whose action served as a reminder to me that  
just because you can do something,  
doesn't mean that you should.*

## Acknowledgement

I would like to thank my supervisor Dr. Jeremy Sit for giving me the opportunity to perform this work, and giving me the academic freedom to follow my own path in this research. As well, I'd like to thank Jeremy for 'bidding out of his ass' when we had the after-work Bridge matches, which gave Jason and I more than our share of rubbers, and left Nick hanging.

I would also like to thank Dr. Michael Brett principally for helping for always making time to chat with me about various things, and also for providing support for this research.

Next, I would like to thank those that I collaborated with, both officially (through published means) and unofficially (through various discussions over the years) – the PDFs, RAs, and Grad Students in the research group. Thanks to (in the order in which I mentally go through the desks on the first floor, followed by the name list on the Naboozers t-shirt circa 2002 to fill in the gaps): Mike Taschuk, Jim Broughton, Doug Vick, Mike Fleischauer, Nathan Gerein, Matt Hawkeye, Doug Gish, Jason Sorge, Mark Summers, John Steele, Shufen Tsoi, Nick Wakefield, Bryan Szeto, Jonathon Kwan, Sumundu Ferdnarno (spelling as per the online petition), Louis Bezuidenhout, Graeme Dice, Katie Krause, Andy van Popta, Anastasia Elias, Peter Hruday, Mike Colgan, Brian Dick, Ken Harris, Martin Jensen, Scott Kennedy, Greg Kiema, Mary Seto, as well as the numerous summer students throughout the years.

I'd like thank Ben Bathgate for helping out whenever equipment didn't behave, and for suggesting that it's because the equipment doesn't like me, as well as the Machine Shop staff for making my crazy schematics a reality.

Next I'd like to thank the NanoFab staff for their support, and for giving me the opportunity to act as a Trainer on the VASE.

Finally, I'd like to thank my family, who had no particular part in this work, but helped me maintain perspective.



# Table of Contents

1 – Introduction and Background .....	1
1.1 – GLAD Films.....	2
1.2 – The Basics of Ellipsometry .....	8
1.3 – The Mueller Matrix.....	10
1.4 – Effective Medium Approximation.....	15
1.5 – Description of an Anisotropic Stratified Film System .....	21
1.6 – Optical Constant Dispersion .....	26
2 – Experimental Details .....	33
2.1 – The Variable Angle Spectroscopic Ellipsometer Hardware .....	33
2.2 – The Modeling Software and Analysis of Films .....	40
3 – Fundamental Film Examination .....	47
3.1 – Examination of Slanted MgF <sub>2</sub> and SiO <sub>2</sub> Columns .....	47
3.2 – Examination of TiO <sub>2</sub> .....	68
4 – Examination of Organic GLAD Films .....	74
5 – Examination of the Index Gradient.....	86
5.1 – Adsorption of Water .....	90
5.2 – Oxygen Depletion of the SiO <sub>2</sub> Source Material .....	91
5.3 – Scanning Electron Micrograph Image Analysis .....	92
5.4 – Optical Modeling Using Finite Wavelength Effects .....	99
6 – Applications to Structured Media .....	103
6.1 – Periodically Arranged Columnar Thin Films.....	103
6.2 – Periodically Layered Luminescent Media .....	115
7 – Summary and Conclusions .....	133
7.1 – Summary.....	133
7.2 – Impact of this Work .....	134
7.3 – Future Work.....	136
References .....	137
Appendices .....	146
Appendix 1 – Maple Calculation for an Anisotropic Film Layer .....	146
Appendix 2 – Kramers-Kronig Analysis for a Lorentz Oscillator .....	162

## List of Tables

Table 1 – Mueller matrices for some typical optical elements.....	14
Table 2 – Semi-empirical parameters for the best-fit least squares fit for the principal indices of refraction as a function of deposition angle. The numbers in parentheses are the $1\sigma$ standard deviation for the parameter. ....	60
Table 3– Empirical parameters to the linear fit for the indices of refraction at deposition angles of $80^\circ$ and higher. The numbers in parentheses are the $1\sigma$ standard deviation for the parameter.....	62
Table 4 – Summary of the physical and optical parameters for the films.....	118

## List of Figures

- Figure 1 – (a) Schematic of the technique used for GLAD deposition. (b) Illustration of the columnar film structure with a vapour source at angle  $\alpha$ , and the post growth at angle  $\beta$ ..... 3
- Figure 2 – Structure zone model for evaporated film growth. Adapted from [62]. ..... 4
- Figure 3 – (a) Vertical pillar microstructure by rapid rotation in  $\varphi$  [65], (b) Helical structures formed by a slow rotation in  $\varphi$  [66], (c) Zigzag microstructure by intermittent, rapid rotation in  $\varphi$  [66], and (d) Periodic tetragonal square spirals formed by rapid, intermittent  $90^\circ$  rotations, grown on a “seeded” substrate for controlled spacing of the posts [12]. ..... 7
- Figure 4 – Schematic for various ellipsometer configurations. Adapted from [39]. ..... 9
- Figure 5 – Incident, reflected and transmitted  $p$ - and  $s$ -modes of a plane wave with wavevectors  $k_a$ ,  $k_a'$ ,  $k_f$ , and  $k_f'$ , respectively. Adapted from [61]. .....21
- Figure 6 – Example of Lorentzian dispersion in the dielectric constants  $\varepsilon_1$  (solid) and  $\varepsilon_2$  (dashed) as given by (1.6.6) ..... 29
- Figure 7 – Images of the variable angle spectroscopic ellipsometer (a) and the controller computer and light source/monochromator (b)..... 34
- Figure 8 – Experimental (dashed) and theoretical (solid) spectrum for the (3,4)th element of the Mueller matrix for a zero-order quarter-wave plate designed with a quarter wave retardation at 633 nm. .... 39
- Figure 9 – Parameter window for evaluating films using Cauchy dispersion. .... 42
- Figure 10 – Parameter window for evaluating general oscillators to describe film dispersion..... 43
- Figure 11 – Parameter window used to evaluate the film using the BEMA (a) and the column tilt using Euler rotations (b)..... 44
- Figure 12 – Illustration of guess values for a given parameter of a film illustrating local and global minima to the  $MSE$ . Adapted from [39]. ..... 45
- Figure 13 – Typical model fits (solid and dashed) to the experimental  $\Psi$  (●) and  $\Delta$  (■) using the Cauchy dispersion for the solid films composed of  $MgF_2$  (a) and  $SiO_2$  (b). For the sake of clarity, only every 5<sup>th</sup> experimental data point is shown, and only one angle of incidence is shown ( $60^\circ$  for (a) and  $65^\circ$  for (b))..... 50
- Figure 14 – Resultant optical constants for the solid films composed of  $MgF_2$  (a) and  $SiO_2$  (b) using the evaluation template in Figure 9.....51
- Figure 15 – Scanning electron microscope image of a 1000 nm thick  $MgF_2$  columnar thin film grown at a deposition angle of  $84^\circ$  with respect to substrate

normal (a) and an illustration of the directions of the principal indices of refraction (b). .....	52
Figure 16 – Example of the evaluation templates used to describe (a) MgF <sub>2</sub> films and (b) SiO <sub>2</sub> films. The BrugBiaxial_Tilt layers describe the tilted columns using the anisotropic Bruggemann EMA, the Surface_Rough layer represents the variation in column height, and the SimpleGraded represents the index of refraction gradient in SiO <sub>2</sub> . The thickness, percent material, Euler angles, and index gradient (for SiO <sub>2</sub> films) were set as fit parameters. ....	54
Figure 17 – Comparison between the experimental (●) and generated (-) first 3 rows of the normalized reflection Mueller matrix elements for light incident at an angle of 50° on a MgF <sub>2</sub> GLAD film grown at α = 82° (a) and an SiO <sub>2</sub> film also grown at α = 82° (b). Only every few experimental data points are shown for the sake of clarity. ....	56
Figure 18 – Magnitude of the principal indices of refraction for MgF <sub>2</sub> columnar thin films (a) and at the 50% growth point for SiO <sub>2</sub> columnar thin films (b) as a function of deposition angle. The curves are fits to the semi-empirical law. ....	60
Figure 19 – Magnitude of the principal indices of refraction for MgF <sub>2</sub> columnar thin films (a) and at the 50% growth point for SiO <sub>2</sub> columnar thin films (b) as a function of deposition angle for deposition angles ≥ 80°. The lines are empirical linear fits. ....	62
Figure 20 – Film density in percentage as a function of deposition angle for MgF <sub>2</sub> films (▼), the 50% growth point for SiO <sub>2</sub> films (○), and plotted for comparison are simulated result (see Fig. 8 in reference [64]) for 0 diameter diffusion length (●) and 4 diameter diffusion length (■). Also shown is the curve given by (3.1.1). ....	63
Figure 21– Percentage of MgF <sub>2</sub> with respect to films grown at normal incidence as a function of film thickness as measured by the Bruggeman EMA for films grown at α ≅ 79.5° (●), α ≅ 80° (○), and α ≅ 80.5° (▼) with respect to substrate normal. ....	67
Figure 22 – Thin film density approximations from Tait’s rule (—), thickness ratios (◆), and Bruggemann’s effective medium theory (▲). From reference [16] ©2006 IEEE. ....	68
Figure 23 – Best model fits (solid and dashed) to experimental Ψ (●) and Δ (■) for a solid TiO <sub>2</sub> film using a Gaussian oscillator function. For the sake of clarity, only an angle of incidence of 70° is shown, and only every 5 <sup>th</sup> experimental point is shown. ....	70
Figure 24 – Index of refraction, n (solid), and extinction coefficient, k (dashed), for a solid TiO <sub>2</sub> film based on the Gaussian Oscillator given in (3.2.1). ....	71
Figure 25 – Index of refraction at a wavelength of 500 nm of the as-deposited solid TiO <sub>2</sub> films (●) and treated films (■) as a function of the cumulative thickness deposited. ....	72

Figure 26 – Density of $\text{TiO}_2$ as a function of $\alpha$ .....	73
Figure 27 – Best model fits (solid and dashed) to experimental $\Psi$ (●) and $\Delta$ (■) for a solid $\text{Alq}_3$ film using a Lorentz and Tauc-Lorentz oscillator function. For the sake of clarity, only an angle of incidence of $50^\circ$ is shown, and only every 5 <sup>th</sup> experimental point is shown.....	76
Figure 28 - The index of refraction, $n$ (solid), and the extinction coefficient, $k$ (dashed), for a solid $\text{Alq}_3$ film resultant from the Lorentz and Tauc-Lorentz oscillators given in (4.1).....	76
Figure 29 – Multilayer model of columnar thin film deposited at $\alpha = 71^\circ$ .....	77
Figure 30 – Cross sectional SEM images of tilted columnar thin films deposited at a) $\alpha = 71^\circ$ and b) $\alpha = 85^\circ$ .....	78
Figure 31 – Normalized film density of the biaxial layer as a function of the deposition angle $\alpha$ . The density predicted based on Tait’s rule (solid line) is shown as a guideline. ....	79
Figure 32 – The principal indices of refraction for the biaxial layer of $\text{Alq}_3$ at a wavelength of 525 nm.....	80
Figure 33 – SEM image of silica slanted columnar thin film deposited at $\alpha = 88^\circ$ as viewed along the direction of the columns. The white arrow indicates the direction of the incoming vapor flux. Broadening occurs for individual columns while growth competition is observed as smaller diameter columns are visible in the background. ....	82
Figure 34 – In-plane birefringence, $\Delta n$ , shown as a function of deposition angle $\alpha$ . ....	82
Figure 35 – SEM of the film deposited at $\alpha = 85^\circ$ as viewed along the direction of the columns. The white arrow indicates the direction of the incoming vapour flux. As can be seen, the column cross-sections are predominantly circular in shape. ....	84
Figure 36 – SEM of the film deposited at $\alpha = 67^\circ$ along the direction of the post growth. The white arrow indicates the direction of the incoming vapour flux. Individual columns have merged together modifying the cross-section of the columns and decreasing the number of voids.....	85
Figure 37 – Difference between the generated and experimental data for a 843 nm thick film.....	87
Figure 38 – Index of refraction along the columns at the bottom of the film (solid) and at the top of the film (dash-dot), and the index of refraction in the plane of the substrate at the bottom of the film (dotted) and top of the film (dashed). ....	88
Figure 39 – $\text{SiO}_2$ film produced using the PhiSweep method.....	89
Figure 40 – Index of refraction versus cumulative thickness for normally grown $\text{SiO}_2$ .....	92

Figure 41 – Top-down SEM images of SiO <sub>2</sub> GLAD films composed of vertically aligned with a thickness of (a) 197 nm, (b) 424 nm, (c) 662 nm, (d) 845 nm, (e) 1032 nm, and (f) 1236 nm.....	95
Figure 42 – Histogram of pixel intensity for a top down SEM image shown in the previous figure (Fig. 41a).....	96
Figure 43 - (a) FFT of the top down image for the film in Fig. 41(a), and (b) the radial average of the FFT, with the spatial frequency calculated.....	98
Figure 44 – Comparison of the difference between experimental and theoretical Mueller matrix elements using the standard EMA (a), and a finite wavelength EMA (b) for the film shown in Fig. 41c. ....	101
Figure 45 – SEM image of the seed enhancement layer. ....	107
Figure 46 – An example of the layer modeling of the seed enhancement layer. ....	108
Figure 47– An example of the experimental (dashed) and theoretical (solid) Mueller matrix elements. This example is for the unpatterned region. The matrix element labels are left off for the sake of clarity.....	108
Figure 48 – The indices of refraction $n_e$ (dashed) and $n_o$ (solid) for the seed enhancement layer for (a) the patterned section and (b) the unpatterned section. ....	109
Figure 49 – SEM images of the unpatterned (a) and patterned (b) areas of the first quarter turn of a square spiral using the PhiSweep method. Note that the small chevron-like features are a result of the PhiSweep method.....	110
Figure 50 – Example of the layer modeling for the seed enhancement layer plus a 1/4-turn square spiral. ....	111
Figure 51 – Example of the experimental (dashed) and theoretical (solid) Mueller matrix elements at a 75° angle of incidence for the (a) unpatterned and (b) patterned regions of the PhiSweep grown film. The matrix element labels are left off for the sake of clarity. ....	112
Figure 52 – Optical constants for the unpatterned (a) and patterned (b) sections of the traditional GLAD film and for the unpatterned (c) and patterned (d) regions of the PhiSweep GLAD film. ....	114
Figure 53 – Cross sectional SEM image of a film from set A (a) and set B (b)....	117
Figure 54 – Example of the PL emission spectra, taken from film set A annealed at 800°C. ....	120
Figure 55 – Angular emission profile of film set A (●) and film set B (○) annealed at 800°C on fused silica substrates. The dashed line is an example of a Lambertian emission profile given in arbitrary units. ....	120
Figure 56 – Transmittance of film (a) set A and (b) set B on fused silica substrates as-deposited (dashed) and annealed at 600°C for 1 hour (solid). The arrows indicate the transmission minima. The data for the wavelength range from 200	

nm to 300 nm was measured using a spectrophotometer (Lambda 900 Spectrophotometer, Perkin-Elmer Inc.) .....	123
Figure 57– Optical model layers to describe a film from set A as-deposited. ....	124
Figure 58 – Experimental (●,◆,■,▼) and model (solid line) curves for (a) normalized Mueller matrix data of the as-deposited film from set A on a silicon substrate measured at a reflectance angle of 50°, and (b) the normal incidence transmissivity for the as-deposited film from set A on a fused silica substrate. For the sake of clarity, the $M_{ij}$ elements near zero were not shown, and only every second experimental data point is shown. ....	126
Figure 59 – Experimental Psi (●) and Delta (○) and with best model fits (solid and dashed lines) for a 69 nm thick $Y_2O_3:Eu$ film deposited at $\alpha = 0^\circ$ annealed at 600°C. Only every 5 <sup>th</sup> experimental point and only an angle of incidence of 70° is shown for the sake of clarity. Also shown (inset) is the resultant $n$ (solid) and $k$ (dashed) using Cauchy and Urbach dispersion.....	128
Figure 60 – Model (-) and experimental (●) transmission of film set A on fused silica after annealing at 600°C.....	129
Figure 61 – Charge transfer band intensity for nano-crystalline $Y_2O_3:Eu$ as a function of wavelength as quoted by Igarishi <i>et al</i> [129]. The inset is the complete band as a function of energy (●) with a Tauc-Lorentz oscillator function[90, 91] applied to it (solid).....	129
Figure 62 - Angular emission pattern for films from set A (●) along with the predicted angular emission pattern from the model (solid) with a correction factor accounting for the laser incidence angle.....	131
Figure 63 - Predicted angular emission pattern for films from set A using the model assuming the excitation source is normally incident for all emission angles. ....	132

# **1 – Introduction and Background**

Thin films produced by glancing angle deposition (GLAD) have been shown by numerous researchers to have interesting and useful physical properties [1-18]. Among these many physical properties is an assortment of optical properties [19-36], such as chiral optical filters, Bragg resonances, and polarized luminescent emission. To optimize the optical properties of GLAD films, studies must be performed on their optical constants, leading to optical descriptions of GLAD-produced films.

Variable angle spectroscopic ellipsometry (VASE) provides highly precise optical data [37-45] on the polarization state changes introduced by an optical system. This can be used for analyzing key parameters of thin films such as index of refraction, extinction coefficient, and thickness, as well as more complicated parameters such as optical dispersion of the film, birefringence, and film structure [23, 46-50]. The key to this technique is that it relies on the acquisition of data for many different wavelengths of light, and for many angles of light incidence, which overcomes many of the problems associated with single wavelength, single incidence angle ellipsometry [38-40].

In this study, spectroscopic ellipsometry techniques were used to characterize GLAD-produced films. The theoretical framework for the description of these films arises from effective medium approximations (EMA) [51-56] and the usage of Berreman's method [57-61] to describe optical film systems. Also examined is the theory behind optical constant dispersion and the usage of various dispersion relations to describe optical media.



This framework is then applied to both inorganic and organic columnar films produced by GLAD, as well as an examination of the subtle properties of index gradients within GLAD columns. An extension to this work allows the study of the effect that periodically arranging GLAD columns on a substrate has on the global optical constants. Application of the ellipsometric models was demonstrated in the prediction of the photoluminescent emission patterns of periodically layered photoluminescent GLAD films.

### **1.1 – GLAD Films**

The following section will discuss the basics of GLAD films, briefly describing the underlying basis for growth of GLAD films in the formalism of the structure zone model, and, as well, will highlight the basic technique and provide examples of some of the types of structures that can be fabricated.

In the GLAD technique, the substrate is mounted such that the incoming particle flux arrives at the substrate at an angle  $\alpha$ , typically between  $75^\circ$  and  $85^\circ$  with respect to substrate normal, as illustrated in Fig. 1(a). The fundamentals behind the growth of GLAD films can be broken into two regimes. The first regime is the nucleation and seeding regime, which typically occurs within the first 100 nm of vertical film growth. In this regime, adatoms from the source impinge and condense on the surface of the substrate and form nuclei. Since the substrate is “cold” with respect to the melting or sublimation point of the source material, the adatoms “stick” to the surface and have low mobility in the plane of the substrate, with the initial seed sizes relating to the adatom mobility [17]. As the film continues to grow, the oblique angle of flux incidence results in

shadowed regions adjacent the nuclei opposite the direction of the incoming flux. This atomic shadowing cause any additional flux to impinge preferentially onto the existing nuclei and due to limited adatom mobility the added flux remains on the initial nuclei, causing column growth. As the initial nucleation layer reaches its final stages of growth, the overall film density reaches a quasi-equilibrium value [17], which occurs through the extinction of columns. The end result of these growth mechanisms is that the films become highly porous, and are composed of posts that grow towards the vapor source at an angle  $\beta$  with respect to substrate normal, illustrated in Fig. 1(b).

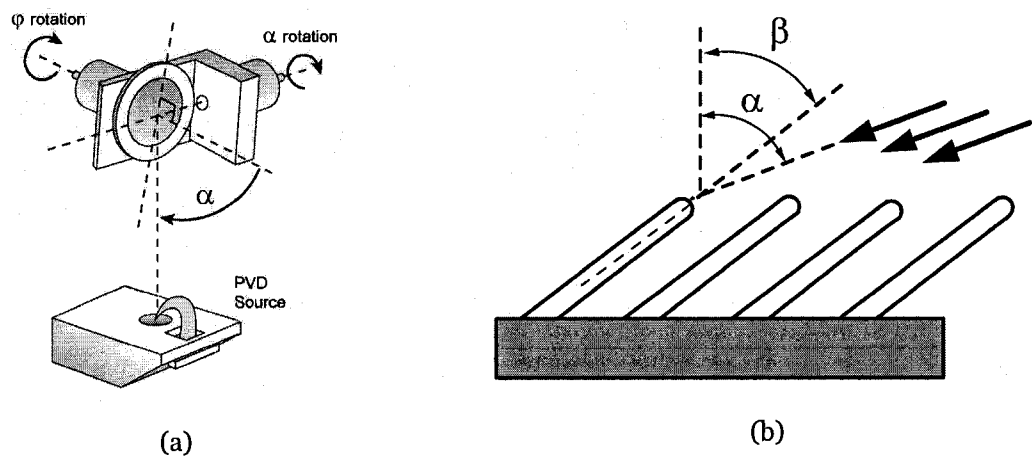


Figure 1 – (a) Schematic of the technique used for GLAD deposition. (b) Illustration of the columnar film structure with a vapour source at angle  $\alpha$ , and the post growth at angle  $\beta$ .

It is important to note here that  $\alpha \neq \beta$  and, specifically,  $\beta > \alpha$ . This inequality at first appears counter-intuitive, however, if  $\alpha$  were equal to  $\beta$ , then no atomic shadowing would occur, and thus the individual pillars would not form.

The deposition resulting in individual columns is characteristic of Zone 1 growth in the structure zone model [62, 63] for physical vapor deposition. Briefly, there are three zones for deposition by evaporation, shown in Fig. 2, with

film structure dependent on ratio  $T/T_m$ , where  $T$  is the substrate temperature, and  $T_m$  is the temperature at which the source material melts (or sublimes). Zone 1 is characterized by tapered columns with domed tops and separated by voids. The crystal structure of the material is poorly defined. Zone 1 structure occurs when adatom diffusion is insufficient to overcome the effects of shadowing. Further, the shadowing causes voids to form in the film since the domed tops of the films receive more material flux than the adjacent areas near the column does, especially when depositing at oblique angles of incidence. Zone 1 film growth occurs when  $T/T_m \approx 0.3$ , which has been determined empirically [62].

Films grown in Zone 2, occurring when  $0.3 \approx T/T_m \approx 0.5$ , are characterized by having columnar grains separated by distinct intercrystalline boundaries. The surface of the film is smooth, unlike those grown in Zone 1, as surface diffusion has a significant role in film growth within this regime. Finally, for films grown in Zone 3, which occurs when  $T/T_m \approx 0.5$ , film growth is characterized by equiaxed grains, and is dominated by bulk surface diffusion.

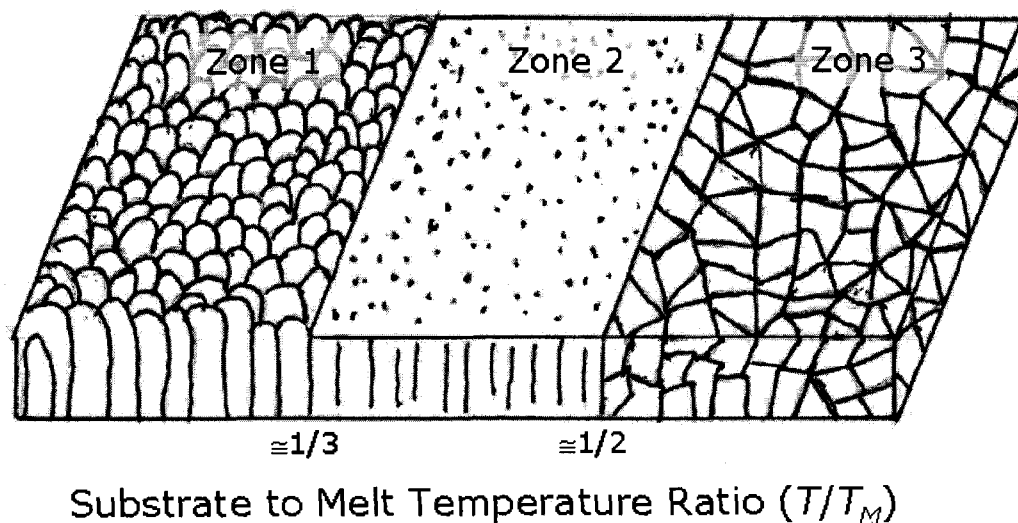


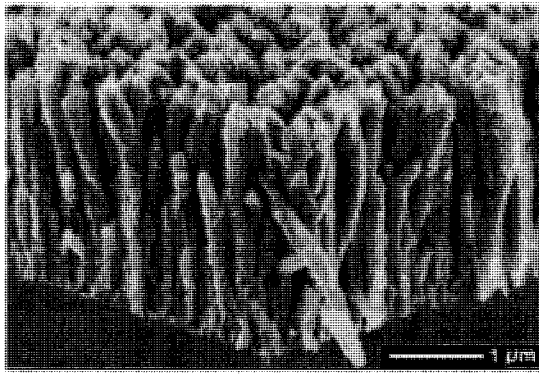
Figure 2 – Structure zone model for evaporated film growth. Adapted from [62].

Historically, growing films in Zone 1 was not desirable since it resulted in poor crystallinity, low density, and a large degree of surface roughness inherent in its growth. However, the GLAD technique takes advantage of the perceived non-idealities present in Zone 1 growth. To do this, one aligns the deposition angle,  $\alpha$ , at angles that are oblique with respect to the source material. In the first few nanometres of growth, nuclei of the evaporant are formed on the substrate at random locations. Since adatom diffusion is very low, the nuclei ‘stick’ to the surface and tend not to coalesce with their neighbours. This creates regions on the substrate where no film material is present. As more material is added, the material preferentially collects on the nuclei that were formed at the beginning of the film growth, while the voids are shadowed by the original nuclei.

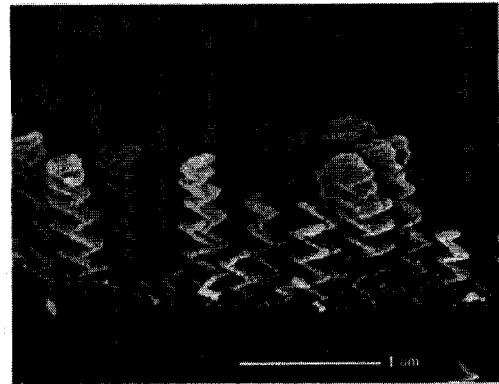
By varying  $\alpha$ , the range of porosity in the film is very controllable [64]. Also, as was implied in Fig. 1(a), by introducing a rotation of the substrate, which was illustrated by the  $\varphi$  rotation, one can tailor-make the overall structure of the posts by a careful selection of the substrate rotation  $d\varphi/dt$ . For example, by using a smoothly varying and continuous  $d\varphi/dt$  the posts grow vertically outward from the substrate with a rapid rotation (Fig. 3(a) [65, 66]), or one can fabricate helices by a slow, constant slow rotation in  $\varphi$  (Fig. 3(b) [31, 66]). By using a stepped rotation in  $\varphi$ , one can fabricate chevrons by intermittent, rapid rotation in  $\varphi$  by  $180^\circ$  (Fig. 3(c) [66]), or tetragonal square spirals by rapid, intermittent  $90^\circ$  rotations in  $\varphi$  (Fig. 3(d) [12]).

Some advanced deposition techniques for GLAD were also used throughout this work:

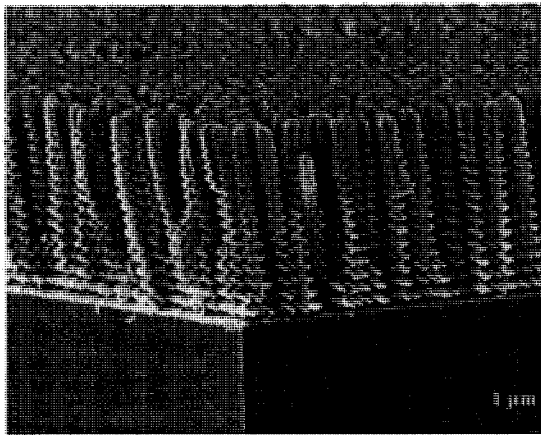
- The first of these is substrate seeding [6, 7, 67, 68] in which the substrate is patterned with a periodic array of photoresist using lithographic techniques so that during film deposition the columns preferentially grow on desired nucleation sites.
- The second is the called the PhiSweep technique [11] in which  $\phi$  is precessed about some fixed angle rather than simply being held fixed at said angle. This technique involves sweeping the substrate rotation angle back and forth about a central axis so that the average position of  $\phi$  remains constant, though the actual  $\phi$  precesses around that value. Since the substrate is repeatedly rotating back and forth across the central axis, the incident vapor only impinges upon the substrate along the central axis momentarily during each oscillation. However, the columnar film growth averages out and extends along the central axis. The PhiSweep method has successfully produced slanted post films, as well as polygonal spiral films [11, 22]. Investigating the effects of this technique on GLAD film structure has revealed more uniform structures, with significantly less inter-seed growth on periodically patterned substrates.
- The third is the capping layer technique [69] in which the deposition angle  $\alpha$  is slowly reduced so that the resultant film is composed columns with a solid layer of film material on top.



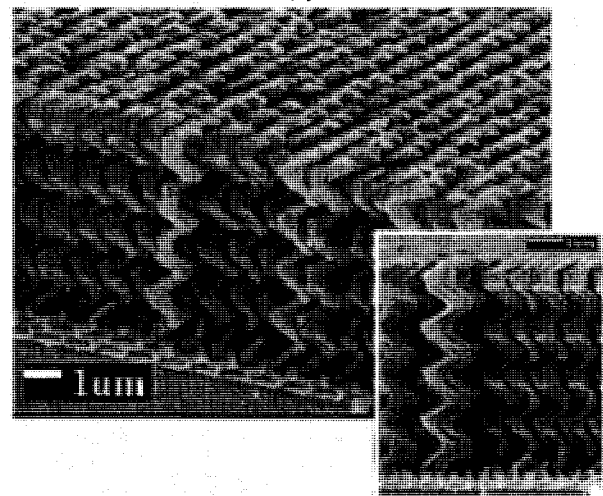
(a)



(c)



(b)



(d)

Figure 3 – (a) Vertical pillar microstructure by rapid rotation in  $\varphi$  [65], (b) Helical structures formed by a slow rotation in  $\varphi$  [66], (c) Zigzag microstructure by intermittent, rapid rotation in  $\varphi$  [66], and (d) Periodic tetragonal square spirals formed by rapid, intermittent  $90^\circ$  rotations, grown on a “seeded” substrate for controlled spacing of the posts [12].<sup>1</sup>

The ability to tailor the morphology of GLAD films leads to a wide range of interesting optical properties. Some examples include circular polarization filters [28, 29, 34, 70-73], graded index films for anti-reflection coatings [27], rugate

---

<sup>1</sup> Figures 3(b) and (c) used with permission from K. Robbie and M. J. Brett, “Sculptured thin films and glancing angle deposition: Growth mechanics and applications,” *J. Vac. Sci. Technol. A*, vol. 15, pp. 1460-1465, 1997. Copyright 1997, American Institute of Physics. Figure 3(d) is reprinted with permission from S. R. Kennedy, M. J. Brett, O. Toader, and S. John, “Fabrication of tetragonal square spiral photonic crystals,” *Nano Lett.*, vol. 2, pp. 59-62, 2002. Copyright 2002, American Chemical Society.

filters [74], or spectral hole filters [19, 35, 75], or producing silicon square spirals for photonic band structures [12, 22]. The purpose of this work was to use variable angle spectroscopic ellipsometry to characterize various structures produced by the GLAD technique to describe and model their optical properties.

## **1.2 – The Basics of Ellipsometry**

Variable angle spectroscopic ellipsometry (VASE) is useful in determining optical parameters for many different types of thin films [39, 76]. The key reason for this is in the very definition of VASE – the fact that the angle of incidence of a light beam is variable, and the fact that the light source is broadband, thus optimizing the sensitivity to unknown parameters [39] and negating the limitations of single wavelength ellipsometry. A common example of the limitations of single wave ellipsometry is the "period" problem in thickness measurement of thick films, caused by multiple reflections within the film [39]).

The basic principle behind all ellipsometry is Fresnel reflection or transmission of polarized light. An ellipsometric measurement is generally a measurement in terms of the ellipsometric parameters  $\Psi$  and  $\Delta$ , as given by the following ratio [37-39, 76]:

$$\tan(\Psi)\exp(i\Delta) = \rho \equiv \frac{r_p}{r_s} \quad (1.2.1)$$

where  $r_p$  and  $r_s$  are the complex Fresnel reflection coefficients for  $p$ - and  $s$ -polarized light with respect to the plane of light incidence, respectively. We can note at this point that the physical meaning of  $\tan(\Psi)$  is the ratio of the *magnitude* of the  $p$ - to  $s$ -reflection coefficient, or  $|r_p|/|r_s|$  while  $\Delta$  is the *phase*

*difference* between the *p*- and *s*-polarization state, or  $\Delta = \delta_p - \delta_s$ . This analysis yields highly accurate measurement since the *ratio* of two values is determined; thus, no reference sample is needed. The importance of this is that factors such as long term fluctuations in the light source are factored out of the equation.

VASE can measure many different material parameters, such as the film thickness (in principle, down to the sub-Å scale, since  $\Psi$  and  $\Delta$  can be measured for mid-range values to better than  $0.02^\circ$  and  $0.1^\circ$ , respectively), surface roughness [77], and optical constants  $n$  and  $k$  [39, 76]. More relevant to this study, one can also measure optical anisotropy with VASE by using the appropriate best-fit regression analysis on the ellipsometric data, based on the microstructure of the real film.

There are several possible VASE measurement schemes, such as the rotating analyzer ellipsometry (RAE) and rotating polarizer ellipsometry (RPE). Some of these different configurations are highlighted the block diagram in Fig. 4 [39].

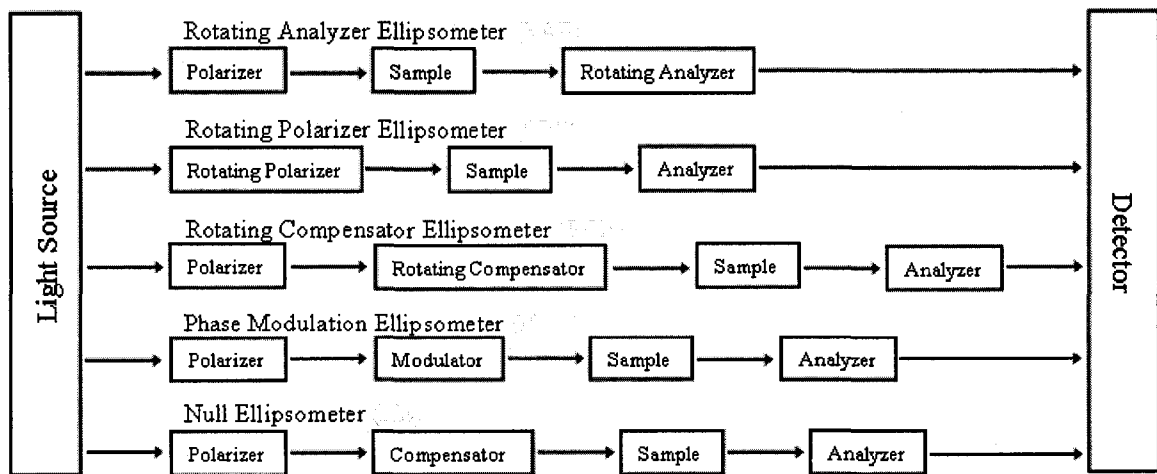


Figure 4 – Schematic for various ellipsometer configurations. Adapted from [39].



Each of these configurations has its own advantages and disadvantages [39], which are beyond the scope of this work, and there have been other configurations developed, which are each used for specific reasons, depending on the measurement sought, and the type of film used. For example, a more recent technique using dual rotating compensators has been developed to optimize certain measurements of anisotropic films [44, 78, 79].

Ellipsometry measures the two quantities  $\Psi$  and  $\Delta$ ; therefore, fitting algorithms must be used to acquire useful data from the raw data. The fitting algorithms used must be relevant to the film in question; therefore a film with a complex structure can make for a complicated analysis procedure, as will be seen in §2.2. Furthermore, due to the nature of GLAD films, the parameters  $\Psi$  and  $\Delta$  are not always sufficient to describe the film medium; we must rather measure the Mueller matrix, which provides a more complete polarization state description of the light that interacts with GLAD films.

### ***1.3 – The Mueller Matrix***

Often, a two-element Jones vector is used to describe the polarization state of light, while a 2 by 2 matrix called the Jones matrix describes the effect of an optical element on the polarization state of light. Thus, the Jones matrix multiplied by the Jones vector for an input polarization of light gives the Jones vector for the output polarization state [80]. The Jones formalism is that which is used in equation 1.2.1. It works well in situations where there is no depolarization of light occurring within the sample; for instance, in the case of a dense film. The limitation of the Jones formalism is that the light must be

completely polarized, that is, there exists no random component to the polarization state of the light.

Stokes vector formalism is a generalization of the degree of polarization in addition to the polarization state of light, *i.e.* systems involving non-completely polarized light can be described. It is important to note that a Jones vector can always be described by some Stokes vector equivalent; however the inverse is not true. In this chapter, we will examine the Stokes vector formalism [81], since ellipsometry, in essence, is the measurement of the Stokes vector of light that reflects off of or transmits through a sample.

As was stated earlier, the Jones formalism is comprised of a Jones vector describing the polarization state of light, and the Jones matrix which describes the effect that an optical element (such as a thin film) has on the Jones vector. Analogously, the Stokes vector formalism is a useful mathematical tool for describing the polarization state of a beam of light, while the Mueller matrix method expresses the change in degree and/or state of a beam of light by a given optical element [81, 82].

The most general mathematical form for the polarization state of a plane wave is elliptical; thus, the electric field vectors for light propagating in the  $z$ -direction can be written generally as:

$$E_x = E_{ox} \cos(\omega t - kz + \delta_x) \quad (1.3.1a)$$

$$E_y = E_{oy} \cos(\omega t - kz + \delta_y) \quad (1.3.1b)$$

where  $E_x$  and  $E_y$  are the x- and y-components of the electric field vector, respectively,  $E_{ox}$  and  $E_{oy}$  describe the magnitude of the oscillation, and  $\delta_x$  and  $\delta_y$  are phase factors for the x- and y- electric field oscillations, respectively.<sup>2</sup>

To describe the polarization state of light, one can define the following time-averaged quantities (assuming that  $E_{ox}$  and  $E_{oy}$  can be written as time-varying quantities), which are known as the Stokes parameters:

$$S_0 = \langle\langle E_{ox}^2 + E_{oy}^2 \rangle\rangle \quad (1.3.2a)$$

$$S_1 = \langle\langle E_{ox}^2 - E_{oy}^2 \rangle\rangle \quad (1.3.2b)$$

$$S_2 = 2\langle\langle E_{ox}E_{oy} \cos \delta \rangle\rangle \quad (1.3.2c)$$

$$S_3 = 2\langle\langle E_{ox}E_{oy} \sin \delta \rangle\rangle \quad (1.3.2d)$$

where  $\delta \equiv \delta_y - \delta_x$  and the double brackets denote time averaging over given time period (*i.e.*, one that is characteristic of the time constant of a detection process). These four Stokes parameters comprise the elements of the Stokes vector ( $S_0, S_1, S_2, S_3$ ). It can be shown that the Stokes parameters obey the following relation:

$$S_0^2 \geq S_1^2 + S_2^2 + S_3^2 \quad (1.3.3)$$

where the equality occurs only for completely polarized light. For randomly polarized light, there is no preference between  $E_{ox}$  and  $E_{oy}$ , therefore  $\langle E_{ox}^2 + E_{oy}^2 \rangle$  reduces to  $2\langle E_{ox}^2 \rangle$  while  $\langle E_{ox}^2 - E_{oy}^2 \rangle$  reduces to 0. The other quantities also reduce to 0 since  $\delta$  is a random function of time. Therefore, when the field is normalized such that  $S_0 = 1$ , the Stokes vector for unpolarized light can be written as (1,0,0,0). One can also derive the normalized Stokes vector for x-polarized

---

<sup>2</sup> As an example, for circularly polarized light:  $E_{ox} = E_{oy}$  and  $\delta \equiv \delta_y - \delta_x = \pm \pi/2$

light as (1,1,0,0),  $y$ -polarized light as (1,-1,0,0), left-circularly polarized (LCP) light (*i.e.*, when  $\delta = \pi/2$ ) as (1,0,0,1) and right-circularly polarized (RCP) light (*i.e.*, when  $\delta = -\pi/2$ ) as (1,0,0,-1). The Stokes parameters can also describe other properties of the polarization state of the light, such as the degree of polarization (1.3.4), the inclination angle of the ellipse,  $\phi$  (1.3.5), or the ellipticity,  $e$  (1.3.6).

$$\frac{(S_1^2 + S_2^2 + S_3^2)^{1/2}}{S_0} \quad (1.3.4)$$

$$\tan 2\phi = \frac{S_2}{S_1} \quad (1.3.5)$$

$$e = \tan\left(\frac{\arcsin(-S_3)}{2}\right) \quad (1.3.6)$$

The degree of polarization, given in (1.3.4), ranges from 0 to 1, where a value of 0 indicates that the light is completely depolarized, while a value of 1 indicates that the light is completely polarized and thus the Stokes parameters could be reduced to the Jones formalism, which yields the following vector to describe the polarization state of light:

$$\mathbf{J} = \begin{pmatrix} E_{ox} e^{i\delta_x} \\ E_{oy} e^{i\delta_y} \end{pmatrix} \quad (1.3.7)$$

Since, in general, any optical element (such as a linear polarizer or wave plate) can perturb the polarization state of an incident light beam, we may now define the Mueller matrix as a  $4 \times 4$  matrix that describes how an optical element affects the Stokes vector for a beam of light upon transmission or reflection [82]. The utility of this matrix is that it applies itself to any arbitrary Stokes vector and is independent of the Stokes parameters. Furthermore, if we have a system

whereby light passes through several elements, by using matrix multiplication, several cascaded optical elements can be reduced to one  $4 \times 4$  matrix<sup>3</sup>, and thus a Mueller matrix,  $M_{ij}$  for an optical system. The following table lists Mueller matrices for transmitted light for a few typical optical elements, assuming no depolarization effects occur within the optical element:

Optical Element	Mueller Matrix
Linear Horizontal ( $x$ -axis) Polarizer	$\frac{1}{2} \begin{pmatrix} 1 & 1 & 0 & 0 \\ 1 & 1 & 0 & 0 \\ 0 & 0 & 0 & 0 \\ 0 & 0 & 0 & 0 \end{pmatrix}$
Linear Vertical ( $y$ -axis) Polarizer	$\frac{1}{2} \begin{pmatrix} 1 & -1 & 0 & 0 \\ -1 & 1 & 0 & 0 \\ 0 & 0 & 0 & 0 \\ 0 & 0 & 0 & 0 \end{pmatrix}$
Quarter-Wave Plate (fast-axis along $y$ )	$\begin{pmatrix} 1 & 0 & 0 & 0 \\ 0 & 1 & 0 & 0 \\ 0 & 0 & 0 & -1 \\ 0 & 0 & 1 & 0 \end{pmatrix}$
Quarter-Wave Plate (fast-axis along $x$ )	$\begin{pmatrix} 1 & 0 & 0 & 0 \\ 0 & 1 & 0 & 0 \\ 0 & 0 & 0 & 1 \\ 0 & 0 & -1 & 0 \end{pmatrix}$

Table 1 – Mueller matrices for some typical optical elements.

The Mueller matrix formalism as it pertains to GLAD films has much utility. Since the Mueller matrix can be used to obtain information on the degree of polarization, one can compute the depolarization metric [83] for a given GLAD

---

<sup>3</sup> For a series of optical elements, where  $M_1$  is the first optical element with which the incident Stokes vector,  $S_i$ , interacts, and  $M_n$  is the final optical element with which the light interacts, before an output Stokes vector,  $S_o$  is obtained, the matrix multiplication must be applied as follows:  $S_o = M_n M_{n-1} \dots M_3 M_2 M_1 S_i$

film. Another example of its usefulness extends to obtaining useful parameters such as the difference in transmission or reflection of left-circularly polarized (LCP) versus right-circularly polarized light (RCP) for helical films. This difference is precisely the  $M_{14}$  component of the Mueller matrix [33]. An extensive study on the usage of the full Mueller matrix to characterize one class of GLAD films was performed by Collins *et al* at Penn State University [41, 84, 85]. In their works, they examined a helically structured  $\text{MgF}_2$  GLAD film produced at the University of Alberta by Robbie *et al* [29]. Though their study is of some relevance to this work, their study involved the use of a Mueller matrix ellipsometer to measure the characteristics of a helical GLAD film, and was more principally focused on the construction of the ellipsometer itself, and continued to rely on estimates of film index of refraction. This work, however was principally focused on using ellipsometry to acquire fundamental optical constants for GLAD films, as well as provide a recipe for analysis of GLAD films in general.

#### **1.4 – Effective Medium Approximation**

Since GLAD films are a mixture of film material and air (commonly expressed as void), we must examine the manner in which the indices of refraction in GLAD films are described. Thus, this section provides an overview of effective medium approximations (EMA), including a discussion of the foundations of the theory leading to the Bruggeman effective medium approximation (BEMA). The extension of the BEMA that is used to deal with anisotropically shaped inclusions within a mixture will then be discussed,

followed by a discussion on the limitations of effective medium approximations. These approximations typically assume that the sizes of the inclusions are much smaller than the wavelengths of the light. Though for our case, this is true for most wavelengths and generally these approximations work well due to minimal scattering in films examined in this study by limiting the film thickness, we will also examine the wavelength correction effects in §5.4.

We begin our examination of EMAs by starting with the Clausius-Mossotti relation, which can be found in most upper-level undergraduate electromagnetics textbooks (see for example [86]), and is often expressed as:

$$\frac{\varepsilon - 1}{\varepsilon + 2} = \frac{4\pi}{3} \sum_j N_j \alpha_j \quad (1.4.1)$$

where  $\varepsilon$  is the dielectric constant for a medium with  $N_j$  molecules or inclusions of the same material per unit volume with a microscopic (or molecular) polarizability  $\alpha_j$ . This expression contains the link between the microscopic properties of a system and the macroscopic observable  $\varepsilon$  (or the index of refraction,  $n$ , and the extinction coefficient,  $k$ ). The development on Clausius-Mossotti which was credited to Maxwell-Garnett was to first assume that there is a link between the microscopic polarizability of an inclusion and its macroscopic counterpart, in other words, we can say that the dielectric constant of the inclusion is  $\varepsilon_1$ , which yields:

$$\alpha = \left( \frac{\varepsilon_1 - 1}{\varepsilon_1 + 2} \right) a^3 \quad (1.4.2)$$

for a spherical particle of radius  $a$ . In this case of oriented ellipsoidal particles of semi-axes  $a$ ,  $b$ , and  $c$ , we can write this as:

$$\alpha_{ii} = \frac{1}{3} \left( \frac{\varepsilon_i - 1}{1 + (\varepsilon_i - 1)q_i} \right) abc \quad (1.4.3)$$

where the depolarization factors  $q_i$  are given using elliptical integrals [51] and describe the shapes of the inclusions. Often the shapes of the inclusions are assumed to be spherical, leading to  $a = b = c$  and the solution to the elliptical integrals for spherical inclusions is  $q_i = 1/3$ , thus reducing (1.4.3) to the expression given in (1.4.2). If we now substitute (1.4.2) into (1.4.1), we obtain:

$$\left( \frac{\varepsilon - 1}{\varepsilon + 2} \right) = \frac{\eta_i}{3} \left( \frac{\varepsilon_i - 1}{\varepsilon_i + 2} \right) \quad (1.4.4)$$

where  $\eta_i$  is the volume fraction of the inclusions, and similarly, for ellipsoidal inclusions, we obtain:

$$\left( \frac{\varepsilon - 1}{\varepsilon + 2} \right) = \eta_i \left( \frac{\varepsilon_i - 1}{1 + (\varepsilon_i - 1)q_i} \right) \quad (1.4.5)$$

As before, for spherically shaped inclusions,  $q_i = 1/3$ , in which case (1.4.5) becomes (1.4.4). Also, of relevance to GLAD films (which are columns), the  $q_i$  for rods approaches 0. At this point, we would like to factor out the vacuum permittivity  $\varepsilon_0$ , which is the host medium, from (1.4.4). This yields the well known form of Maxwell-Garnett:

$$\left( \frac{\varepsilon - \varepsilon_0}{\varepsilon + 2\varepsilon_0} \right) = \eta_i \left( \frac{\varepsilon_i - \varepsilon_0}{\varepsilon_i + 2\varepsilon_0} \right) \quad (1.4.6)$$

As can be shown, an immediate problem arises with the use of Maxwell-Garnett in that if we choose the vacuum or void as the host medium, the formula follows (1.4.6), however, if we choose the inclusions as the host medium, we obtain (1.4.7):



$$\left( \frac{\varepsilon - \varepsilon_1}{\varepsilon + 2\varepsilon_1} \right) = \eta_0 \left( \frac{\varepsilon_0 - \varepsilon_1}{\varepsilon_0 + 2\varepsilon_1} \right) \quad (1.4.7)$$

which we can immediately see yields a different result for  $\varepsilon$ . In other words, the choice of which medium is the host affects the results, which is not acceptable. Furthermore, Maxwell-Garnett suffers problems when it comes to generalizing to multiple types of inclusions:

$$\left( \frac{\varepsilon - \varepsilon_0}{\varepsilon + 2\varepsilon_0} \right) = \sum_i \eta_i \left( \frac{\varepsilon_i - \varepsilon_0}{\varepsilon_i + 2\varepsilon_0} \right) \quad (1.4.8)$$

It can immediately be seen that the result here depends on the void medium (on the left hand side of the equation), even when the host has been replaced (i.e. when  $\sum \eta_i = 1$ ). Furthermore, (1.4.5) yields the incorrect result when  $\eta_1$  approaches 1, which is not acceptable.

We will now examine the improvements that Bruggeman made to the theory, which justifies the choice of Bruggeman EMA for the purpose of this study. Bruggeman began his approximation by treating the constituents within a mixture in a symmetric fashion. Thus, we consider a two-material system with fractions  $\eta_1$  and  $\eta_2$  with dielectric constants  $\varepsilon_1$  and  $\varepsilon_2$ , respectively, which comprises a homogeneous system of dielectric constant  $\varepsilon$ . Without loss of generality, we now assume that  $\varepsilon_1$  is spherical particles of radius,  $a$  within the host,  $\varepsilon$ . From electrostatics, we would evaluate the field outside and inside of the spherical particle to be:

$$\mathbf{E}_{outside} = \left( E_0 + 2\frac{C_1}{r^3} \right) \cos\theta \hat{r} + \left( E_0 + \frac{C_1}{r^3} \right) \sin\theta \hat{\theta} \quad (1.4.9)$$

$$\mathbf{E}_{inside} = -A_1 \cos \theta \hat{r} + A_1 \sin \theta \hat{\theta} \quad (1.4.10)$$

where  $C_1$  and  $A_1$  are given by:

$$C_1 = \left( \frac{\epsilon_1 - \epsilon}{\epsilon_1 + 2\epsilon} \right) a^3 E_o \quad (1.4.11)$$

$$A_1 = - \left( \frac{3\epsilon}{\epsilon_1 + 2\epsilon} \right) E_o \quad (1.4.12)$$

Now, we can calculate the electric flux deviations due to the polarization by the inclusions for a disc of surface area  $\pi a^2$  (or  $\theta = \pi/2$ ),  $\Delta\Phi_1$ , given by the following [51]:

$$\Delta\Phi_1 = 2\pi \left( \int_0^a dr r D - \int_0^a dr r \epsilon E_o \right) = 2\pi a^2 \epsilon E_o \left( \frac{\epsilon_1 - \epsilon}{\epsilon_1 + 2\epsilon} \right) \quad (1.4.13)$$

with  $D$  being the displacement current for the field near the sphere. If we then assume that the average flux deviations are zero, then we can write:

$$\eta_1 \Delta\Phi_1 + \eta_2 \Delta\Phi_2 = 0 \quad (1.4.14)$$

with  $\Delta\Phi_2$  is obtain equivalently using (1.4.13). In other words, the flux deviations are due to single particle polarizations in the effective medium,  $\epsilon$ . Using this hypothesis in (1.4.14), we arrive at the well know form of the BEMA:

$$\eta_1 \left( \frac{\epsilon_1 - \epsilon}{\epsilon_1 + 2\epsilon} \right) + \eta_2 \left( \frac{\epsilon_2 - \epsilon}{\epsilon_2 + 2\epsilon} \right) = 0 \quad (1.4.15)$$

Immediately recognizable is that this form can easily be generalized to any arbitrary number of components forming an effective medium:

$$\sum_i \eta_i \left( \frac{\epsilon_i - \epsilon}{\epsilon_i + 2\epsilon} \right) = 0 \quad (1.4.16)$$

The important thing to note about the BEMA is that, unlike MG, the choice of host is self-consistent [52], meaning that the effective medium is the host, rather than requiring one of the constituent media to be the host, which leads to difficulties already seen. The above section has discussed the BEMA for the simple case of spherical inclusions. Generalizing to the case of ellipsoidal inclusions, we obtain [51, 52]:

$$\eta_1 \left( \frac{\varepsilon_1 - \varepsilon}{\varepsilon_1 + (q_i^{-1} - 1)\varepsilon} \right) + \eta_2 \left( \frac{\varepsilon_2 - \varepsilon}{\varepsilon_2 + (q_i^{-1} - 1)\varepsilon} \right) = 0 \quad (1.4.17)$$

This description relates to GLAD columns in that we now have a means to describe the percentage concentration of a given film,  $\eta_{film}$ , using the optical constants of the film material,  $\varepsilon_{material}$ , using the appropriate factor  $q_i$  which describes the inclusion shapes along our principal axes within a film. It should be stressed at this time that the  $q_i$  values represent the index along a given principal index of refraction; for instance, with a biaxial medium, we would evaluate (1.4.17) for each principal index, where the  $\eta$  values are fixed for each axis, and the values for  $q_x$ ,  $q_y$ , and  $q_z$  give the index of refraction along each principal axis.

Given now a general description of GLAD films as a mixture of film material and void whose effects on light polarization can be expressed by the Mueller matrix, we must now examine the theoretical basis by which a film of effective medium,  $\varepsilon$ , produces a characteristic Mueller matrix,  $M$ . This will be examined in the following section.

## 1.5 – Description of an Anisotropic Stratified Film System

This section will discuss the theoretical formalism used to generate the theoretical description that is used when modeling films to obtain the spectroscopic ellipsometry parameters  $\Psi(\lambda)$ ,  $\Delta(\lambda)$ , and  $M_{ij}(\lambda)$ . The theoretical formalism used follows the well-known and commonly-used Berreman's method [57-61] for calculating reflection and transmission coefficients in stratified media. In general, our film system will be composed of a substrate with anisotropic layers or slabs. This problem has been dealt with in great detail by Schubert [61] in order to be applied to the specific problem of generating ellipsometric parameters for film systems, and this section will cover the calculation and will extend the calculation for the point of this work to include the calculation of the Mueller matrix.

We first consider a layered system with plane parallel interfaces, as in Fig.

5.

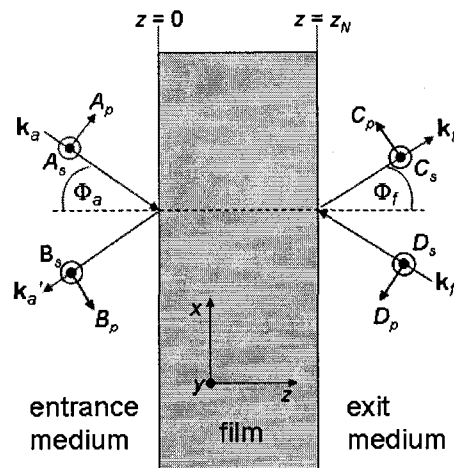


Figure 5 – Incident, reflected and transmitted  $p$ - and  $s$ -modes of a plane wave with wavevectors  $\mathbf{k}_a$ ,  $\mathbf{k}_a'$ ,  $\mathbf{k}_f$ , and  $\mathbf{k}_f'$ , respectively. Adapted from [61].

where we have an incident light wave vector  $\mathbf{k}_a$  coming from our light source traveling in ambient medium (air  $n_a = 1$ ,  $k_a = 0$ ), at an angle of incidence  $\Phi_a$ , and  $\mathbf{k}_a'$  is the reflected wave vector. As shown in Fig. 5,  $A_p$ ,  $A_s$ ,  $B_p$ , and  $B_s$  are the complex wave amplitudes of the  $p$ - and  $s$ -modes of the incident and reflected waves, respectively. If we also assume in this analysis that the substrate (*i.e.*, exit medium) is infinitely extending (or practically speaking the substrate has a roughened backside), thus we can neglect the back-traveling wave amplitudes  $D_p$  and  $D_s$ . Thus, we can define a general transfer matrix for the wave amplitudes for a given layered structure as:

$$\begin{pmatrix} A_s \\ B_s \\ A_p \\ B_p \end{pmatrix} = \begin{pmatrix} T_{11} & T_{12} & T_{13} & T_{14} \\ T_{21} & T_{22} & T_{23} & T_{24} \\ T_{31} & T_{32} & T_{33} & T_{34} \\ T_{41} & T_{42} & T_{43} & T_{44} \end{pmatrix} \begin{pmatrix} C_s \\ 0 \\ C_p \\ 0 \end{pmatrix} \quad (1.5.1)$$

where the  $T_{ij}$  allow us to obtain parameters of interest such as the Jones transmission and reflection coefficients as follows:

$$R_{ss} = \frac{T_{21}T_{33} - T_{23}T_{31}}{T_{33}T_{11} - T_{13}T_{31}} \quad (1.5.2a)$$

$$R_{pp} = \frac{T_{41}T_{13} - T_{11}T_{43}}{T_{13}T_{31} - T_{33}T_{11}} \quad (1.5.2b)$$

$$R_{ps} = \frac{T_{21}T_{13} - T_{23}T_{11}}{T_{13}T_{31} - T_{33}T_{11}} \quad (1.5.2c)$$

$$R_{sp} = \frac{T_{41}T_{33} - T_{31}T_{43}}{T_{11}T_{33} - T_{13}T_{31}} \quad (1.5.2d)$$

By using this analysis, we can describe the propagation of light in a given layered system by solving for the  $T_{ij}$  elements and now must examine the method for

doing so. We now define  $d_i$  as the thickness of the  $i^{\text{th}}$  layer in the film system, with a partial transfer matrix  $\mathbf{T}_{ip}$  which connects its wave amplitude components to the  $(i-1)^{\text{th}}$  and the  $(i+1)^{\text{th}}$  layers in our film, with the ordered product of the partial transfer matrices for all  $N$  layers yielding the  $4 \times 4$  matrix as seen in (1.5.1). We also at this point define the incident and exit matrices as  $\mathbf{L}_a$ ,  $\mathbf{L}_f$  as given by the following [61]:

$$\mathbf{L}_a^{-1} = \frac{1}{2} \begin{pmatrix} 0 & 1 & -1/n_a \cos \Phi_a & 0 \\ 0 & 1 & 1/n_a \cos \Phi_a & 0 \\ 1/\cos \Phi_a & 0 & 0 & 1/n_a \\ -1/\cos \Phi_a & 0 & 0 & 1/n_a \end{pmatrix} \quad (1.5.3)$$

$$\mathbf{L}_f = \begin{pmatrix} 0 & 0 & \cos \Phi_f & 0 \\ 1 & 0 & 0 & 0 \\ -n_f \cos \Phi_f & 0 & 0 & 0 \\ 0 & 0 & n_f & 0 \end{pmatrix} \quad (1.5.4)$$

where  $n_f$  and  $n_a$  are the complex indices of refraction of the substrate material and ambient material, respectively, and the angle  $\Phi_f$  can be obtained by using Snell's Law:

$$\cos \Phi_f = \sqrt{1 - \left(\frac{n_a}{n_f}\right)^2 \sin^2 \Phi_a} \quad (1.5.5)$$

Now, with the general description for all layers in our film system, we can obtain our transfer matrix,  $\mathbf{T}$  using the following expression [61]:

$$\mathbf{T} = \mathbf{L}_a^{-1} \prod_{i=1}^N \mathbf{T}_{ip}(-d_i) \mathbf{L}_f \quad (1.5.6)$$

where the thickness  $d_i$  of the  $i^{\text{th}}$  layer connects the wave components at the interface  $z = z_i$  with the next interface at  $z = z_i + d_i$ . If we now consider the case of a biaxial film with the principle axes  $\varepsilon_x$ ,  $\varepsilon_y$ , and  $\varepsilon_z$  oriented in a general direction, we can write its general dielectric tensor as follows:

$$\varepsilon = \mathbf{A} \begin{pmatrix} \varepsilon_x & 0 & 0 \\ 0 & \varepsilon_y & 0 \\ 0 & 0 & \varepsilon_z \end{pmatrix} \mathbf{A}^{-1} \quad (1.5.7)$$

where  $\mathbf{A}$  is an orthogonal rotation matrix which describes the Euler angle rotations about the lab frame of reference<sup>4</sup>, and is given by (see for example [87]):

$$\mathbf{A} = \begin{pmatrix} \cos \phi & \sin \phi & 0 \\ -\sin \phi & \cos \phi & 0 \\ 0 & 0 & 1 \end{pmatrix} \begin{pmatrix} 1 & 0 & 0 \\ 0 & \cos \theta & \sin \theta \\ 0 & -\sin \theta & \cos \theta \end{pmatrix} \begin{pmatrix} \cos \varphi & \sin \varphi & 0 \\ -\sin \varphi & \cos \varphi & 0 \\ 0 & 0 & 1 \end{pmatrix} \quad (1.5.8)$$

From first-order Maxwell equations, Berreman [58] derived a set of four differential equations for the in-plane components of the sinusoidally varying electric and magnetic fields in Gaussian units and Cartesian coordinates as [61]:

$$\partial_z \Psi(z) = ik_0 \Delta(z) \Psi(z) \quad (1.5.9)$$

$$\Psi(z) = (E_x, E_y, H_x, H_y)^T(z) \quad (1.5.10)$$

where  $k_0 = \omega/c_0$  and  $\omega$  is the angular frequency of the wave and  $c_0$  is the speed of light in vacuum, and the matrix  $\Delta$  depends on the dielectric tensor and the  $x$ -component of wavevector  $\mathbf{k}_a$ , which is denoted as  $k_x (= n_a \sin \Phi_a)$ . The matrix  $\Delta$  is thus given by:

---

<sup>4</sup> We note here that GLAD produced columns only have a rotation in the Euler angles  $\theta$  and  $\phi$ .

$$\Delta = \begin{pmatrix} -k_x \frac{\epsilon_{31}}{\epsilon_{33}} & -k_x \frac{\epsilon_{32}}{\epsilon_{33}} & 0 & 1 - \frac{k_x^2}{\epsilon_{33}} \\ 0 & 0 & -1 & 0 \\ \epsilon_{23} \frac{\epsilon_{31}}{\epsilon_{33}} - \epsilon_{21} & k_x^2 - \epsilon_{22} + \epsilon_{23} \frac{\epsilon_{32}}{\epsilon_{33}} & 0 & k_x \frac{\epsilon_{23}}{\epsilon_{33}} \\ \epsilon_{11} - \epsilon_{13} \frac{\epsilon_{31}}{\epsilon_{33}} & \epsilon_{12} - \epsilon_{13} \frac{\epsilon_{32}}{\epsilon_{33}} & 0 & -k_x \frac{\epsilon_{13}}{\epsilon_{33}} \end{pmatrix} \quad (1.5.11)$$

and finally, the partial transfer matrix for the film is given by:

$$\mathbf{T}_{ip} = \exp\left(j \frac{\omega}{c_0} \Delta d_i\right) \quad (1.5.12)$$

and the partial transfer matrix can be evaluated by using the Cayley-Hamilton theorem stating that this matrix function can be expressed by a series expansion up to the rank of the matrix minus one (so in this case 3), which is given by the following identities:

$$\mathbf{T}_p = \exp\left(j \frac{\omega}{c_0} \Delta d_i\right) = \beta_0 \mathbf{I} + \beta_1 \Delta + \beta_2 \Delta^2 + \beta_3 \Delta^3 \quad (1.5.13)$$

where the scalars  $\beta_0$  through  $\beta_3$  obey the following set of equations:

$$\exp\left(j \frac{\omega}{c_0} q_k d_i\right) = \sum_{j=0}^3 \beta_j q_k^j \quad (1.5.14)$$

for  $k = 1..4$ , and the  $q_j$  are the eigenvalues of the matrix  $\Delta$ .

Now that the partial matrices for our film layer system are solved using (1.5.7) to (1.5.14), the complete transfer matrix for a given air-film-substrate system can now be solved by substituting the layer matrices into (1.5.6), and finally solve for our Jones reflection matrix coefficients using the expressions given in (1.5.2). It is important to note at this point that one could also have evaluated similar expressions to those shown in (1.5.2) for the Jones



transmission matrix (herein denoted by  $\mathbf{J}$ ) coefficients by applying the proper formulae.

Now that we have the Jones reflection coefficients, we can finally solve for the Mueller reflection matrix using the following expression [88]:

$$\mathbf{M} = \mathbf{B}(\mathbf{J} \otimes \mathbf{J}^*)\mathbf{B}^{-1} \quad (1.5.15)$$

where  $\mathbf{J}^*$  is the conjugate transpose of the Jones matrix, the symbol  $\otimes$  represents the Direct (or Kronecker) matrix product operation, and the matrix  $\mathbf{B}$  is given by:

$$B = \begin{pmatrix} 1 & 0 & 0 & 1 \\ 1 & 0 & 0 & -1 \\ 0 & 1 & 1 & 0 \\ 0 & i & -i & 0 \end{pmatrix} \quad (1.5.16)$$

For the Maple code of a calculation performed using this technique as it applies to studies contained in this work, please see Appendix 1. Other applications of this technique have been used in other studies for the evaluation of the transmission modes for GLAD films such as rugate filters and spectral hole filters [19], and helical thin films [89].

Now that we have arrived at a theory to describe an effective medium,  $\varepsilon$ , with film layers that give us a Mueller matrix, we must now examine the theory behind optical properties of film materials, as will be seen in the following section.

## **1.6 – Optical Constant Dispersion**

The optical properties of the film materials were described using various optical dispersion functions, depending on the material itself. This section will cover the basics and physical principles behind optical dispersion.

One of the most basic, and probably the most well-known and used dispersion equation was proposed by Cauchy in 1830 [38], known as the Cauchy dispersion equation. Together with the Urbach absorption model [38], the two equations are used to obtain the index of refraction and extinction coefficient,  $n$  and  $k$ , as functions of wavelength,  $\lambda$ :

$$n(\lambda) = A + \frac{B}{\lambda^2} + \frac{C}{\lambda^4} \quad (1.6.1a)$$

$$k(\lambda) = D \exp \left[ F \left( \frac{1240}{\lambda} - \frac{1240}{\gamma} \right) \right] \quad (1.6.1b)$$

where  $A$ ,  $B$ ,  $C$ ,  $D$ , and  $F$ , are constants which depend on the material, and  $\gamma$  is a parameter that is set to a convenient value, and is a “fudge factor” generally set to the lowest wavelength used experimentally since the Urbach expression (1.6.1b) is in reality a two-parameter expression. Two things to note about (1.6.1b) are that when  $\lambda = \gamma$ ,  $k = D$ , and the value of 1240 is for the sake of converting  $F$  from units of [eV] to [nm]. This set of equations is commonly used to describe the optical dispersion for transparent media, or media with very weak optical absorption in the wavelengths of interest, with this work being no exception.

To obtain a better understanding of the origin of the Cauchy formula and justification for its use here, it is important to examine more general optical dispersion functions. Another commonly used and well understood dispersion function is the Lorentz oscillator, and can be found in most electromagnetics textbooks. The physical principle behind the Lorentz oscillator is that an oscillating electric field (*i.e.*, electromagnetic radiation) drives the motion of an electron bound to a nucleus. The motion of an electron with time-dependent

position,  $\mathbf{r}$ , can thus be described using a damped simple harmonic oscillator with an external driving force, given by the following:

$$m_e \frac{d^2 \mathbf{r}}{dt^2} + m_e \Gamma \frac{d\mathbf{r}}{dt} + m_e \omega_0^2 \mathbf{r} = -e\mathbf{E} \quad (1.6.2)$$

where  $\mathbf{E}$  is the applied electric field,  $\Gamma$  describes the damping of the system,  $m_e$  is the mass of an electron with charge,  $e$ , and  $\omega_0$  is the resonant frequency of oscillation. If we assume that  $\mathbf{E}$  and  $\mathbf{r}$  vary in time as  $e^{-i\omega t}$ , then a solution to (1.6.2) is:

$$\mathbf{r} = \frac{1}{m_e} \frac{e\mathbf{E}}{(\omega_0^2 - \omega^2) - i\Gamma\omega} \quad (1.6.3)$$

if we now solve for the polarizability of the atom,  $\alpha$ , we obtain:

$$\alpha(\omega) = \frac{e^2}{m_e} \frac{1}{(\omega_0^2 - \omega^2) - i\Gamma\omega} \quad (1.6.4)$$

and since the dielectric constant relates to the polarizability as  $\varepsilon = 1 + 4\pi N\alpha$ , we can obtain the dielectric constant to be:

$$\varepsilon = 1 + \frac{4\pi N e^2}{m_e} \frac{1}{(\omega_0^2 - \omega^2) - i\Gamma\omega} \quad (1.6.5)$$

and finally, if we separate the real and imaginary parts of the dielectric constant such that  $\varepsilon = \varepsilon_1 + i\varepsilon_2$ , we obtain:

$$\varepsilon_1 = 1 + \frac{4\pi N e^2}{m_e} \frac{(\omega_0^2 - \omega^2)}{(\omega_0^2 - \omega^2)^2 + \Gamma^2 \omega^2} \quad (1.6.6a)$$

$$\varepsilon_2 = \frac{4\pi N e^2}{m_e} \frac{\Gamma\omega}{(\omega_0^2 - \omega^2)^2 + \Gamma^2 \omega^2} \quad (1.6.6b)$$

If we now plot these for illustrative purposes as a function of  $\omega$ , we would obtain an example that roughly illustrates UV absorption using Lorentz dispersion with a line centered at 200 nm (or  $\omega_0 = 9.42 \times 10^{15}$  rad/s), and an oscillator width  $\Gamma = 1 \times 10^{15}$  rad/s (say for instance,  $\text{TiO}_2$ ):

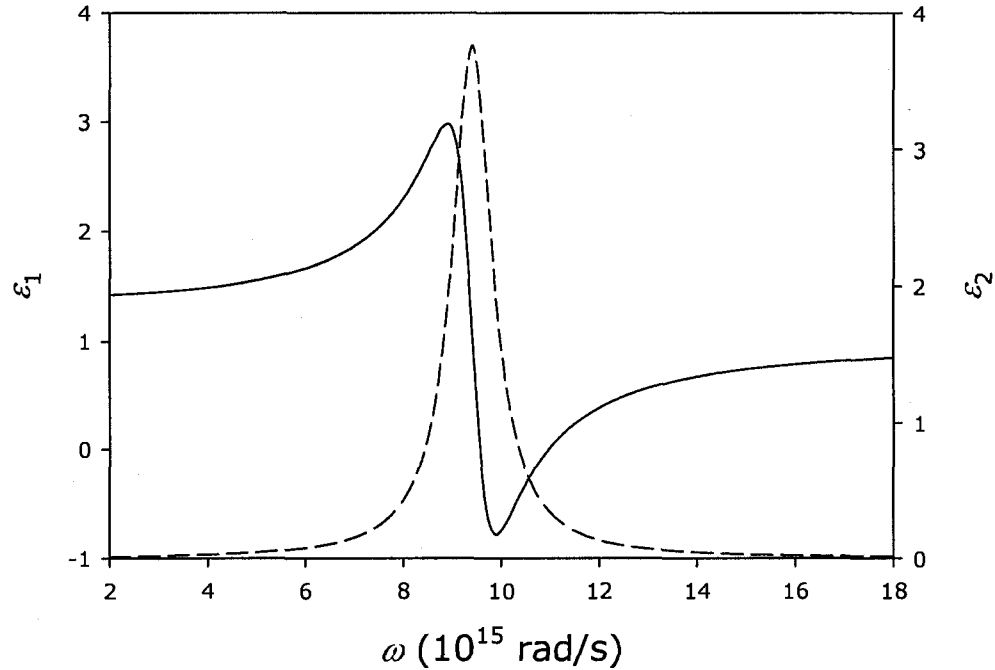


Figure 6 – Example of Lorentzian dispersion in the dielectric constants  $\epsilon_1$  (solid) and  $\epsilon_2$  (dashed) as given by (1.6.6)

We can see that except for a region near  $\omega_0$ ,  $\epsilon_1$  increases with  $\omega$ ; this is known as normal dispersion. Anomalous dispersion is the region in which  $\epsilon_1$  decreases with increasing  $\omega$ . Note also regarding (1.6.6), that when the wavelength range of interest is far removed from  $\omega_0$ , the optical dispersion is often approximated by expressions such as (1.6.1) by using the following relationship relating the dielectric function to the index of refraction:

$$\epsilon = (n + ik)^2 \quad (1.6.7)$$

Many of the materials examined in this study (such as  $\text{MgF}_2$ ,  $\text{SiO}_2$ ,  $\text{Al}_2\text{O}_3$ ) were modeled quite effectively using the simple Cauchy and Urbach dispersion models seen in (1.6.1). However, describing dispersion in other materials required the use of oscillators such as the Gaussian (to describe, for example,  $\text{TiO}_2$ ), the Drude oscillator in the case of metals, and the Tauc-Lorentz oscillator [90, 91] (to describe, for example,  $\text{Alq}_3$ ). Furthermore, some materials require the use of more than one oscillator function due to complex electronic structures in compounds (for instance), where the dielectric constant for multiple oscillators can be written using the superposition principle. The methods used to determine which oscillators are appropriate to a given material are by consulting the literature regarding the optical properties of the material in question, and by trial and error. We can also often get a good idea of the nature of the dispersion by examining the transmission or reflection spectrum of the film in question.

In general, once we obtain optical constants for a film, we need to ensure that they are consistent with the Kramers-Kronig relations (see for example [92]), as given by the following Principal Value integrals:

$$\varepsilon_1(\omega) = 1 + \frac{2}{\pi} P \int_0^{\infty} \frac{\omega' \varepsilon_2(\omega')}{\omega'^2 - \omega^2} d\omega' \quad (1.6.8a)$$

$$\varepsilon_2(\omega) = -\frac{2\omega}{\pi} P \int_0^{\infty} \frac{\varepsilon_1(\omega')}{\omega'^2 - \omega^2} d\omega' \quad (1.6.8b)$$

These expressions relate the real and imaginary components of the dielectric constants with each other. The key point about these relations is that they arise from the causal and linear nature of optical constants and must hold true for a set of optical constants to be considered physically realistic. An example of Kramers-

Kronig consistency applied to the aforementioned Lorentz oscillator can be found in Appendix 2. We may also apply Kramers-Kronig to our Cauchy and Urbach relations and find that they are in fact *not* Kramers-Kronig consistent. This is forgiven, however, by the fact that these relations are long wavelength approximations to oscillators which *are* Kramers-Kronig consistent. The point here is that we must not forget Kramers-Kronig and must be careful when applying formulae which do not hold. Another important point to mention here is that with some oscillators (the Gaussian and the Tauc-Lorentz oscillators, for example) have real components of their dielectric constants that are expressly determined by applying Kramers-Kronig to their imaginary parts. Typically for a given material of interest we do not have a means to measure the material's properties over the entire electromagnetic spectrum, and need to assume that there is an offset from 1 for the real part of the dielectric constant,  $\epsilon_{1,Offset}$ . This offset can be viewed as the real part of the dielectric constant at a wavelength corresponding to  $\lambda_{light} = \infty$ . Thus, in general, we write the dielectric constants for any given system as the sum of all oscillators and offsets as:

$$\epsilon = \epsilon_{1,Offset} + \epsilon_{Oscillators} \quad (1.6.9)$$

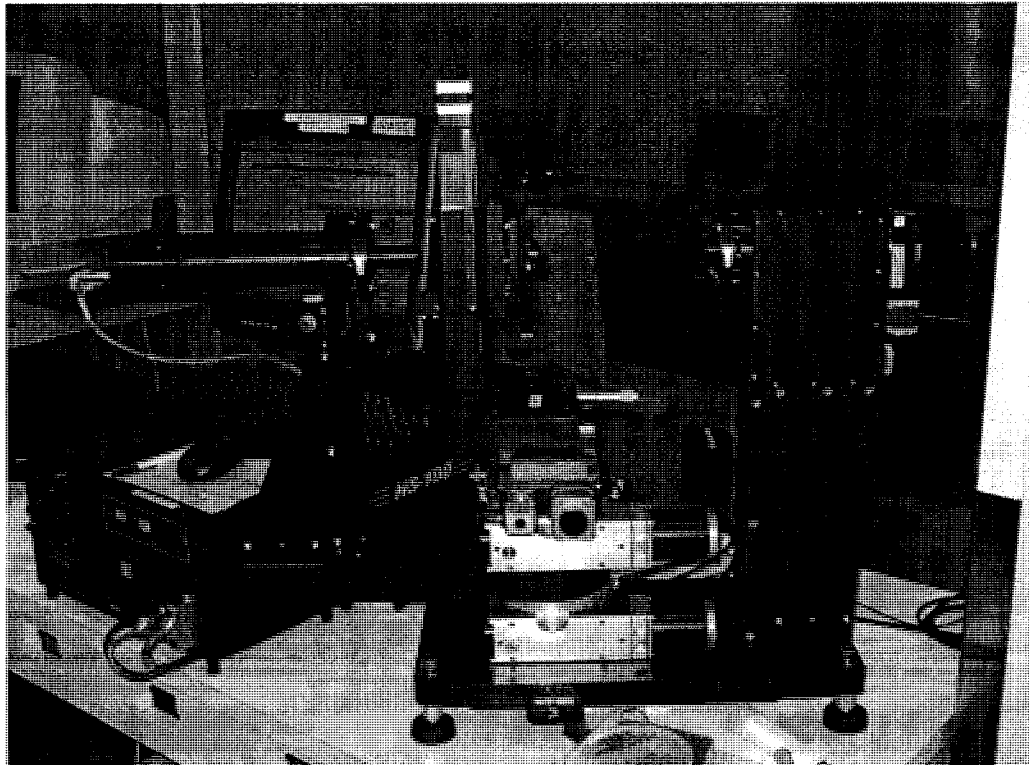
In summary, a complete description of films produced by GLAD can be obtained by first measuring its characteristic Mueller matrix, which is then compared with a theoretical Mueller matrix obtained using Berreman's matrix method, where the film system is composed of an EMA composed of a mixture of void and material, whose optical constants are governed by oscillator theory. This is useful in examining GLAD films since we need not assume material

constants using standard tables, and thus can evaluate parameters such as GLAD film density compared to bulk film density.

## 2 – Experimental Details

### 2.1 – *The Variable Angle Spectroscopic Ellipsometer Hardware*

Ellipsometry and Mueller matrix measurements within this work were performed using a commercially available spectroscopic ellipsometer (V-VASE model, J. A. Woollam Co. Inc.). The V-VASE instrument can be broken down into three distinct components: the optical system stage (Fig. 7a), and the computer controller/controller hardware (Fig. 7b), and the light source/monochromator (Fig. 7b).



(a)





(b)

Figure 7 – Images of the variable angle spectroscopic ellipsometer (a) and the controller computer and light source/monochromator (b).

The computer controller contains the hardware cards, embodied within the VB-250 module, that are used to control the motors within the HS-190 high speed monochromator, and motion and position of the optics and motor arms in the optical system stage. This is interfaced with a Microsoft Windows-based computer, running the WVASE32 software which was included with the ellipsometer. The operation of the ellipsometer system is done by using the “Hardware” window located within the WVASE32 software, where the user can set up and define the types of scans desired, as well as the averaging schemes for light detection, monochromator settings, and which optics are to be enabled or disabled during the measurement scheme. The user also inputs the angles of incidence desired for the measurement, and the light wavelength range of

interest. The user may also control the beam spot location on the sample being examined using the substrate stepper motor.

The light source used in the HS-190 module is a 75 W Xe arc lamp (model L2174-01, Hamamatsu Photonics). The light output from the xenon lamp is focused using concave mirrors. This light is then passed to a series of computer-controlled grating mirrors and slits to select individual wavelengths from the light source (Fig. 7b). The precision of this monochromator is 0.1 nm and the bandwidth of the light output is no more than 3.9 nm (based on a grating dispersion of 2.3 nm/mm and a maximum slit width used in the experiments of 1.7 mm). The range of the light output for this particular model of light source is 300 nm to 1700 nm. The speed at which the light output switches from one wavelength to the next during a scan is on the order of a few seconds to a few minutes, depending on the complexity of the data acquisition mode.

The light output from the HS-190 module is then coupled to an optical fibre. The V-VASE was supplied with two types of fibres that are available for use, depending on the application. One type of these fibres has a nominal wavelength range, when used with this instrument, of 400 nm to 1700 nm (the so-called "IR Fibre"); the other type of fibre has a nominal wavelength range of 300 nm to 1350 nm, and 1450 nm to 1700 nm (the so-called "UV Fibre"). If the user wishes to obtain the full available spectrum (300 nm to 1700 nm), two measurements are necessary: one with the UV Fibre in place, and another with the IR Fibre in place.

The light coming from the fibre then reaches the optical system stage of the V-VASE. The light first passes through a computer controlled linear

polarizer, and then optionally through a computer controlled MgF<sub>2</sub> Berek wave plate which is used to introduce a known retardation to the optical beam, and thus a known degree of elliptical polarization. The input wave plate (known as the Autoretarder) has many purposes. The most commonly quoted purpose for the Autoretarder in this system is to allow the user to obtain  $\Delta$  to a better degree of precision. Since the measurement configuration that the V-VASE uses is the rotating analyzer scheme (seen in Fig 4), in actuality the system measures  $\cos(\Delta)$ , rather than  $\Delta$ , leading to two limitations: if the physical,  $\Delta_{real}$  corresponding to a given film system is  $180^\circ < \Delta_{real} < 360^\circ$ , the system will give a result  $\Delta_{result}$  corresponding to  $\Delta_{result} = 360^\circ - \Delta_{real}$ . The other difficulty associated is that if  $\Delta_{real}$  is near  $180^\circ$  or  $360^\circ$ , then the precision of the measurement becomes poor, since small errors in the measured  $\cos(\Delta)$  near those angles results in large errors when applying an arccosine to obtain  $\Delta$ . More relevant to this work is that usage of the Autoretarder is necessary to obtain the fourth column of the Mueller matrix, since  $S_3$  (see (1.3.2(d))) of our input light polarization must be known, as it relates to the ellipticity of the light polarization as given in (1.3.6).

With the input light beam having a known polarization and incident on the sample, we can now define the lab frame of reference for the polarization states such that  $p$ - and  $s$ -polarized light correspond to electric field oscillations in the horizontal and vertical, respectively. This definition is consistent with the fact that the sample is mounted vertically using the vacuum stage on the V-VASE and the angle of light incidence is controlled by arms that swing in the horizontal plane. After interacting with the sample in question, the light then passes

through a continuously rotating analyzer (linear polarizer), and is finally detected by one of two detectors: a silicon photodiode for wavelengths in the 300 nm to 1100 nm range, and an InGaAs stack for wavelengths in the range of 1100 nm to 1700 nm. The acquired data at this point is then analyzed and plotted by the WVASE32 software, where any regression algorithms depend on the choice of the scan type that the user has defined for a particular scan.

The V-VASE, as supplied, was not equipped with a means for obtaining the complete Mueller matrix, as there is no retarding element at the output of the detection system. As part of this work, a means was developed to deal with this limitation. To explain the procedure, we first must examine the conditions by which the fourth row of the Mueller matrix for a film can be obtained. In general, a film system has a Mueller matrix given by  $\mathbf{M}_{film}$ , and interacts with a Stokes vector  $\mathbf{S}_{input}$ , producing an output Stokes vector  $\mathbf{S}_{output}$ . This can be expressed as:

$$\mathbf{S}_{output} = \mathbf{M}_{film} \mathbf{S}_{input} \quad (2.1.1)$$

Addition of a wave plate with a Mueller matrix  $\mathbf{M}_{waveplate}$ , which interacts with the light after interacting with the film, yields:

$$\mathbf{S}_{output} = \mathbf{M}_{waveplate} \mathbf{M}_{film} \mathbf{S}_{input} \quad (2.1.2)$$

where we can define  $\mathbf{M}$  as being the product  $\mathbf{M}_{waveplate} \mathbf{M}_{film}$ . From the matrix product, that the third row of  $\mathbf{M}$  can be expressed as:

$$\mathbf{M}_{3j} = \sum_{k=1}^4 \mathbf{M}_{waveplate,3k} \mathbf{M}_{film,kj} \quad (2.1.3)$$

Since the goal is to obtain the  $\mathbf{M}_{film,4j}$  elements, we must rewrite (2.1.3) as:

$$\mathbf{M}_{film,4j} = \frac{1}{\mathbf{M}_{waveplate,34}} \left( \mathbf{M}_{3j} - \sum_{k=1}^3 \mathbf{M}_{waveplate,3k} \mathbf{M}_{film,kj} \right) \quad (2.1.4)$$

As was seen in Table 1, an important characteristic of a quarter-wave plate is that its (3,4)<sup>th</sup> element is 1. Unfortunately, due to dispersion, the matrix seen in Table 1 is only true for a certain wavelength; more generally, the wavelength dependent Mueller matrix for a wave plate is given by [82]:

$$\mathbf{M}_{\text{waveplate}}(\lambda) = \begin{pmatrix} 1 & 0 & 0 & 0 \\ 0 & C^2 + S^2 \cos(\delta(\lambda)) & SC(1 - \cos(\delta(\lambda))) & -S \sin(\delta(\lambda)) \\ 0 & SC(1 - \cos(\delta(\lambda))) & S^2 + C^2 \cos(\delta(\lambda)) & C \sin(\delta(\lambda)) \\ 0 & S \sin(\delta(\lambda)) & -C \sin(\delta(\lambda)) & \cos(\delta(\lambda)) \end{pmatrix} \quad (2.1.5a)$$

$$C \equiv \cos(2\phi) \quad (2.1.5b)$$

$$S \equiv \sin(2\phi) \quad (2.1.5c)$$

where  $\delta(\lambda)$  is the retardation of the wave plate for a given wavelength,  $\lambda$ , and  $\phi$  is the fast axis orientation angle measured from the horizontal. A zero-order quarter wave plate at 633 nm (WPQ05M-633, Thor Labs, Inc.) with its fast axis aligned horizontally (*i.e.*,  $M_{24} = 0$  and  $\phi = 0$ ) was found to be sufficient for wavelengths in the range of 400 to 1700 nm, since the  $M_{34}$  component was approximately 0.5 or greater in this band. By calculating the (3,4)<sup>th</sup> element of the Mueller matrix for the wave plate using the dispersion relations for crystalline quartz found in [93], and assuming that the fast axis is aligned along the horizontal, we can then plot this as a function of wavelength as for comparison against the experimentally measured (3,4)<sup>th</sup> element of the wave plate as follows:

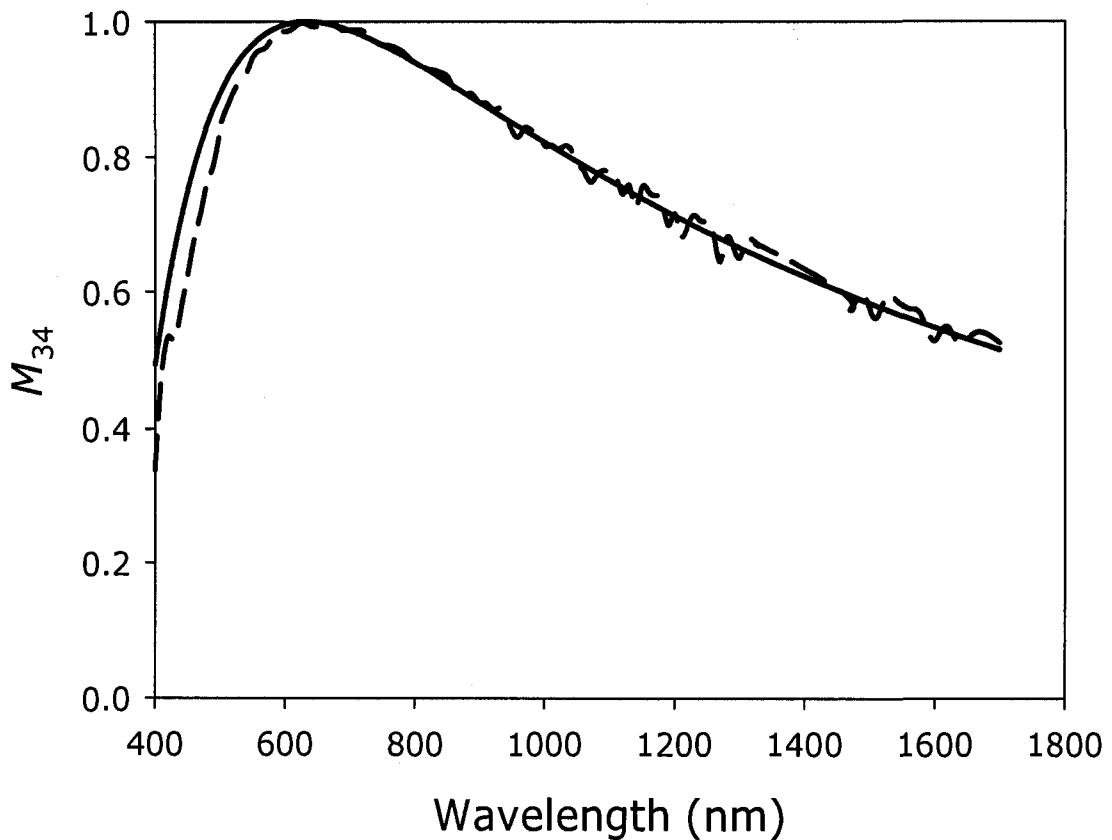


Figure 8 – Experimental (dashed) and theoretical (solid) spectrum for the (3,4)th element of the Mueller matrix for a zero-order quarter-wave plate designed with a quarter wave retardation at 633 nm.

Thus, from this analysis, the fourth row of the Mueller matrix was measured using the following procedure: 1) measuring the first three rows of the normalized Mueller matrix of the sample in reflection mode, 2) measuring  $M_{11}$  to calculate the non-normalized Mueller matrix for the sample (based on the reflectivity of two orthogonal polarization states), 3) inserting the wave plate on the detector arm of the ellipsometer and measuring the first three rows of the normalized Mueller matrix of the film/wave plate combination, 4) using previously measured elements of the first three rows of the non-normalized

transmission Mueller matrix for the wave plate (same procedure as in step 1 and 2) to calculate the fourth row of the non-normalized sample Mueller matrix. For this procedure, an ideal wave plate would have the  $M_{34}$  component of its Mueller matrix be unity for all wavelengths.

## **2.2 – The Modeling Software and Analysis of Films**

The first step necessary in the theoretical modeling of any film system first involves knowledge of the substrate. In this work, the substrates used were one-side polished silicon test wafers (p-type Boron, 3" or 4" diameter, Evergreen Semiconductor), fused silica glass, 0211 Corning glass, and 7059 Corning glass. Substrates models throughout the course of this study were produced as needed. Thus, whenever a new substrate was used, a scan was performed over the full wavelength range for the bare substrate, and its ellipsometric data could then be used in film-substrate systems.

In the first example, we examine the modeling of the ellipsometric data for a bare silicon wafer. We obtained the optical constants using a standard procedure (WVASE32 Manual). In this procedure, the first step is to acquire the  $\Psi$  and  $\Delta$  data for the silicon over the full spectrum, with two angles of incidence being sufficient. Since the backside of the silicon wafer is unpolished, any transmitted light in the infrared is diffusely scattered and thus does not affect the measured results. Since the thickness of the substrate can be treated as being infinite, there is a one-to-one mapping between  $\Psi$  and  $\Delta$ , and  $n$  and  $k$  (or  $\epsilon_1$  and  $\epsilon_2$  for that matter), as given by the following expression [38]:

$$n_{\text{substrate}} + ik_{\text{substrate}} = n_{\text{air}} \tan \phi_{\text{inc}} \sqrt{1 - \frac{4\rho \sin^2(\phi_{\text{inc}})}{(\rho + 1)^2}} \quad (2.2.1)$$

where  $n_{\text{air}}$  is assumed to be 1,  $\phi_{\text{inc}}$  is the angle of light incidence with respect to substrate normal, and  $\rho$  is that given in (1.2.1). The modeling software is then used to convert the  $\Psi$  and  $\Delta$  pair into an  $n_{\text{substrate}}$  and  $k_{\text{substrate}}$  pair.

The procedure used to obtain the optical constants for glass substrates is based on the same physical principle as above, except that the light reflection contribution from the back side of the substrate must be accounted for, and can be done so in the modeling software. All of the glass optical constants were obtained using a standard recipe (WVASE32 Manual).

Having obtained the substrate optical constants from the “baseline” scans, we could then proceed with modeling the ellipsometric parameters or Mueller matrices for the thin films to be examined. The first step was to define film layers using standard layers available in performing the analysis, and by using a number of layers relevant to the film system being studied.

The first type of layer was the Cauchy layer (Fig. 9) which was used to describe transparent films examined throughout this study. The layer model looks like as follows: The fit parameters  $A_n$ ,  $B_n$ ,  $C_n$ ,  $k$  Amplitude, Exponent, and Band Edge in Fig. 9 correspond to the constants  $A$ ,  $B$ ,  $C$ ,  $D$ ,  $F$  and  $\gamma$ , respectively, given in (1.6.1).



Cauchy Layer, with Urbach Absorption

Layer Name:

Comment:

Thickness:  nm  Fit

An:   Fit

Bn:   Fit

Cn:   Fit

k Amplitude:   Fit

Exponent:   Fit

Band Edge:  nm

Opt Const Fit

n

k

Figure 9 – Parameter window for evaluating films using Cauchy dispersion.

The second example is the General Oscillator Layer (Fig. 10). There are a number of interesting features within this model layer. The first, denoted by (a) in Fig. 10 is a pull-down menu in which we can define the type of Oscillator that we wish to use to describe our film. The second, denoted by (b), is an area in which we can define parameters such as the  $\epsilon_1$  offset (or the value of  $\epsilon_1$  at  $E = \infty$ ). The third, denoted by (c), is where we can include our initial guesses, and fit our oscillator parameters.

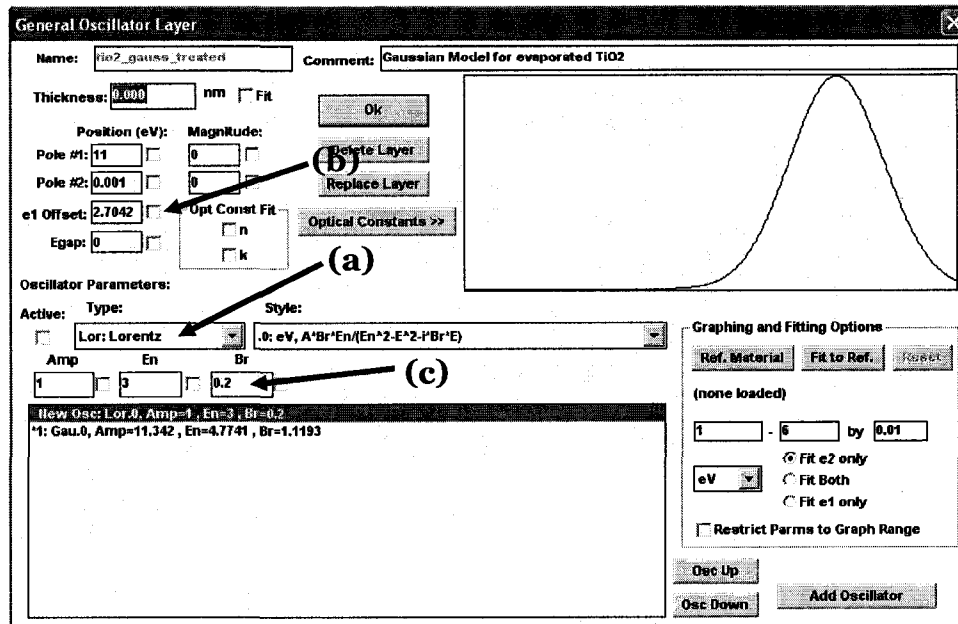
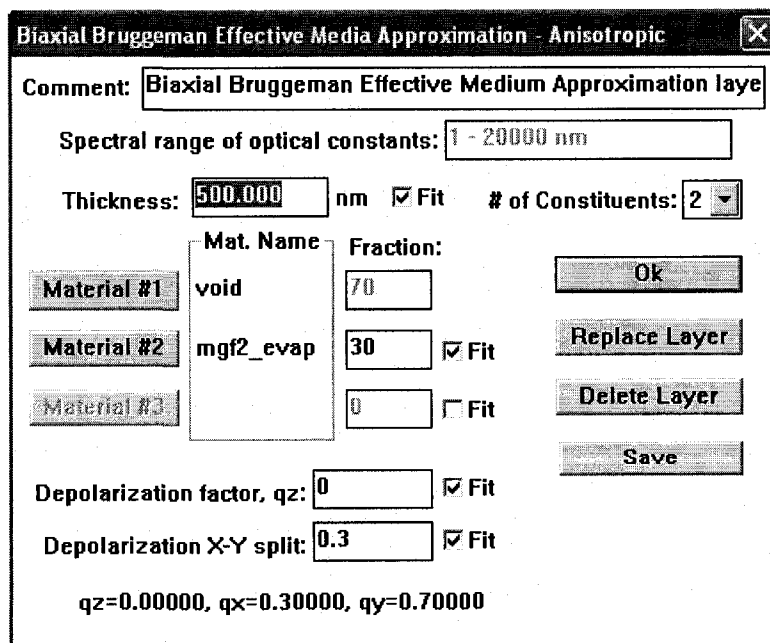
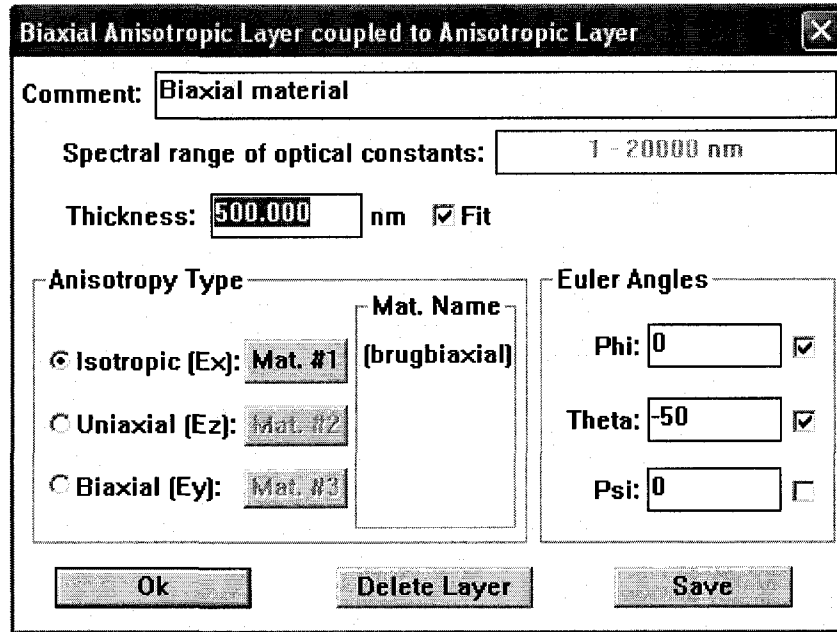


Figure 10 – Parameter window for evaluating general oscillators to describe film dispersion.

To analyze GLAD films, two layer types were used: the biaxial EMA, and the biaxial layer used to define the Euler rotations (like those discussed in §1.5). Examples of these are shown as follows:



(a)



(b)

Figure 11 – Parameter window used to evaluate the film using the BEMA (a) and the column tilt using Euler rotations (b).

As highlighted by Fig. 11(a), the depolarization factors (as in equation (1.4.17)) are evaluated as fit parameters. Furthermore, we note that the depolarization factor along the columns ( $q_z$ ) is approaching a value of 0, consistent with the theory in §1.4. Also shown is that the percentage of material can also be evaluated by fitting it. In the case of tilted columns, we must apply the Euler angle rotations, as highlighted in Fig. 11b.

Best fits of the fit parameters are obtained within the software package using the Marquardt-Levenberg algorithm [94]. This algorithm is used to fit parameters and minimize the Mean Squared Error (MSE) between the experimental and theoretical observables (such as  $\Psi$  and  $\Delta$ ). The expression for the *MSE* for  $N$  data points with experimental error given by  $\sigma$  and  $M$  fit parameters is given by:

$$MSE = \sqrt{\frac{1}{2N - M} \sum_{i=1}^N \left[ \left( \frac{\Psi_i^{Model} - \Psi_i^{Exp}}{\sigma_{\psi,i}^{Exp}} \right)^2 + \left( \frac{\Delta_i^{Model} - \Delta_i^{Exp}}{\sigma_{\Delta,i}^{Exp}} \right)^2 \right]} \quad (2.2.2)$$

To minimize the *MSE*, a physically reasonable model must be developed to represent the experimental data. Furthermore, one must provide a guess on the initial parameters to generate good agreement to the experimental data. Generally speaking, for a given parameter there are fit results to the parameter that are close to the guess. Thus, the fitting algorithm must be able to fit the parameter in a global sense, rather than finding a local minimum to the *MSE*, as illustrated in Fig. 12:

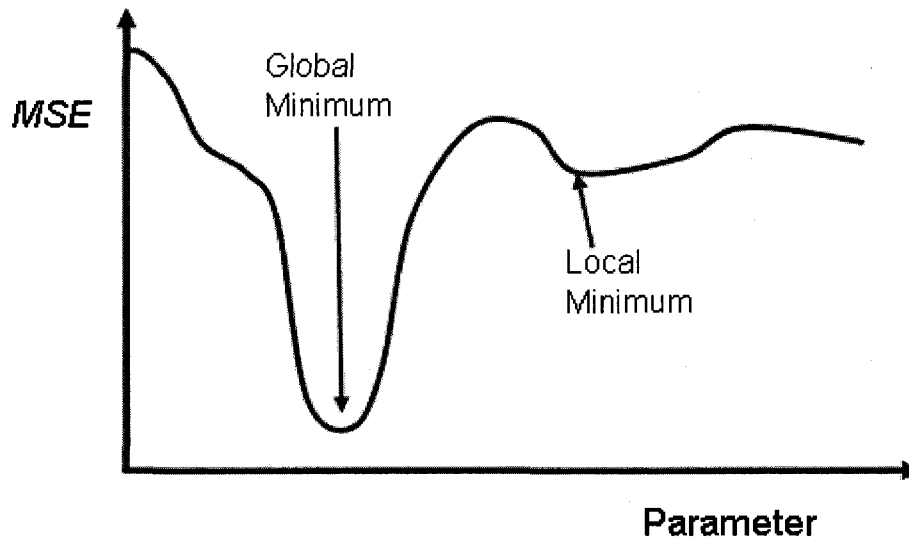


Figure 12 – Illustration of guess values for a given parameter of a film illustrating local and global minima to the *MSE*. Adapted from [39].

Generally, one wants to assume the simplest possible model that best fits the data, and then add more levels of complexity to the model to further reduce *MSE* until either there are no further improvements to be made, or parameter correlation begins to occur. Unfortunately there are instances in which parameter correlation occurs even for the most physically realistic model. When

parameters are correlated there are several results for the two parameters which would yield the same *MSE*. In those cases, other data may be required to justify the correlation. For example, by obtaining the non-optical data to confirm some of the physical parameters of the film (for example SEM images), or by obtaining multiple optical data sets for the film and simultaneously fitting the desired parameters, parameter correlation may be improved or eliminated. In practice, whenever parameter fits were performed in this study, the correlation matrix was examined to see if and which parameters were correlated.

By combining the concepts that were covered throughout this background section, we can describe our GLAD films using material using oscillator theory and effective medium theory, and Berreman's matrix technique to use ellipsometry techniques to obtain parameters of interest in our films.

## **3 – Fundamental Film Examination**

Our examination of GLAD films begins with simple columnar thin films of optically transparent materials and composed of columns tilted with respect to substrate normal. These morphologies form the basis for all GLAD structures, and as such, it is necessary to study their properties first. This is followed by an examination of materials with more complicated optical properties such as TiO<sub>2</sub>. This analysis is used as a basis for advanced analyses including organic Alq<sub>3</sub>, an examination on the subtle optical properties regarding SiO<sub>2</sub>, and films with periodic structure in the plane of the substrate or along substrate normal. These advanced analysis topics will be covered in subsequent chapters of this work.

### ***3.1 – Examination of Slanted MgF<sub>2</sub> and SiO<sub>2</sub> Columns<sup>5</sup>***

Thin films of MgF<sub>2</sub> and SiO<sub>2</sub> were grown by thermal and electron beam evaporation, respectively, at base pressures below  $2 \times 10^{-6}$  Torr ( $3 \times 10^{-4}$  Pa) and evaporant throw distances of approximately 30 cm and 40 cm, respectively onto single-side polished silicon substrates. Films were grown at various flux incidence angles  $\alpha$  resulting in film morphologies ranging from solid ( $\alpha = 0^\circ$ ) to solid tilted columnar ( $0^\circ < \alpha \leq 70^\circ$ ) to porous tilted columnar ( $\alpha \geq 70^\circ$ ). Films grown at normal flux incidence were first characterized using variable angle spectroscopic ellipsometry in order to obtain  $\Psi$  and  $\Delta$ . The solid MgF<sub>2</sub> and SiO<sub>2</sub> films were grown to thicknesses of 620 nm, and 380 nm, respectively. The

---

<sup>5</sup> This section has been largely extracted from: J. Gospodyn and J. C. Sit, "Characterization of dielectric columnar thin films by variable angle Mueller matrix and spectroscopic ellipsometry," *Optical Materials*, vol. 29, pp. 318-325, 2006.

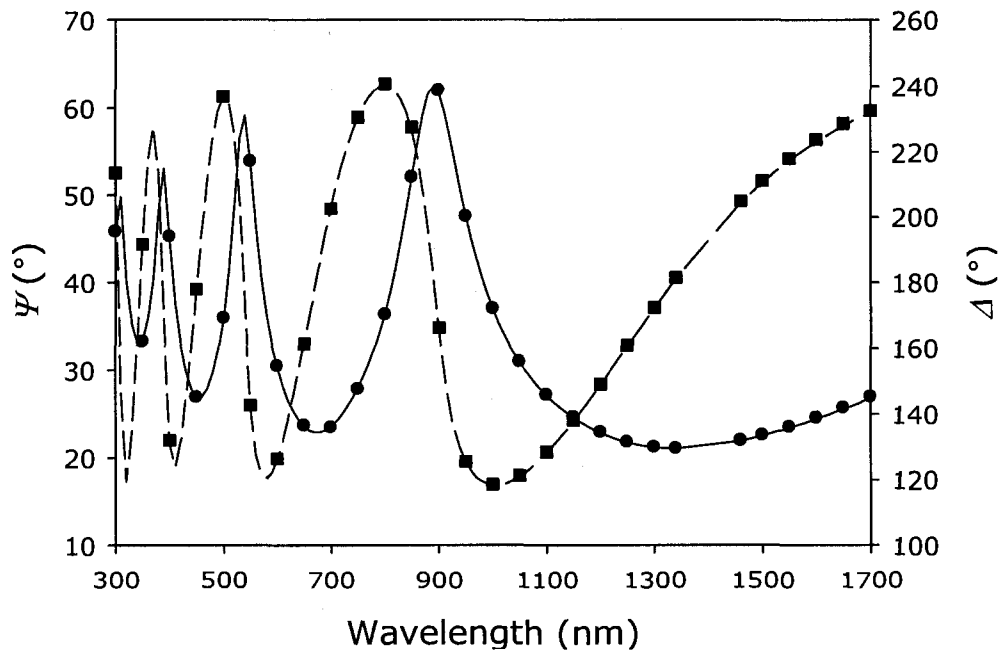
thickness of the solid films was found not to affect appreciably the optical properties of the films, since they were both much thicker than the nucleation layer (sub-50 to 100 nm regime). The optical dispersion relations for the solid films grown at normal flux incidence were found by evaluating the  $\Psi(\lambda)$  and  $\Delta(\lambda)$  ellipsometry data as a medium obeying Cauchy dispersion with a surface roughness layer<sup>6</sup> on top consisting of a Bruggeman effective medium approximation between 50% film material and 50% void with a depolarization factor of 1/3 [39]. The experimental and best-fit models for these solid films are shown in Fig. 13. The additional surface roughness layer had a thickness on the order of only a few nanometres but produced better results with a lower *MSE* and was more physically realistic as the film growth in the Zone 1 regime [62, 63], due to atomic shadowing effects, results in solid, but domed columns that cannot be filled in due to low adatom mobility resulting from low substrate temperature. The refractive index dispersion of the films was described using a two-term Cauchy relation shown in (1.6.1a)

For the MgF<sub>2</sub> film, the constants were found to be  $A = 1.3745 \pm 0.0003$  and  $B = (2.31 \pm 0.02) \times 10^{-3} \mu\text{m}^2$ , and for SiO<sub>2</sub>,  $A = 1.4428 \pm 0.0004$  and  $B = (4.36 \pm 0.04) \times 10^{-3} \mu\text{m}^2$  and are plotted in Fig. 14. As with all plots of this nature throughout this work, error bars arising from the precision of the instrument measurements have been left off the graph, as they are of insufficient size as to be

---

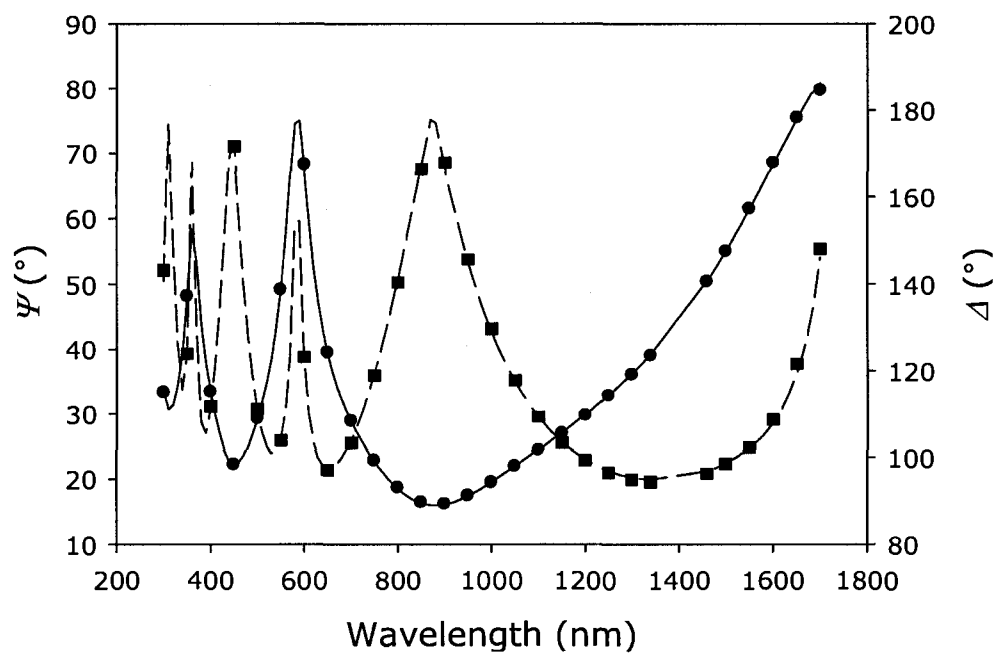
<sup>6</sup> The term “surface roughness layer” is rather misleading, despite its use throughout the literature and this work. More accurately, it should be referred to as an “interfacial layer” that physically represents the fact that the film does not have a perfectly smooth surface, and thus an interfacial layer would be an effective mixture of air and film. The 1/3 depolarization factor is used since the mixture is assumed to be composed of random surface features, and the 50% factor is an arbitrary mixing concentration.

noticeable, as the measurement errors are typically well within a degree for  $\Psi$  and  $\Delta$ . Note here that the stated uncertainties denote 90% confidence limits arising from deviation from the best fit in the least squares fitting algorithm. Using these dispersion relations, it was then assumed that the individual columns of films grown at oblique flux incidence obeyed the same optical dispersion as the films grown at normal incidence. The index of refraction values quoted here for  $\text{MgF}_2$  and  $\text{SiO}_2$  compare well with literature values of 1.3838 [95] and 1.4655 [96] at a wavelength of 500 nm and 546 nm, respectively. It should be noted at this time that whenever optical constants for bulk films were obtained for any material, said values were always compared with literature values, or standard tables of optical constants such as those found in the works of Palik [97].



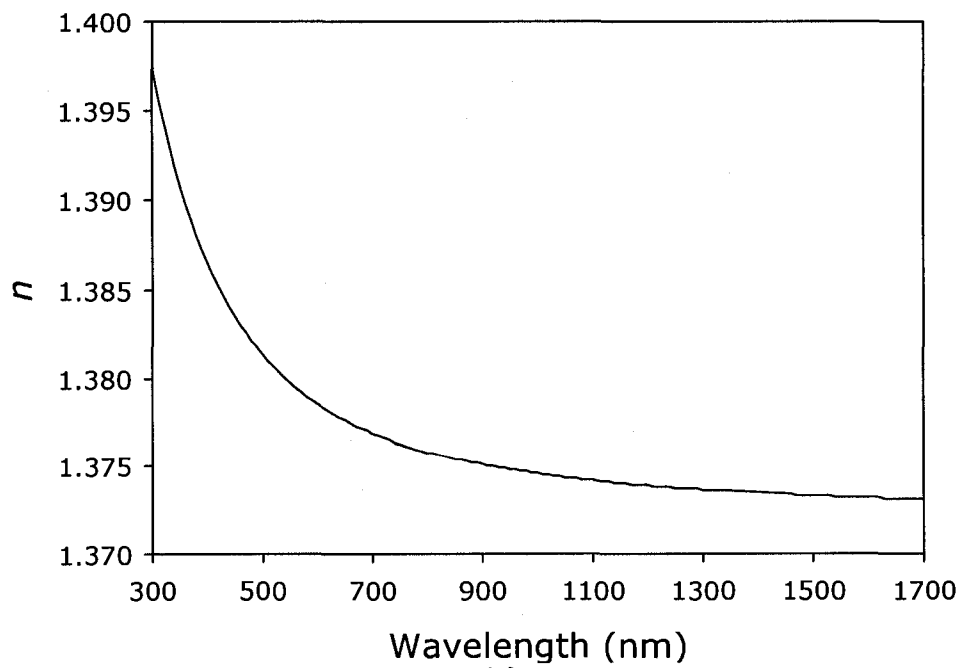
(a)





(b)

Figure 13 – Typical model fits (solid and dashed) to the experimental  $\Psi$  (●) and  $\Delta$  (■) using the Cauchy dispersion for the solid films composed of  $\text{MgF}_2$  (a) and  $\text{SiO}_2$  (b). For the sake of clarity, only every 5<sup>th</sup> experimental data point is shown, and only one angle of incidence is shown ( $60^\circ$  for (a) and  $65^\circ$  for (b)).



(a)

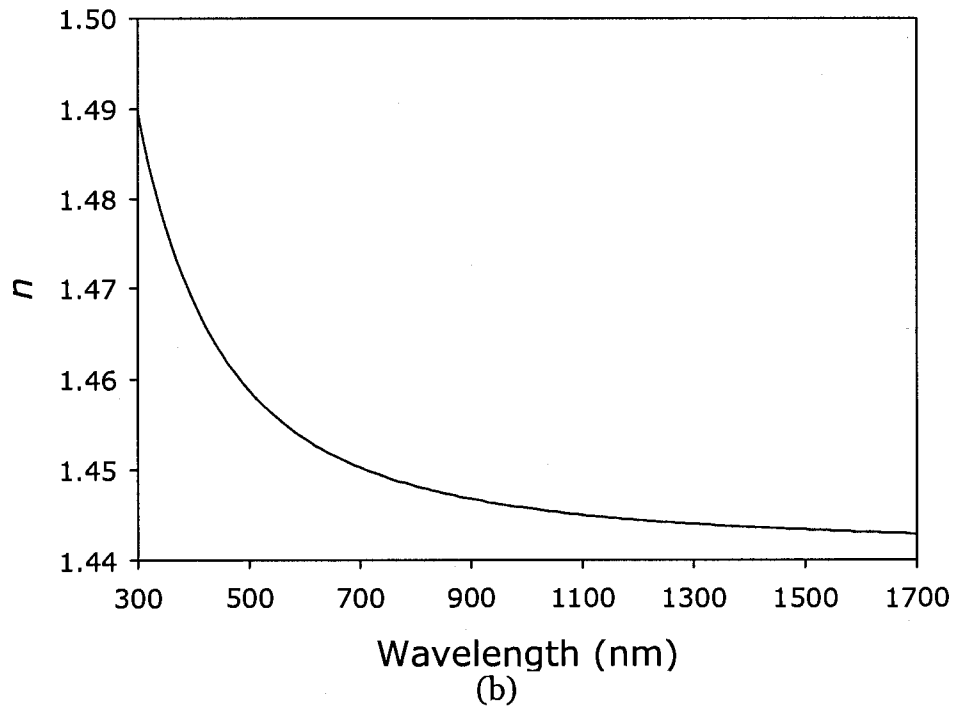
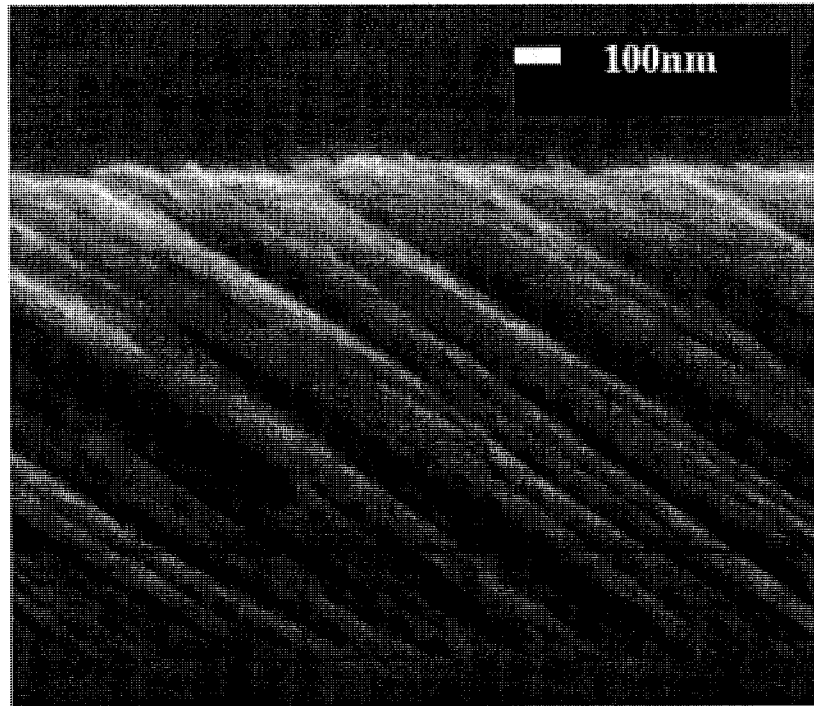


Figure 14 – Resultant optical constants for the solid films composed of  $\text{MgF}_2$  (a) and  $\text{SiO}_2$  (b) using the evaluation template in Figure 9.



(a)

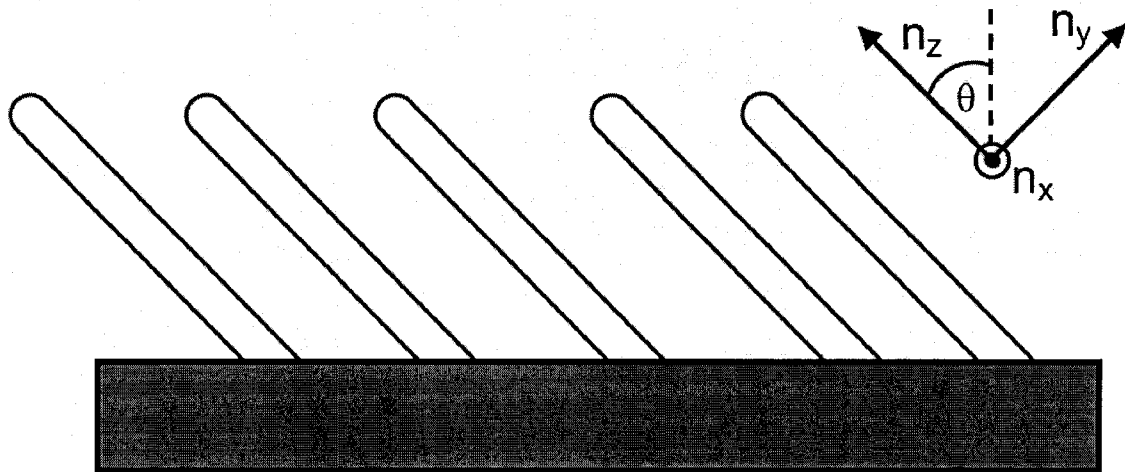


Figure 15 – Scanning electron microscope image of a 1000 nm thick MgF<sub>2</sub> columnar thin film grown at a deposition angle of 84° with respect to substrate normal (a) and an illustration of the directions of the principal indices of refraction (b).

Having obtained the optical dispersion of the film material, obliquely deposited films could subsequently be examined. To evaluate the Mueller matrix data for the columnar thin films (an example of which is shown in Fig. 15 along with a schematic illustrating the orientation of the principal indices of refraction) the Bruggeman EMA in the evaluation software was employed, where the two constituent media used were void (*i.e.*, the real and imaginary components of the index of refraction are  $n = 1$  and  $k = 0$ , respectively) and the appropriate Cauchy relation that represented each film material as described above. Since the films are biaxial media, the model was composed of directionally dependent Bruggeman EMA, where the percentage of material in the model was constrained to be equal in all directions for a given point in the film. The birefringence in this case arises due to the shape of the inclusions along each principal axis, leading to anisotropic depolarization factors as seen in (1.4.17). It was also found that including a symmetric index gradient in the evaluation of the SiO<sub>2</sub> columnar thin

films significantly improved the quality of the model fit. Including an index gradient for the  $\text{MgF}_2$  films was also attempted but was found not to significantly improve the quality of the fit. It also caused significant parameter correlation in the model after fitting. The index gradient in  $\text{SiO}_2$  will be discussed in further detail later.

The  $\text{MgF}_2$  films could thus be modeled as a two-layer film structure. The layer closest to the substrate could be described as a biaxial film with tilted principal axes with respect to the silicon substrate. Additionally, since this layer is a mixture of material columns and void, the anisotropic Bruggeman EMA was used to obtain the biaxial nature of this film layer. Finally, a top film layer on the order of a few nanometres thick in the model describes a decreased density of columns, which physically represents the fact that the columns grow to different heights. Thus, in the film evaluation template for  $\text{MgF}_2$  films, as shown in Fig. 16(a), the  $\text{MgF}_2$  films were evaluated as a tilted biaxial Bruggeman layer medium (labeled BrugBiaxial\_Tilt) on a silicon substrate (labeled Si\_Substrate), with a Bruggeman EMA mixture of 50% void and 50% of the previous layer to describe the post height variation (labeled Surface\_Rough). A similar procedure was used for the evaluation of the  $\text{SiO}_2$  films, with the exception that it was found that there was an index of refraction gradient through the thickness of the  $\text{SiO}_2$  films, the possible source of which will be discussed later. Thus, a symmetric index gradient was included for the  $\text{SiO}_2$  films, where the layer describing the biaxially tilted columns was coupled into a layer describing the index of refraction profile (labeled SimpleGraded). An example of this evaluation template is shown in Fig. 16(b). By using this modeling technique, we can fit for the film density with

respect to those grown at normal incidence, the depolarization factors which describe the shape of the inclusions along each optical axis, the Euler angles  $\theta$  and  $\phi$ , where  $\theta$  is the angle of  $n_z$  (along the columns) with respect to substrate normal, and  $\phi$  is the azimuthal angle describing the orientation of the posts in the plane of the substrate, and the index gradient (where applicable). In the case of the SiO<sub>2</sub> films, the index of refraction predicted by the model corresponds to the density in the vertical center of the film, and thus the density predicted optically also corresponds to this point in the film. For these experiments, although  $\phi$  was fit, it was known to within a few degrees, and the  $\phi$  predicted by the model corresponded to within a few degrees of the known estimate. The alignment of  $\phi$  was done by careful alignment of the substrate with respect to the incoming flux during deposition, and then by a careful alignment of the sample on the ellipsometer sample stage (the major flats of the silicon wafer substrates made this alignment convenient).

2	Surface_Rough	3.982 nm
1	BrugBiaxial_Tilt Void/36.2% MgF <sub>2</sub>	1197.969 nm
0	Si_Substrate	0.25 mm

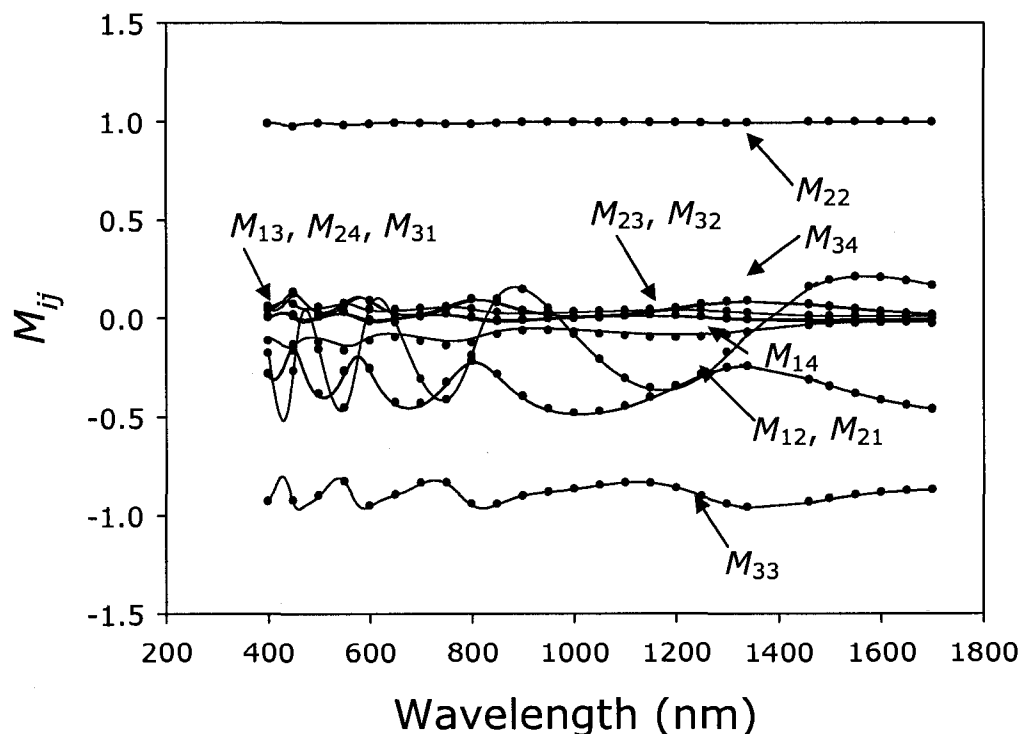
(a)

2	Surface_Rough	14.809 nm
1	SimpleGraded (BrugBiaxial_Tilt)	808.161 nm
0	Si_Substrate	0.25 mm

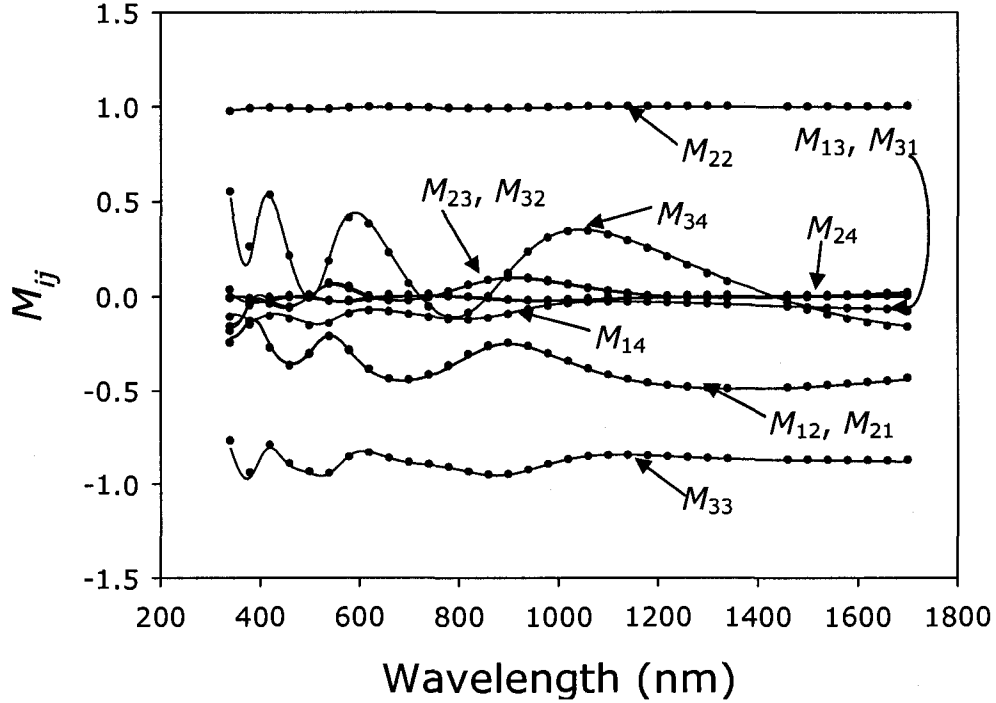
(b)

Figure 16 – Example of the evaluation templates used to describe (a) MgF<sub>2</sub> films and (b) SiO<sub>2</sub> films. The BrugBiaxial\_Tilt layers describe the tilted columns using the anisotropic Bruggemann EMA, the Surface\_Rough layer represents the variation in column height, and the SimpleGraded represents the index of refraction gradient in SiO<sub>2</sub>. The thickness, percent material, Euler angles, and index gradient (for SiO<sub>2</sub> films) were set as fit parameters.

An example of the resultant model and experimental curves for the Mueller matrix data are shown in Fig. 17, where the global mean squared error (*MSE*) in this particular example was 3.072 in the case of a  $\text{MgF}_2$  film grown at  $\alpha = 82^\circ$  (Fig. 17a) and 6.336 in the case of  $\text{SiO}_2$  film also grown at  $\alpha = 82^\circ$  (Fig. 17b). In Fig. 17, both results were acquired using the V-VASE at an angle of incidence of  $50^\circ$  with respect to substrate normal and were only a subset of the full data set acquired in each case, which included other angles of incidence. For the sake of clarity, the data shown in Fig. 17 was restricted to one angle of incidence and only every few data points. The generated data and the experimental result compare well for both film materials studied here.



(a)



(b)

Figure 17 – Comparison between the experimental (●) and generated (–) first 3 rows of the normalized reflection Mueller matrix elements for light incident at an angle of  $50^\circ$  on a  $\text{MgF}_2$  GLAD film grown at  $\alpha = 82^\circ$  (a) and an  $\text{SiO}_2$  film also grown at  $\alpha = 82^\circ$  (b). Only every few experimental data points are shown for the sake of clarity.

It is also important to note that the fourth row of the Mueller matrices was not needed to evaluate these films. It was found that the evaluation software with no data directly measured on the fourth row could accurately predict the normalized fourth row of the Mueller matrix from the model given. This was confirmed by measuring the fourth row of the Mueller matrix afterwards using the technique described in §2.1 and comparing with the fourth row predicted by the model. Though the fourth row of the Mueller matrix may be superfluous information for these simple structures, it may not be for more complicated structures. As was seen in §1.3, the fourth row of the Mueller matrix pertains to circular polarization

rotations. Thus, were one to examine helical film structures, the fourth row of the Mueller matrix would contain vital information for the characterization of those structures. The closeness of the comparison suggested that film parameters determining the fourth row for these films also appear independently in other rows of the Mueller matrix. It was also found that when  $\phi \cong 0^\circ$  or  $90^\circ$  (which was the geometry chosen for these measurements), the matrix elements in the fourth row had the properties  $M_{33} \cong M_{44}$ , and  $M_{j4} \cong -M_{4j}$  for  $j = 1, 2, 3$ . Though the complete Mueller matrix was not needed for a complete model analysis of these films, by obtaining the complete Mueller matrix, we were able to calculate the depolarization index [83] for these films and found that for films in this thickness range, the index was in the range of 0.97 to 1 for all wavelengths, indicating that the light reflected from the samples was polarized.

The resultant *MSE* in evaluating the first three rows of the Mueller matrix data for all of the films ranged from 3.07 to 8.8. The good quality of the fit suggests that there is only a small amount of scattering occurring in some of these films, since the model does not account for scattering. However, by not including the index gradient in the SiO<sub>2</sub> films, the *MSE* values were as high as 19.2. As will be discussed later, this gradient is attributable to scattering of light in the lower wavelengths. The perceived scattering is worse in SiO<sub>2</sub> due to its higher index of refraction. The film thickness and Euler angle  $\theta$  predicted by the evaluation software were confirmed for a sampling of the films by cross sectional SEM images such as that shown in Fig. 15. Furthermore, not including a gradient for the SiO<sub>2</sub> data often yielded a discrepancy in the Euler angle  $\theta$ .



The principal indices of refraction for both MgF<sub>2</sub> and SiO<sub>2</sub> columnar thin films were found to decrease as the deposition angle,  $\alpha$ , increased. This was to be expected due to a decrease in the film density with  $\alpha$  according to simulation predictions [64] as  $\alpha$  increases, which is also consistent with other studies performed on titanium oxide, tantalum oxide, and zirconium oxide [46, 47], which demonstrated that for films grown with  $\alpha < 70^\circ$ , the indices of refraction follow empirical formulae expressible in the form of  $n_i = C_i + D_i\alpha^2$ , where the constants  $C$  and  $D$  describe the indices of refraction for a fixed wavelength as a function of the deposition angle,  $\alpha$  for  $i = x, y, z$ . However, this form was found to be insufficient to describe our data. This may be due to differences in materials deposited. An example of this is the fact that the same works also found uniaxial birefringence for films grown at  $\alpha = 0^\circ$  for their materials of interest. However, this was not found to be the case for the tilted columnar GLAD films studied here. To better describe the functional form of the indices of refraction as a function of deposition angle, we used a semi-empirical expression. To arrive at this expression, we first used an analytical expression that describes the normalized film density,  $\rho$ , as a function of deposition angle,  $\alpha$  [64]:

$$\rho = \frac{2 \cos(\alpha)}{1 + \cos(\alpha)} \quad (3.1.1)$$

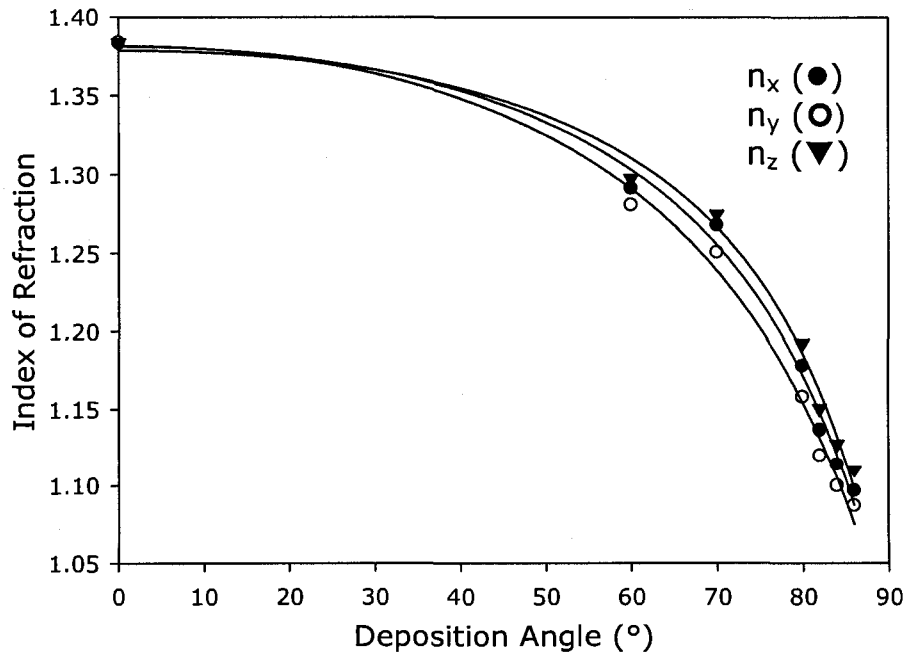
By using (3.1.1), we can then solve the Bruggeman equation [51, 52] for a fixed wavelength as a function of the deposition angle, where the Bruggeman equation for a these films is given by:

$$0 = \rho \frac{\epsilon_1 - \epsilon}{\epsilon_1 + 2\epsilon} + (1 - \rho) \frac{\epsilon_2 - \epsilon}{\epsilon_2 + 2\epsilon} \quad (3.1.2)$$

In this case:  $\varepsilon$ ,  $\varepsilon_1$ , and  $\varepsilon_2$  are the dielectric constants for the effective medium, the film material (*i.e.* MgF<sub>2</sub> or SiO<sub>2</sub>), and air respectively. By combining (3.1.1) and (3.1.2), assuming that  $n_{air} = 1$ , and that the imaginary component of the complex index of refraction  $k = 0$ , and solving for the index of refraction as a function of deposition angle, we obtain:

$$n_i = \sqrt{\frac{E_i \cos(\alpha) + 1}{F_i \cos(\alpha) + 1}} \quad (3.1.3)$$

where  $E_i$  and  $F_i$  are the constants relating to each principal index. The experimental data for the principal indices of refraction for MgF<sub>2</sub> and SiO<sub>2</sub> films as a function of the deposition angle is shown in Fig. 18. The least-squares best-fit are given by the semi-empirical expression (3.1.3). The  $E$  and  $F$  parameters are highlighted in Table 2 for the MgF<sub>2</sub> and SiO<sub>2</sub> films. The  $R^2$  values for these fits were found to be 0.9999 or greater.



(a)

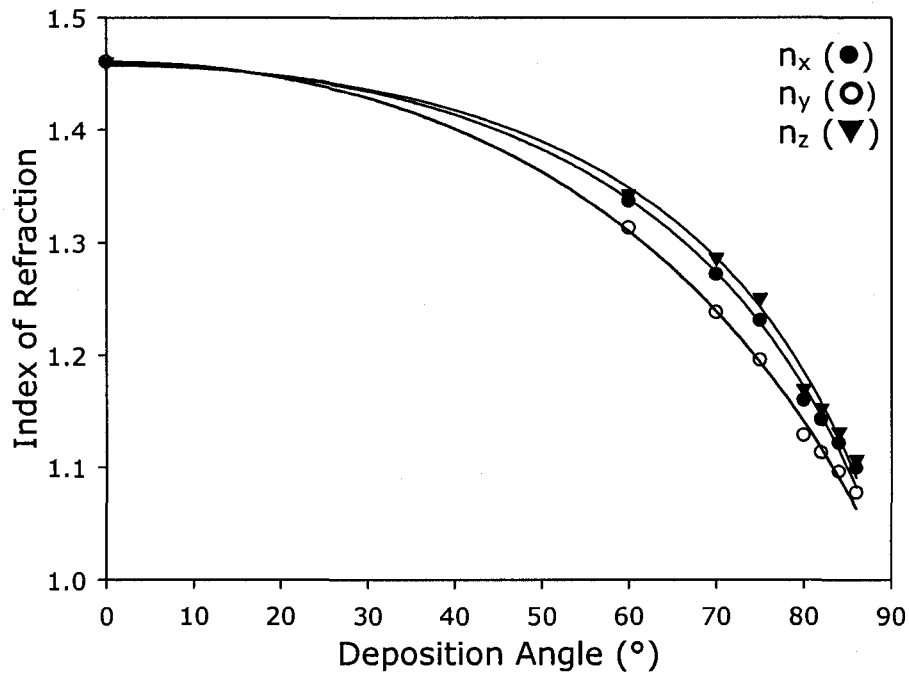


Figure 18 – Magnitude of the principal indices of refraction for  $\text{MgF}_2$  columnar thin films (a) and at the 50% growth point for  $\text{SiO}_2$  columnar thin films (b) as a function of deposition angle. The curves are fits to the semi-empirical law.

	$E_x$	$F_x$	$E_y$	$F_y$	$E_z$	$F_z$
$\text{MgF}_2$	5.369 (0.451)	2.339 (0.268)	4.257 (0.361)	1.754 (0.214)	6.447 (0.547)	2.918 (0.325)
$\text{SiO}_2$	4.029 (0.238)	1.365 (0.131)	2.669 (0.151)	0.720 (0.083)	4.705 (0.304)	1.686 (0.168)

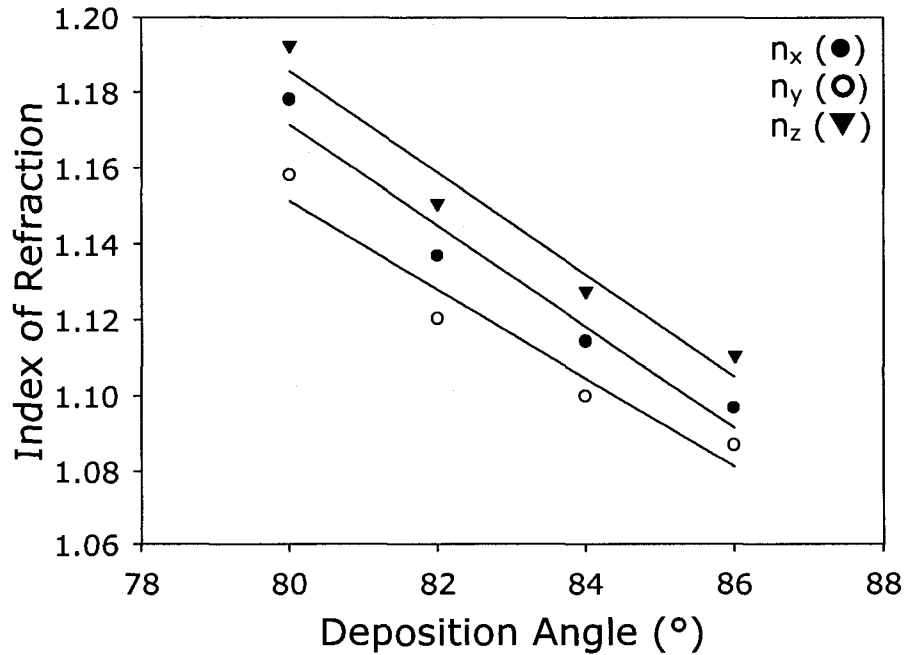
Table 2 – Semi-empirical parameters for the best-fit least squares fit for the principal indices of refraction as a function of deposition angle. The numbers in parentheses are the  $1\sigma$  standard deviation for the parameter.

Since the biaxial optical properties of the columnar thin films arise from the shapes of the inclusions, the values of the index of refraction are determined by the fitting depolarization factors,  $q_i$ , for each optical axis. Note here that the value of  $n_z$  is the highest in both cases. This is due to the fact that the structure in this direction can be viewed as laminar [52] with the electric field of the light being parallel to the material layer. Thus the measured depolarization factor

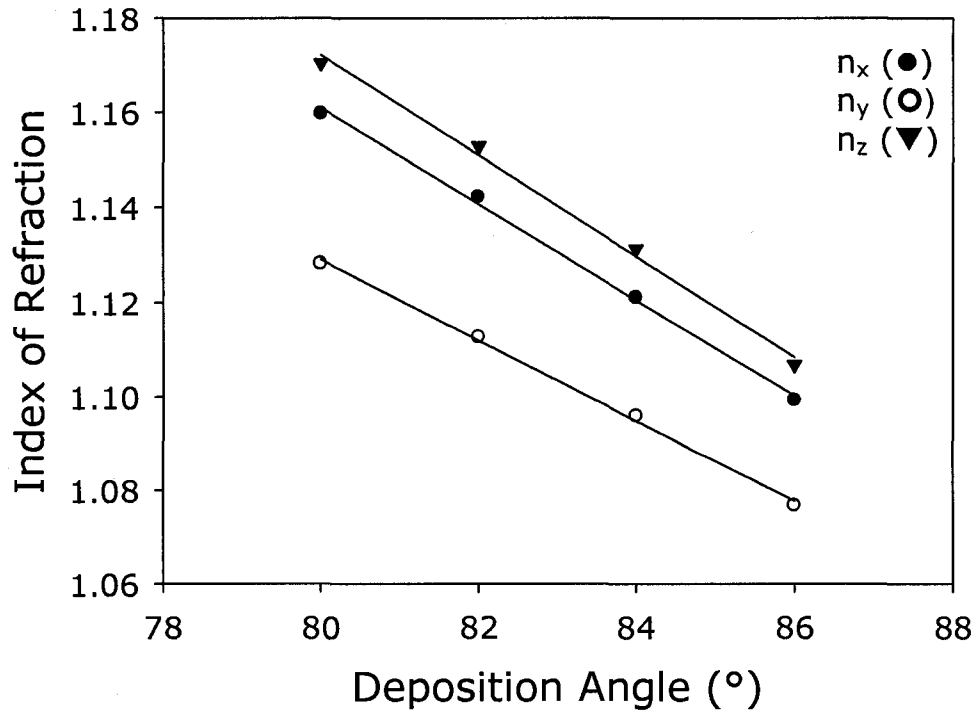
along this axis is  $q_z \cong 0$ , with the sum of  $q_x$  and  $q_y$  being the difference of  $q_z$  from 1. Thus in the model,  $q_z$  was one fit parameter, was typically between 0.01 and 0.1, and the ratio of  $q_x$  to  $q_y$  was another fit parameter, which was typically 0.3 after fitting. As a result, the hierarchy of the values of the indices of refraction was  $n_z > n_x > n_y$  (Fig. 15(b)). If we now focus primarily on the index values obtained for films grown in the GLAD regime  $80^\circ \leq \alpha \leq 86^\circ$ , the relations describing the values of the principal indices at a wavelength of 500 nm as a function of deposition angle are approximately linear. This result is shown in Fig. 19 along with the lines corresponding to a least squares fit to the relations of the following form:

$$n_i = H_i + I_i \alpha \quad (3.1.4)$$

where the parameters  $H$  and  $I$  are summarized in Table 3.



(a)



(b)

Figure 19 – Magnitude of the principal indices of refraction for  $\text{MgF}_2$  columnar thin films (a) and at the 50% growth point for  $\text{SiO}_2$  columnar thin films (b) as a function of deposition angle for deposition angles  $\geq 80^\circ$ . The lines are empirical linear fits.

	$H_x$	$I_x$ (deg <sup>-1</sup> )	$H_y$	$I_y$ (deg <sup>-1</sup> )	$H_z$	$I_z$ (deg <sup>-1</sup> )
$\text{MgF}_2$	2.237 (0.160)	-0.013 (0.002)	2.085 (0.166)	-0.012 (0.002)	2.260 (0.169)	-0.013 (0.002)
$\text{SiO}_2$	1.970 (0.030)	-0.0101 (0.0004)	1.813 (0.025)	-0.0085 (0.0003)	2.022 (0.045)	-0.0106 (0.0005)

Table 3– Empirical parameters to the linear fit for the indices of refraction at deposition angles of  $80^\circ$  and higher. The numbers in parentheses are the  $1\sigma$  standard deviation for the parameter.

Using the Bruggeman EMA, the density of the films with respect to films grown at normal incidence was also found using the evaluation software. These values are plotted for both the  $\text{MgF}_2$  films and  $\text{SiO}_2$  films at the 50% growth point in Fig. 20

along with previously reported values predicted by a ballistic deposition simulation and a geometric analysis [64], shown for comparison.

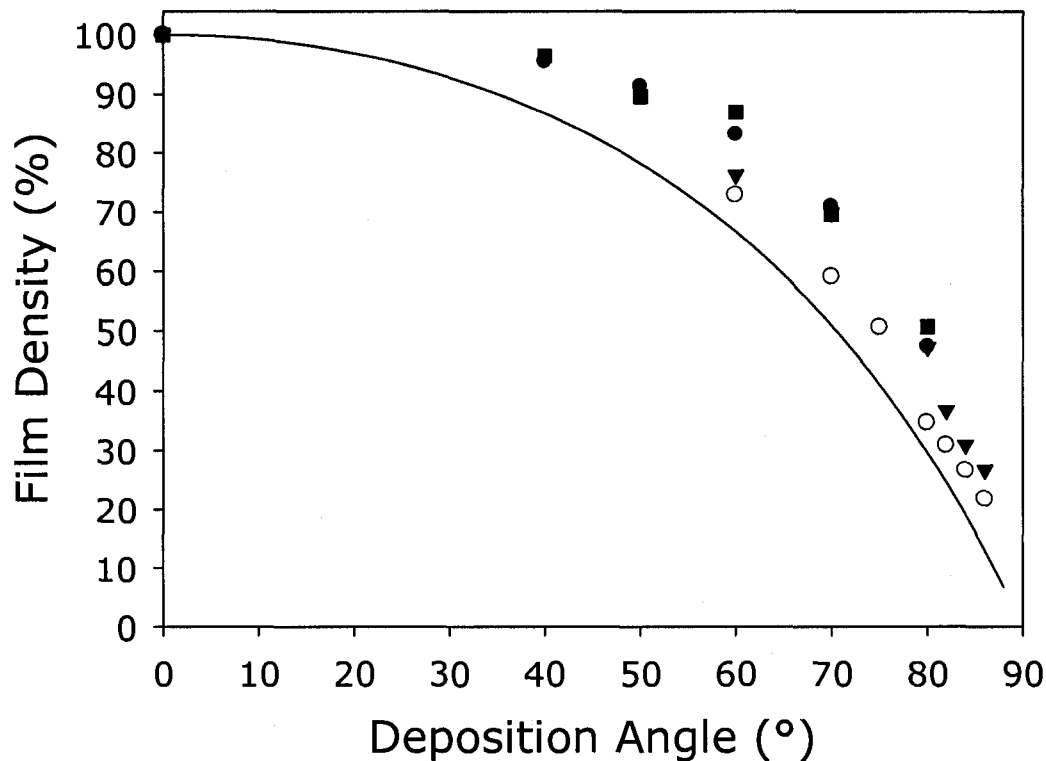


Figure 20 – Film density in percentage as a function of deposition angle for MgF<sub>2</sub> films (▼), the 50% growth point for SiO<sub>2</sub> films (○), and plotted for comparison are simulated result (see Fig. 8 in reference [64]) for 0 diameter diffusion length (●) and 4 diameter diffusion length (■). Also shown is the curve given by (3.1.1).

The results obtained here are in good agreement with those predicted theoretically as they lie within the range of theoretically predicted results. The data points shown by ● and ■ correspond to those predicted by a ballistic simulation SIMBAD [98], which simulates the film growth of two-dimensional hard discs of user-defined diffusion lengths and provides density information. In this particular simulation, surface diffusion of the particles in the ballistic simulation was considered, but diffusion between columns was neglected, as is

consistent with Zone 1 films. For these particular data points, the film particles upon deposition were represented by discs that were assumed to have either a 0 disc diameter diffusion length or a 4 disc diameter diffusion length (see Fig. 8 in reference [64]). Although the results simulated for the 0 and 4 diameter diffusion length do not show that the resultant density is much different, the fact that the SiO<sub>2</sub> density found optically was consistently lower than that of the MgF<sub>2</sub> density found optically was attributed to the fact that the MgF<sub>2</sub> molecules were more mobile along the substrate, thus the columns themselves are more densely packed than the SiO<sub>2</sub> posts, resulting in a higher MgF<sub>2</sub> density. A higher MgF<sub>2</sub> density may also be attributed to a small amount of inter-column diffusion during film growth. Also shown in Fig. 20 is the normalized density (in %) predicted by (3.1.1). It is important to note here that the values of  $\rho$  from (3.1.1) are consistently lower than measured values. This has been attributed to the fact that (3.1.1) is based on an assumption that the film is composed of perfect uniform parallel columns [64]. As seen in Fig. 15(a), this assumption is clearly not true for the films studied here, since the columns tend to broaden as the film gets thicker, especially during the first micrometre of film growth. Furthermore, expression (3.1.1) also assumes a point source and thus would predict that the film density approaches zero as  $\alpha$  approaches 90°. Whereas, the experimental source subtends a parallax angle of approximately 2° and thus would lead to another source of discrepancy, particularly as the experimental  $\alpha$  approaches 90°. Although the density predicted by (3.1.1) does not agree as well with our densities and it was used to derive expression (3.1.3), this was done solely to approximate

the dependence of the index of refraction as a function of deposition angle,  $\alpha$ ; that is, it was used to derive a semi-empirical relation. Further study is needed to evaluate the exact functional dependence. If it could be shown that the packing density of the columns is the same as that for films grown at normal incidence, then expression given by (3.1.1) likely sets a lower bound on film density, and should hold true for films that approach the assumption that the columns are uniform and parallel; however, if the packing density of the columns is lower than that of films grown at normal incidence, then this is not necessarily true. Nevertheless, the shape of the column tips directly affects the film density as atomic shadowing is a determining factor for the film density. A possible source of discrepancy between the actual film density and that measured optically is based on the assumption that the refractive index of the pores is  $n_{void} = 1$ . Although this is approximately the case, the adsorption of water in the pores would serve to increase the overall refractive index in the films, which would in turn increase the apparent density. The optical measurements were performed in a cleanroom environment where both the temperature and humidity were controlled, so any discrepancy arising here would arise in all cases. The broadening of the films may imply that the density of a slice of the film in the plane of the substrate near the substrate would have a different density than that of a slice of film in the plane of the substrate near the top of the film. In the case of  $\text{SiO}_2$  films, using a gradient index model the index of refraction was found to decrease monotonically as the film grows thicker suggesting that the density of the film near the substrate is at its highest value. This gradient however, may also be attributed to other possible causes. One of these could be oxygen



disassociation during the deposition. Another possible cause of the index gradient observed could be capillary condensation in the hydrophilic SiO<sub>2</sub> [99]. That is, since the pore size increases with film thickness, and capillary condensation at a given humidity and temperature will occur in pores with radii smaller than the Kelvin radius [100], more water will be present in the film near the substrate than at the surface of the film. It is important to note that either of these possible causes is consistent with no gradient being observed in the case of MgF<sub>2</sub> films. The cause of the index gradient in the SiO<sub>2</sub> films and the exact functional dependence of the gradient with film thickness are currently under investigation. The existence of an index gradient in the case of the MgF<sub>2</sub> films was not found however, as is demonstrated in Fig. 21. The percentage of MgF<sub>2</sub> compared to films grown at normal incidence, and consequently the index of refraction, was found using the Bruggeman EMA as a function of film thickness for films grown at  $\alpha \cong 79.5^\circ$ ,  $80^\circ$ , and  $80.5^\circ$  with respect to substrate normal. This demonstrates that although the columns broaden as the films become thicker, the film density remains constant. The broadening mechanism has been attributed to column competition and extinction in various stages of growth [17]. The results here in Fig. 21 may not be true for films in the early stages of growth for films with thickness in the sub-100 nm regime, since in the early stages of column growth, nucleation and seeding are factors that determine the density. Further study is under way to quantify the film characteristics in the early stages of growth. It should be noted however, that all films used in this study were approximately 500 nm or thicker, and should obey the trend in Fig. 21. That is, due to column competition, some of the columns that formed in the initial

seeding stage of film growth become extinct, and as a result, columns that persist become broader in the later stages of growth. This result is confirmed by other simulation work, in which the mechanisms of column competition has been examined [101].

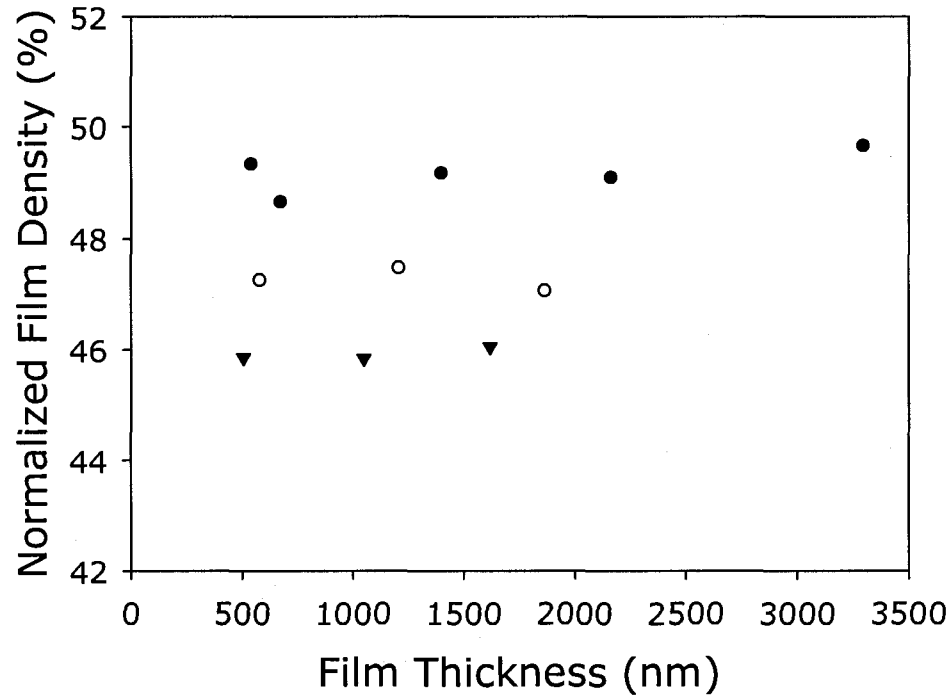


Figure 21– Percentage of MgF<sub>2</sub> with respect to films grown at normal incidence as a function of film thickness as measured by the Bruggeman EMA for films grown at  $\alpha \cong 79.5^\circ$  (●),  $\alpha \cong 80^\circ$  (○), and  $\alpha \cong 80.5^\circ$  (▼) with respect to substrate normal.

The power of this technique is revealed in its ability to calibrate films in terms of index of refraction and in obtaining estimates of film density. This technique was found to be very useful in computing the densities for Al<sub>2</sub>O<sub>3</sub> GLAD films composed of columns oriented along the substrate normal, with application towards GLAD films used for humidity sensing. Using this technique, we are able

to evaluate the film density of  $\text{Al}_2\text{O}_3$  as a function of the deposition angle as [16], and is shown in Fig. 22:

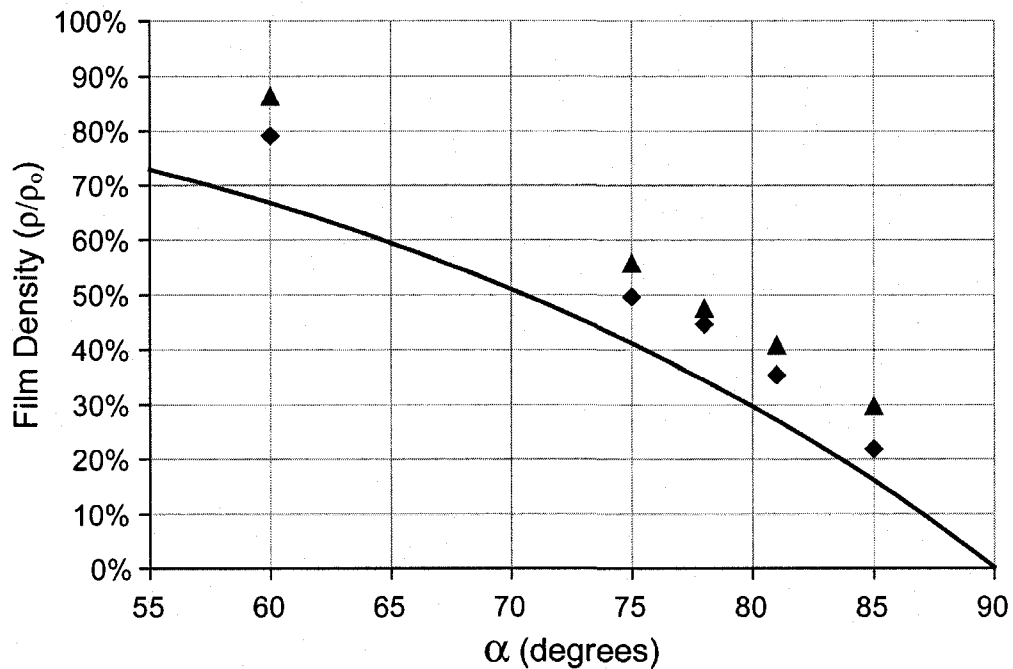


Figure 22 – Thin film density approximations from Tait's rule (—), thickness ratios (◆), and Bruggemann's effective medium theory (▲). From reference [16] ©2006 IEEE.

As can be seen, there is a good agreement between the BEMA model used to obtain the film density and that examined by evaluating the density using resultant film thickness measurements obtained by SEM images, and also by comparing Tait's Rule [64].

### 3.2 – Examination of $\text{TiO}_2$

The analysis technique described in the previous section was subsequently be applied to evaluate a more complex material such as  $\text{TiO}_2$ . The difficulty with  $\text{TiO}_2$  is that it has been observed to have an index of refraction that is dependent on the stoichiometry [102], which has been observed to change over time under

atmospheric conditions [103]. Furthermore, it has been suspected that oxygen depletion of the  $\text{TiO}_2$  source material during electron beam evaporation can cause optical constant change throughout the thickness of a  $\text{TiO}_2$  film. It has been observed that  $\text{TiO}_2$  films that are freshly deposited have different optical constants than those that have been exposed to ambient conditions for some period of time. Empirical studies undertaken within the research group have shown that baking  $\text{TiO}_2$  films in atmosphere at a temperature of  $100^\circ\text{C}$  for approximately 24 hours stabilizes the optical constants to a final value that is consistent with exposure to normal ambient conditions for several days or weeks [103]. In this section, the as-deposited optical properties of  $\text{TiO}_2$  solid films with thicknesses on the order of that of GLAD columns is examined, along with the effect of the baking on the optical properties of the film. This result is then applied to obtaining the film density of  $\text{TiO}_2$  GLAD films as a function of the deposition angle.

In the experiment, a total of 1250 nm of  $\text{TiO}_2$  was deposited all in one deposition, but serially onto eight substrates at normal flux incidence, with only one substrate being exposed to the vapor flux at any given moment during the deposition. The ellipsometric parameters  $\Psi$  and  $\Delta$  were then measured angles of incidence of  $50^\circ$  to  $70^\circ$  over the wavelength range of 300 nm to 1700 nm immediately following the deposition, with all scans made within approximately 30 minutes of removal of samples from the vacuum chamber, which was limited only by the data acquisition speed. The solid  $\text{TiO}_2$  films were found to follow a dispersion related to a Gaussian oscillator centered in the region of 4.75 eV to 4.8117 eV. An example of the best fit for one of the films is given in Fig. 23:

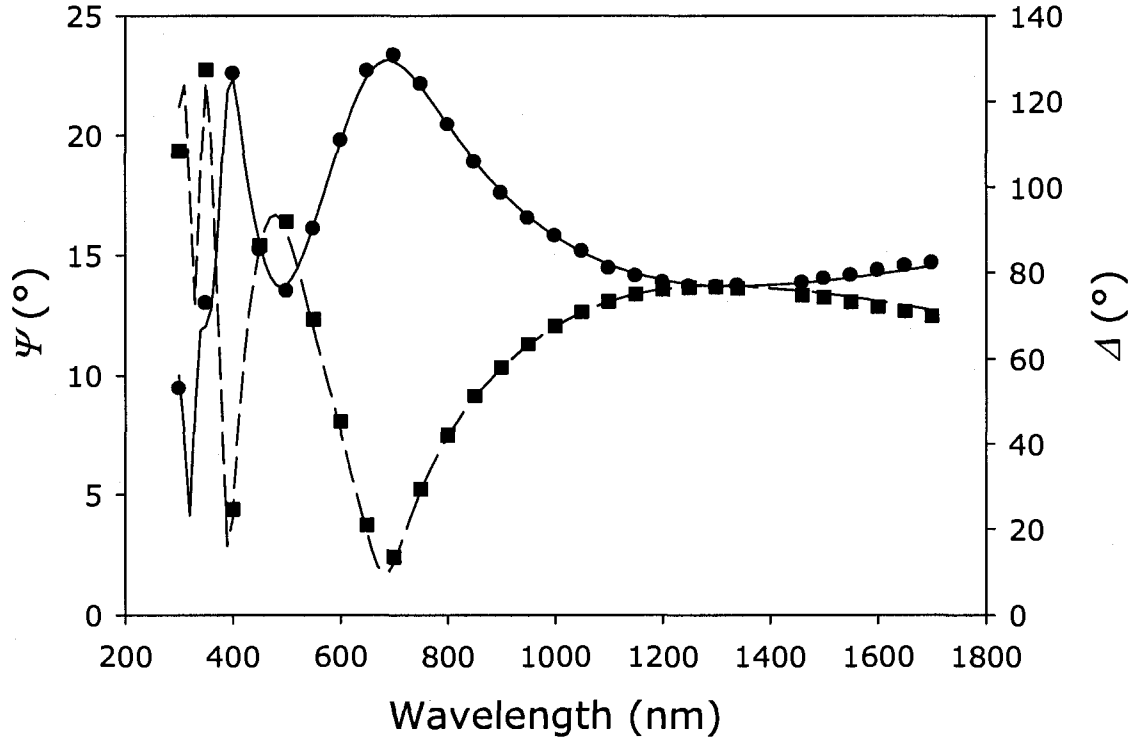


Figure 23 – Best model fits (solid and dashed) to experimental  $\Psi$  (●) and  $\Delta$  (■) for a solid  $\text{TiO}_2$  film using a Gaussian oscillator function. For the sake of clarity, only an angle of incidence of  $70^\circ$  is shown, and only every 5<sup>th</sup> experimental point is shown.

The optical constants for this fit were found using the Gaussian oscillator as it yielded the best agreement with the data as compared with other oscillators. The Gaussian oscillator is defined with an imaginary component of the dielectric constant as follows:

$$\epsilon_2(E) = A \exp\left(-\frac{E - E_n}{B}\right) + A \exp\left(-\frac{E + E_n}{B}\right) \quad (3.2.1a)$$

where for this particular result  $A = 10.338$ ,  $E_n = 4.7477$  eV,  $B = 1.0604$  eV. For the Gaussian oscillator, the real component of the dielectric constant is determined by using the Kramers-Kronig expression (1.6.8a). An  $\epsilon_1$  offset was

also used (see (1.6.9)) with a value of  $\epsilon_{1,\text{offset}} = 2.7103$ . Use of this oscillator resulted in an optical dispersion as shown in Fig. 24:

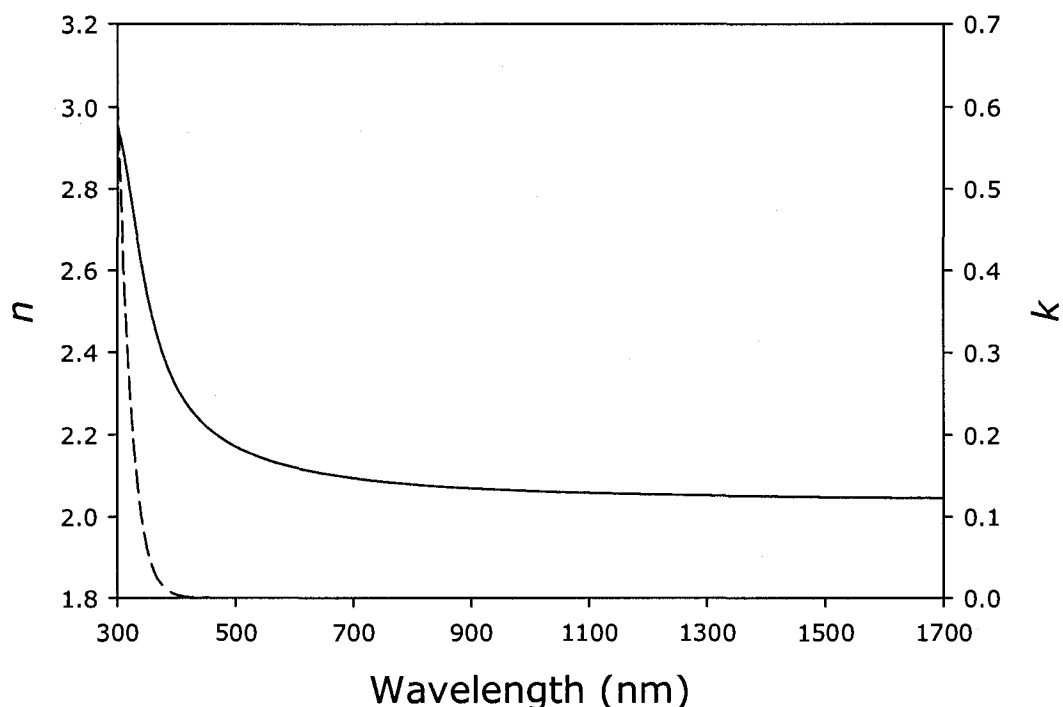


Figure 24 –Index of refraction,  $n$  (solid), and extinction coefficient,  $k$  (dashed), for a solid  $\text{TiO}_2$  film based on the Gaussian Oscillator given in (3.2.1).

Using the above descriptions of  $\text{TiO}_2$ , the resultant index of refraction at 500 nm as a function of the cumulative thickness was found (Fig. 25). For the freshly deposited films, the index of refraction shows a steady increase ( $\bullet$ ). After baking the films at  $100^\circ\text{C}$  for 24 hours in air, the index of refraction was constant over the set of eight films, with discrepancies on the end films ( $\blacksquare$ ). The source of this discrepancy of these two data points is unknown. However, it is clear from this data that the post-deposition treatment on the films acted to stabilize the index of refraction. The index of refraction of the  $\text{TiO}_2$  after treatment was 2.2, while in the case of the as-deposited films, the index of refraction increased over the

course of the deposition. This increase is attributed to oxygen depletion in the source leading to a higher metallic content within the film.

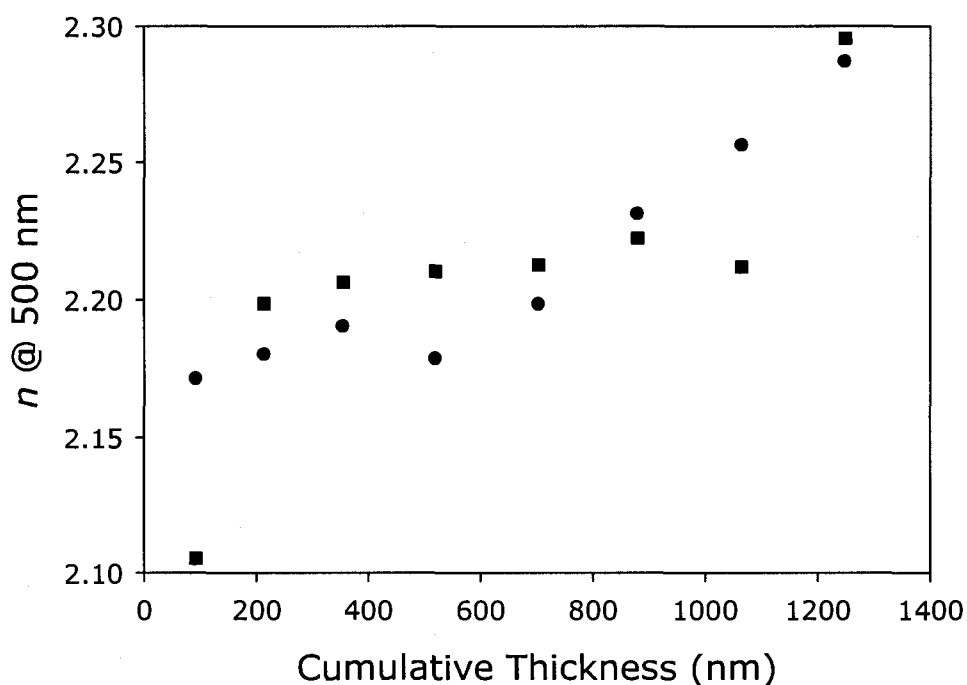


Figure 25 – Index of refraction at a wavelength of 500 nm of the as-deposited solid  $\text{TiO}_2$  films (●) and treated films (■) as a function of the cumulative thickness deposited.

Thus, the optical constants for the aged solid  $\text{TiO}_2$  films could then be used as the basis for the columns within an aged GLAD film. If we also use the BEMA technique discussed in detail throughout this section, the density of the GLAD films relative to those deposited at  $\alpha = 0^\circ$  as a function of the  $\alpha$  may be obtained, as shown in Fig. 26:

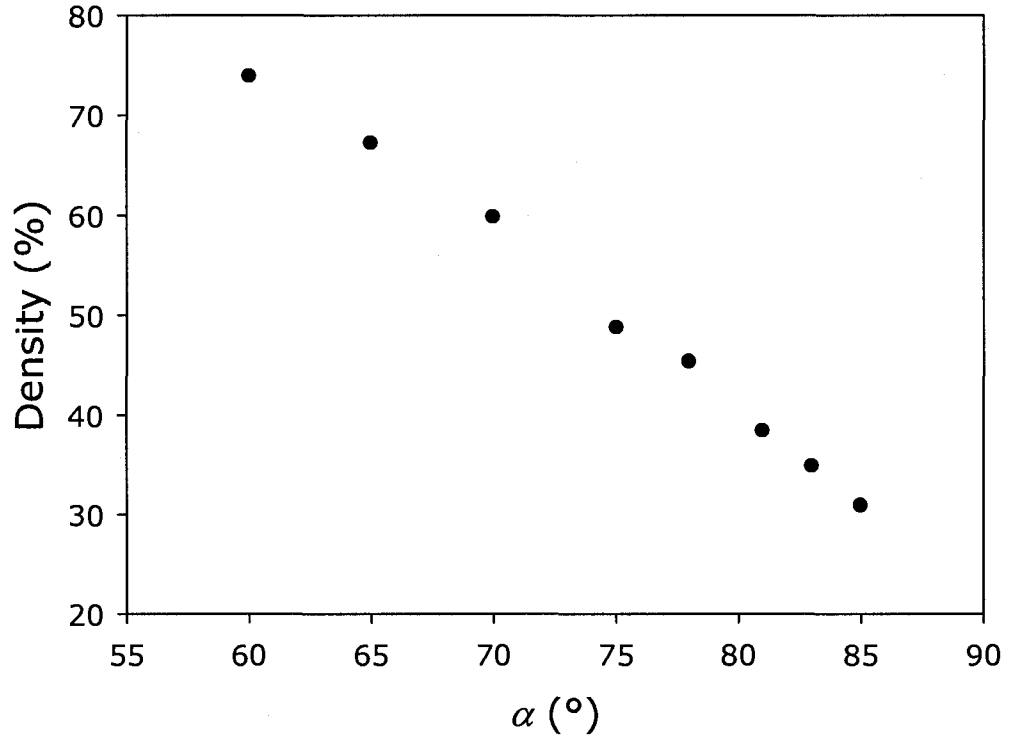


Figure 26 – Density of  $\text{TiO}_2$  as a function of  $\alpha$ .



## 4 – Examination of Organic GLAD Films<sup>7</sup>

Having studied inorganic materials typically used for optical GLAD films, we now turn our attention to the characterization of organic tris(8-hydroxyquinoline) aluminum ( $\text{Alq}_3$ ), an organic photoluminescent material having complicated optical constants in both the visible and near UV. Optical characterization of this material is of particular interest due to its unique growth morphology as compared with inorganic materials. These unique growth characteristics include an absence of column broadening, a more circular column cross-section, and the presence of a “wetting layer” in the nucleation phase of film growth [104-106].

In this study,  $\text{Alq}_3$  powder (99+% purity from Gelest Inc.) was heated to 150°C for several hours under rough vacuum in order to remove water vapor and potential solvents.  $\text{Alq}_3$  films were then deposited by thermal evaporation of the heat treated source material onto as-supplied silicon (100) wafers at a base pressure  $< 8 \times 10^{-5}$  Pa.

Analysis began by examining the solid  $\text{Alq}_3$  film grown at  $\alpha = 0^\circ$ . The ellipsometric parameters  $\Psi$  and  $\Delta$  were obtained over the wavelength range of 400 to 1300 nm for angles of light incidence from 50° to 70° with respect to substrate normal. The normally deposited film was then modelled optically using a Lorentz and Tauc-Lorentz oscillator system, which produced optical constant

---

<sup>7</sup> This section has been adapted to highlight the my contribution to the optical characterization of  $\text{Alq}_3$  in the following work: B. Szeto, P. C. P. Hruday, J. Gospodyn, J. C. Sit, and M. J. Brett, “Obliquely deposited tris(8-hydroxyquinoline) aluminium ( $\text{Alq}_3$ ) biaxial thin films with negative in-plane birefringence,” *J. Opt. A-Pure Appl. Op.*, vol. 9, pp. 457-462, 2007. Journal of Optics A webpage can be found at: [www.iop.org/journals/jopa](http://www.iop.org/journals/jopa)

profiles comparable to previous studies [107, 108], yielding  $n = 1.7343$  and  $k = 0.0026$  at a wavelength of 525 nm, which corresponds well with a values of  $n \cong 1.7$  and  $k \cong 0$  from at the same wavelength as per Figure 2 in reference [108]). The resultant fit for the solid Alq<sub>3</sub> film and the optical constants are shown in Fig. 27 and 28 with the oscillators being given by the following expressions:

$$\varepsilon_{Lorentz}(E) = \frac{ABE_N}{E_N^2 - E^2 - iBE} \quad (4.1a)$$

$$\varepsilon_{2,Tauc-Lorentz}(E) = \begin{cases} \frac{AE_0C(E - E_g)^2}{(E^2 - E_0^2)^2 + C^2E^2} \frac{1}{E} & E > E_g \\ 0 & E \leq E_g \end{cases} \quad (4.1b)$$

where parameters for the Lorentz in (4.1a) are  $A = 36.455$ ,  $E_N = 5.1014$  eV, and  $B = 0.091929$  eV, and the parameters for the Tauc-Lorentz in (4.1b) are  $A = 36.455$ ,  $E_0 = 2.9193$  eV,  $E_G = 2.6524$  eV, and  $C = 0.52233$  eV. The real part of the dielectric constant has  $\varepsilon_{1,offset} = 1.9456$ , and for (4.1b) the real part of the dielectric constant is found by applying the Kramers-Kronig relations (1.6.8a).

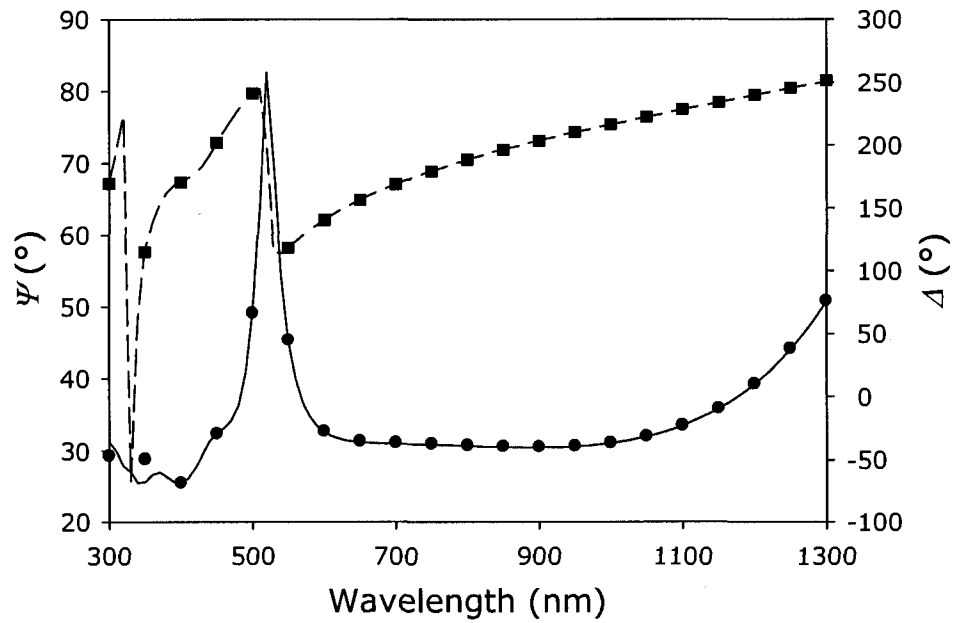


Figure 27 – Best model fits (solid and dashed) to experimental  $\Psi$  (●) and  $\Delta$  (■) for a solid  $\text{Alq}_3$  film using a Lorentz and Tauc-Lorentz oscillator function. For the sake of clarity, only an angle of incidence of  $50^\circ$  is shown, and only every 5<sup>th</sup> experimental point is shown.

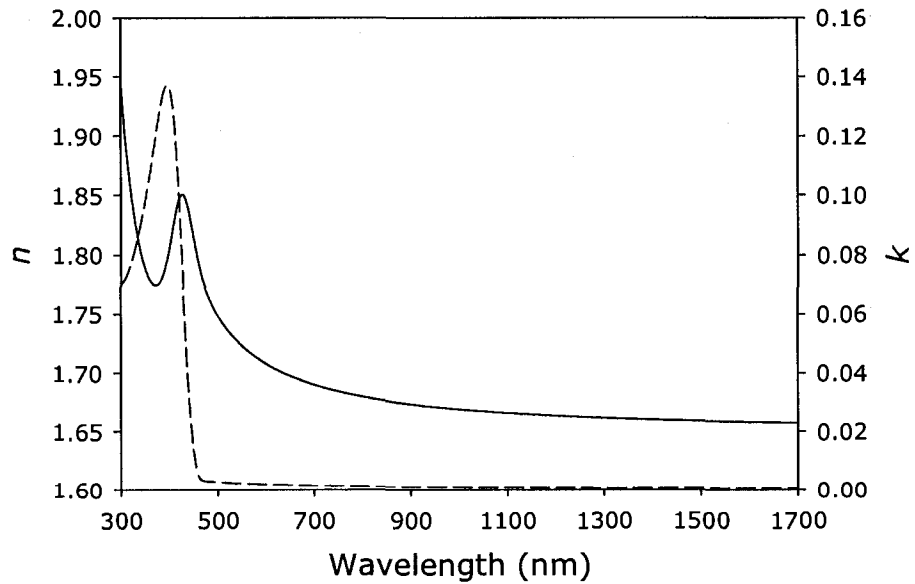


Figure 28 - The index of refraction,  $n$  (solid), and the extinction coefficient,  $k$  (dashed), for a solid  $\text{Alq}_3$  film resultant from the Lorentz and Tauc-Lorentz oscillators given in (4.1).

The obliquely deposited Alq<sub>3</sub> films were modelled using three layers on top of a silicon substrate (Fig. 29). Examples of these films can be seen in Fig. 30. The first layer modelled a solid wetting layer of Alq<sub>3</sub> that forms prior to the growth of individual structures [104]. The second layer described the biaxial slanted posts using the BEMA, where the two constituent media consisted of Alq<sub>3</sub> and void (*i.e.*,  $n_{void} = 1$ ,  $k_{void} = 0$ ). Since the effective medium mixture was anisotropic, we used a BEMA that can account for the cylindrical shaped inclusions [52], as was done previously. The third layer consisted of a surface roughness layer, which was included to compensate for the slight variation in column heights between individual posts. The parameters that were simultaneously fit using the modelling software were the thicknesses of each of the three layers, the film density in the tilted column layer, the screening parameters describing the cylindrical inclusions, and the Euler angles  $\theta$  (which in our case is synonymous with  $\beta$ ) and  $\phi$  which describe the column orientation with respect to the lab coordinate system. The Euler angle,  $\phi$ , is the azimuthal angle that describes the orientation of the columns in the substrate plane. Although the angle  $\phi$  was defined as a fit parameter, it was known to within a few degrees due to careful alignment of the substrates on the deposition system and ellipsometer sample stages. Correspondingly, the model fit for  $\phi$  was always within a few degrees of our estimate.

3	Surface Roughness	29.2 nm
2	Biaxial BEMA, Alq <sub>3</sub> 83.5% / Void 16.5%	612 nm
1	Alq <sub>3</sub> (wetting layer)	269.5 nm
0	Silicon Substrate	0.25 mm

Figure 29 – Multilayer model of columnar thin film deposited at  $\alpha = 71^\circ$

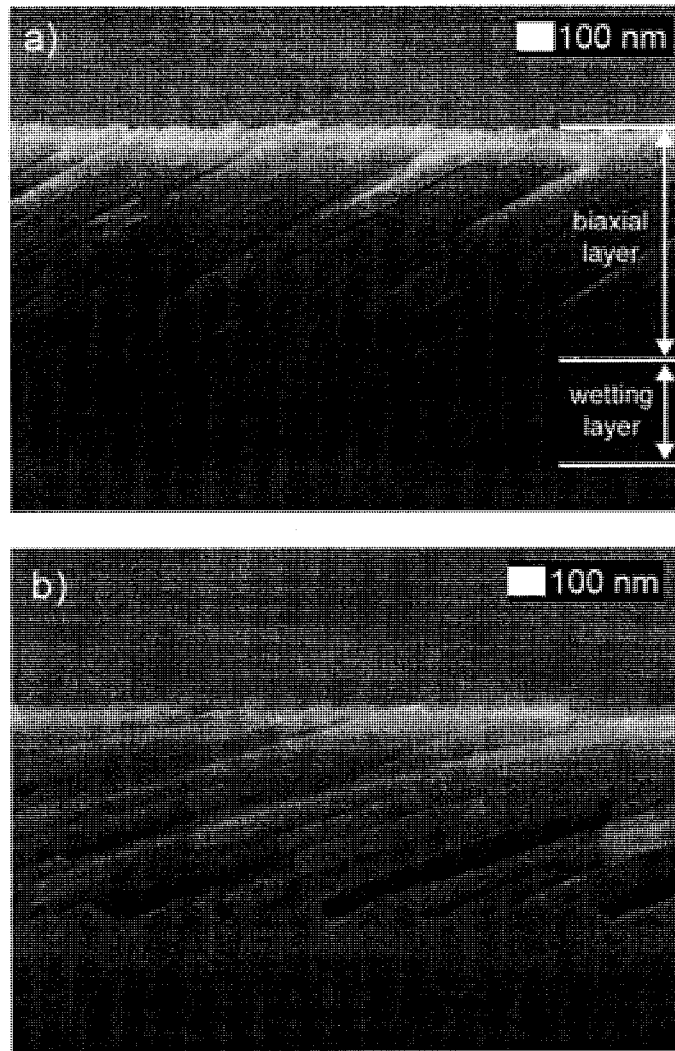


Figure 30 – Cross sectional SEM images of tilted columnar thin films deposited at a)  $\alpha = 71^\circ$  and b)  $\alpha = 85^\circ$ .

From the optical model, we obtained the three principal indices of refraction for the biaxial films, which were defined in the same fashion as in previous chapters and previous studies [46, 47, 50]. By determining the principal indices of refraction, the in-plane birefringence can be calculated using (4.2) and (4.3).

The normalized density of the GLAD layer of the models is shown in Fig. 31 (density compared to the film grown at  $\alpha = 0^\circ$ ) of the biaxial post layer as a

function of deposition angle with the predicted density using Tait's rule [64] included as a guideline. As expected, the film density decreases as the deposition angle is increased due to increased self-shadowing that occurs at higher deposition angles, thus increasing the average spacing between nucleation sites. The result is an increase in the ratio of void to film, which decreases the effective index of refraction of the tilted column layer. The computed values for the three principal indices at a wavelength of  $\lambda = 525$  nm are given in Fig. 32, and as expected, the values of the principal indices of refraction decrease with deposition angle. Furthermore, if we contrast this with the result in Fig. 20, we note that there is a large difference in the density of these films as compared with inorganic columns.

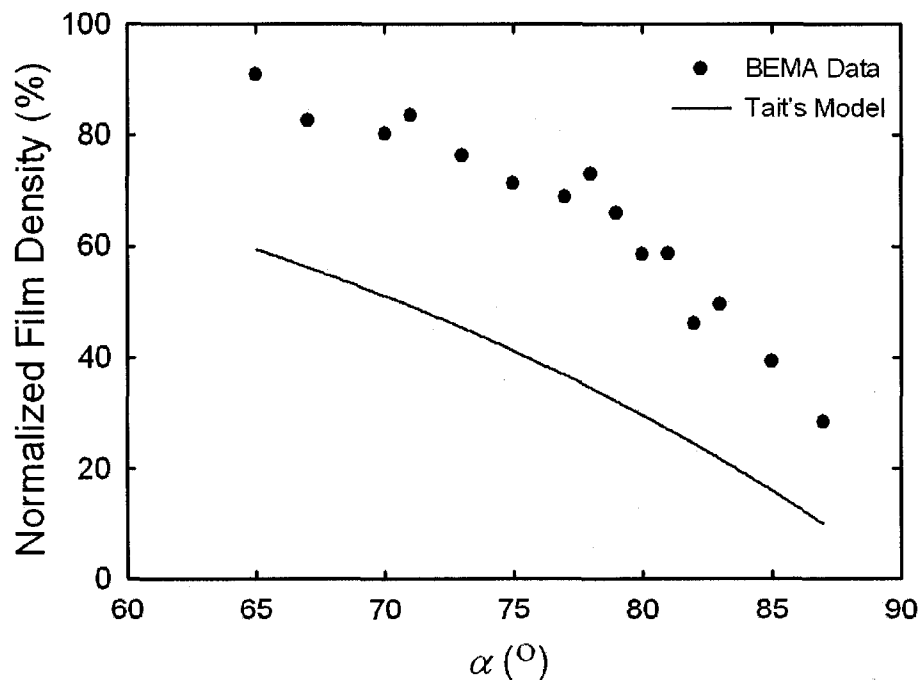


Figure 31 – Normalized film density of the biaxial layer as a function of the deposition angle  $\alpha$ . The density predicted based on Tait's rule (solid line) is shown as a guideline.

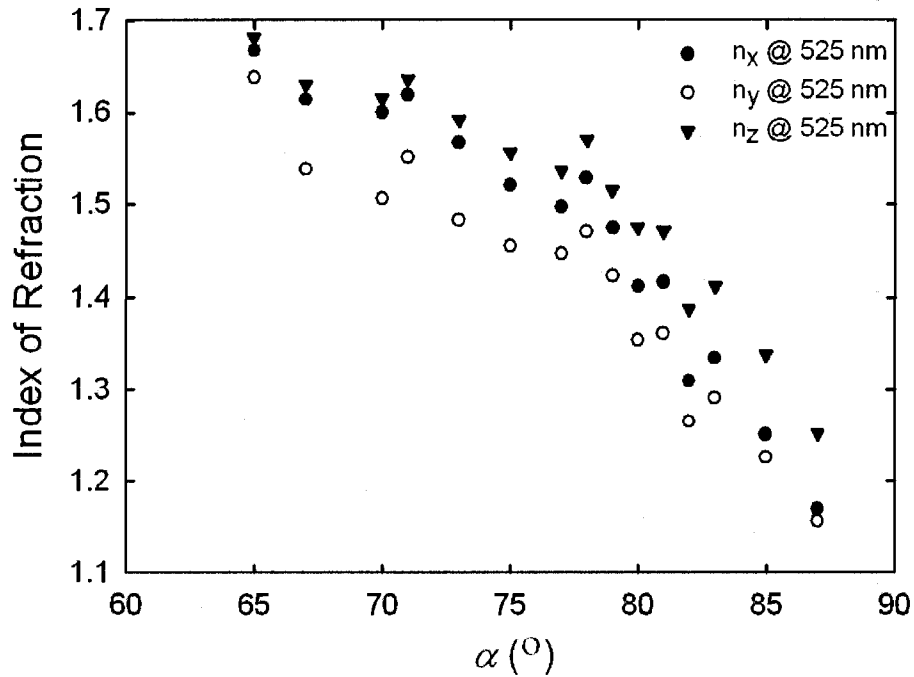


Figure 32 – The principal indices of refraction for the biaxial layer of Alq<sub>3</sub> at a wavelength of 525 nm.

The optical characterization of Alq<sub>3</sub> also yielded useful information pertaining to the morphology of the GLAD produced Alq<sub>3</sub> films as a function of deposition angle. The Alq<sub>3</sub> films deposited at oblique angles of incidence have been shown to exhibit a significant lack of column broadening during film growth and secondary structural anisotropy [104, 105]. The optical properties of chiral Alq<sub>3</sub> films have been studied previously and it was shown that the magnitude of the circular Bragg effects exhibited by such films increased with deposition angle [105]. Given the relationship between in-plane birefringence and the magnitude of the circular Bragg effects of chiral thin films demonstrated previously [71], this trend of stronger circular Bragg effects at higher deposition angles suggests that the in-plane birefringence of tilted columnar Alq<sub>3</sub> films should increase with

deposition angle. Such a trend would be in direct contrast to the situation observed for inorganic tilted columnar films, which exhibit peak values of in-plane birefringence at deposition angles  $60^\circ < \alpha < 70^\circ$  [47].

This is in contrast to films composed of inorganic tilted columnar films, which grow with characteristic elliptical cross-sections [109]. An example of an inorganic silica slanted columnar thin film deposited at  $\alpha = 88^\circ$  is shown in Fig. 33. Column broadening occurs in the individual columns while growth competition effects are visible as the smaller diameter columns in the background which are shadowed by the neighbouring columns and cease to receive any additional incoming vapour flux. When viewed at normal incidence to the substrate plane, the secondary structural anisotropy of inorganic tilted columnar films gives rise to positive in-plane birefringence values according to (4.2), which defines the in-plane birefringence,  $\Delta n$ , as:

$$\Delta n = n_x - n_p \quad (4.2)$$

where the index of refraction in the deposition plane parallel to the substrate,  $n_p$ , is given by:

$$n_p = \left( \frac{\sin^2 \beta}{n_z^2} + \frac{\cos^2 \beta}{n_y^2} \right)^{-1/2} \quad (4.3)$$

and as before,  $n_x$  is in the substrate plane perpendicular to the deposition plane,  $n_y$  is in the deposition plane and perpendicular to the column posts, and  $n_z$  is aligned in the direction of the posts. The in-plane birefringence for the  $\text{Alq}_3$  films is shown in Fig. 34.



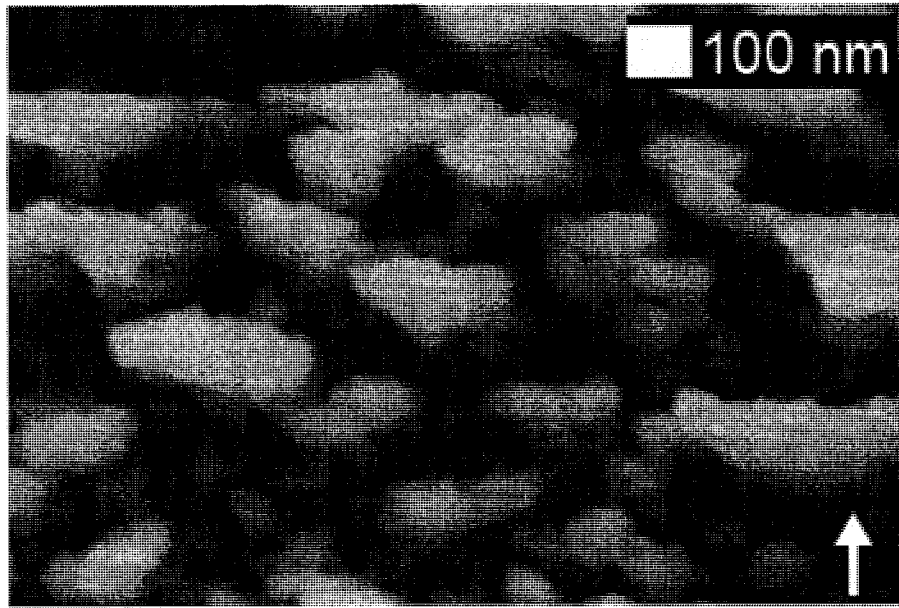


Figure 33 – SEM image of silica slanted columnar thin film deposited at  $\alpha = 88^\circ$  as viewed along the direction of the columns. The white arrow indicates the direction of the incoming vapor flux. Broadening occurs for individual columns while growth competition is observed as smaller diameter columns are visible in the background.

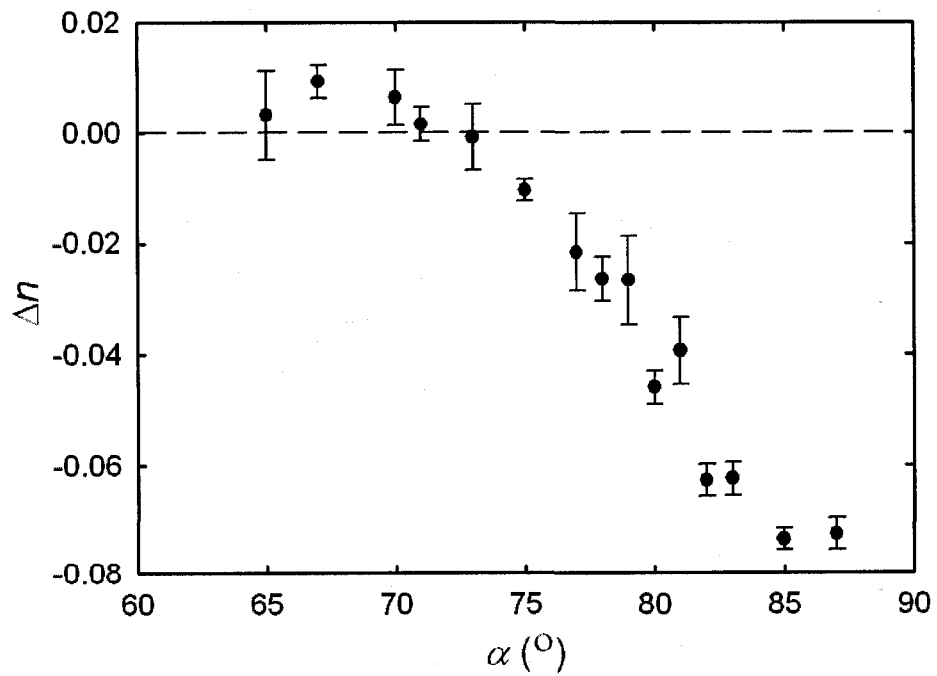


Figure 34 – In-plane birefringence,  $\Delta n$ , shown as a function of deposition angle  $\alpha$ .

At deposition angles  $\alpha > 70^\circ$ , a larger index of refraction in the direction parallel to the deposition plane is measured than perpendicular to the deposition plane ( $n_p > n_x$ ). This negative in-plane birefringence is opposite to the values previously seen in biaxial film studies of inorganic thin films [47, 110, 111] and as discussed earlier in this work. The magnitude of the birefringence showed a generally increasing trend as the deposition angle  $\alpha$  increased, with a maximum negative birefringence of  $-0.073 \pm 0.002$  obtained for the film deposited at  $85^\circ$ . The negative value of the in-plane birefringence is due to the predominantly circular cross-section of individual  $\text{Alq}_3$  columns. The  $\text{Alq}_3$  columns have diameters in the approximate range of 40 to 70 nm which remain constant throughout the thickness of the biaxial film layer. This is combined with the fact that the columns do not exhibit the common broadening. The circular cross-sections cause the variation of the post cross-sectional geometry in the substrate plane to vary as a function of the column tilt angle  $\beta$ . A greater column tilt causes an increase in the length of the major elliptical axis of the columns in the substrate plane whereas the length of the minor elliptical axis perpendicular to the deposition plane remains unchanged and equal to the post diameter. The in-plane anisotropy varies due to the form birefringence of the column cross-sections. As the deposition angle decreases and the overall film density increases, the individual post morphology deteriorates as the individual columnar posts begin to chain together with their neighbouring posts and coalesce, causing the circular cross-sections to merge and a secondary anisotropy to occur in the film perpendicular to the deposition plane (Fig. 36). This phenomenon causes a

change in the form birefringence which is optically similar to column broadening seen in inorganic GLAD films. This results in a decrease in the number of voids between columns and thus an increase in the refractive index perpendicular to the deposition plane, leading to the positive in-plane birefringence values observed in Fig. 34 for  $\alpha < 70^\circ$ . The column melting effect was more prevalent at lower deposition angles (due to film densification and anisotropic shadowing effects) and coupled with the smaller column tilt angle reduced the negative in-plane birefringence. This was observed to be largest in the films deposited at  $67^\circ$  and  $70^\circ$  which measured the largest positive birefringence values.

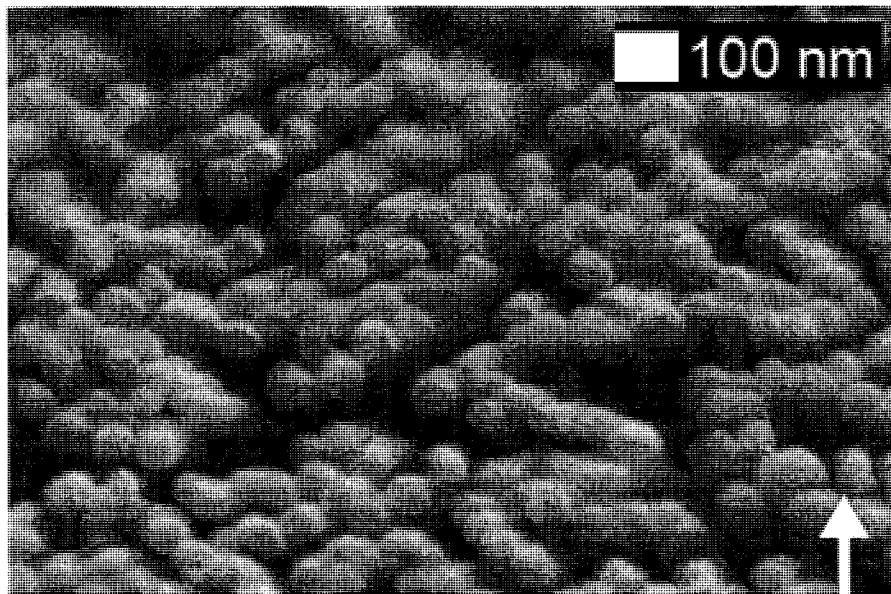


Figure 35 – SEM of the film deposited at  $\alpha = 85^\circ$  as viewed along the direction of the columns. The white arrow indicates the direction of the incoming vapour flux. As can be seen, the column cross-sections are predominantly circular in shape.

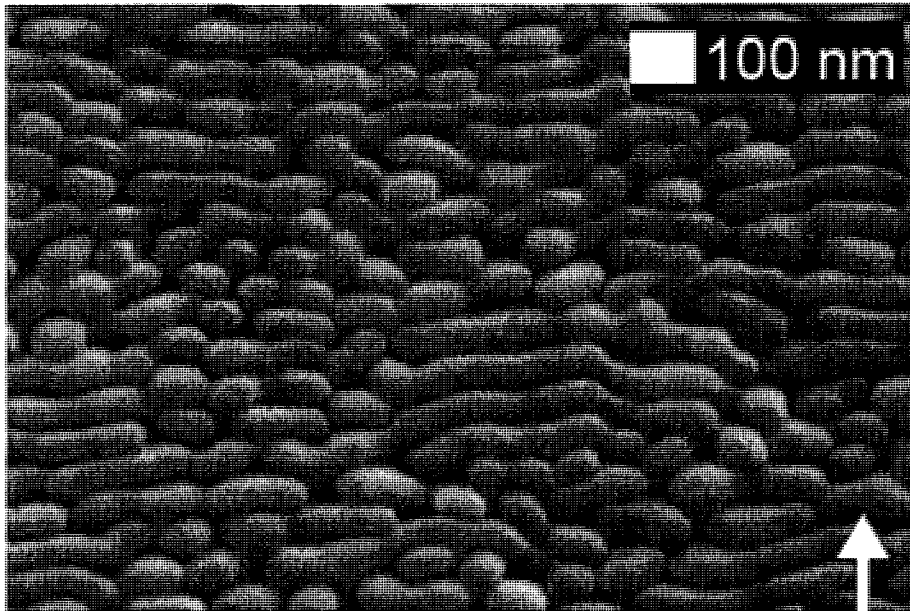


Figure 36 – SEM of the film deposited at  $\alpha = 67^\circ$  along the direction of the post growth. The white arrow indicates the direction of the incoming vapour flux. Individual columns have merged together modifying the cross-section of the columns and decreasing the number of voids.

## 5 – Examination of the Index Gradient

Columns composed of SiO<sub>2</sub> were fabricated at deposition pressures in the range of  $4 \times 10^{-4}$  Pa to  $1 \times 10^{-3}$  Pa onto silicon substrates at a deposition angle of  $\alpha = 85^\circ$ . During the deposition, the  $\phi$  motor was continuously rotated so as to produce columns aligned along the substrate normal. Several series of SiO<sub>2</sub> films were examined using the spectroscopic ellipsometer. Because the films were composed of columns aligned along the substrate normal, for the sake of optical analysis, we used the Bruggeman effective medium approximation, which allowed us to obtain the film density compared with that grown at normal incidence and the screening parameters describing the shapes of the inclusion, as described previously. Because these films were composed of columns aligned along substrate normal, the principal indices denoted previously by  $n_x$  and  $n_y$  degenerate to the same value, and we obtain a uniaxial medium with one principal axis along the columns, and the other in the substrate plane. Examining the quality of the model fits without the inclusion of a gradient index layer; one feature common to all of the results is large discrepancy between experimental and generated data at the lower wavelengths. An example of this can be seen in difference between the experimental and model Mueller matrix elements, shown in Fig. 37 for an 843 nm thick film.

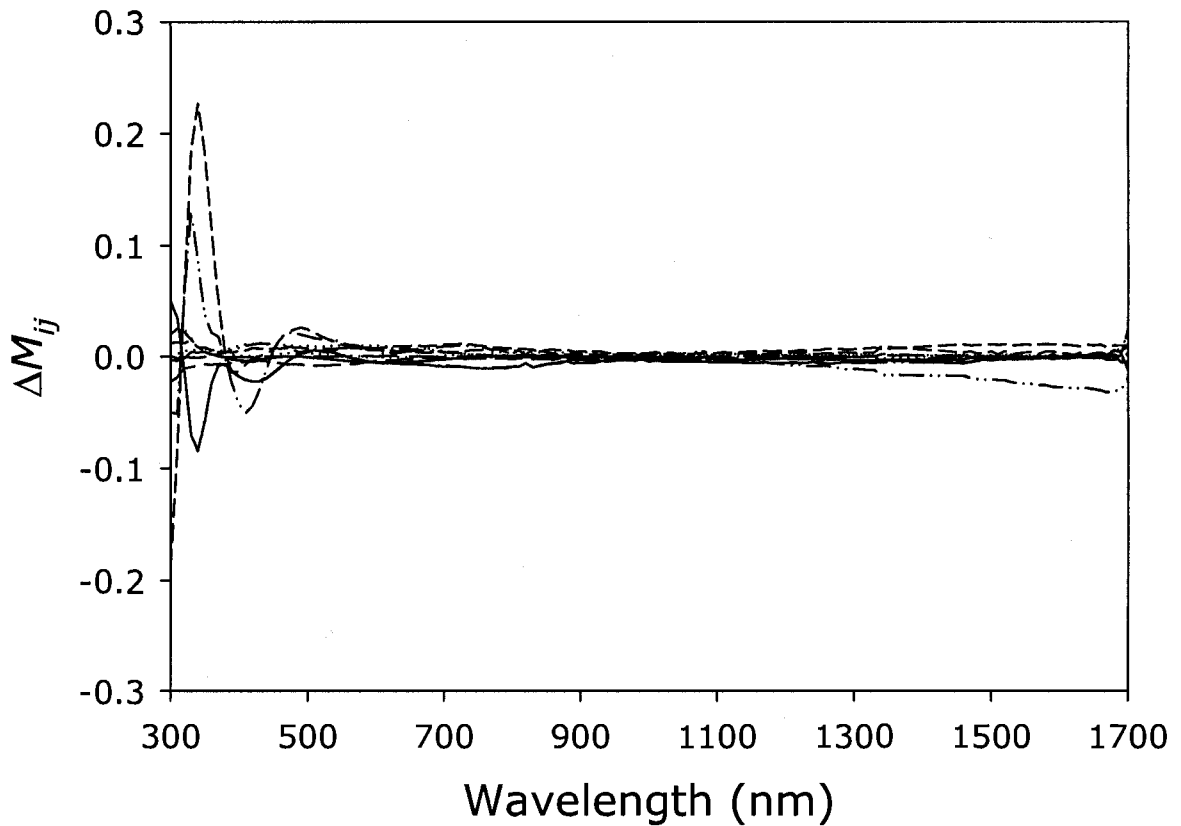


Figure 37 – Difference between the generated and experimental data for a 843 nm thick film.

Including a gradient index layer in the model fits reduced *MSE* from 19 to values ranging between 3 and 8. In this study, the index variation was given by the following function:

$$n(d) = n_{offset} + ad^b \quad (5.1)$$

where  $n_{offset}$  is the shift from the tabulated index value for a given material and  $a$  and  $b$  are constants describing the power-law scaling with thickness  $d$ . We can see an example of the oxide gradient for the indices at the top and bottom of the film in Fig. 38.

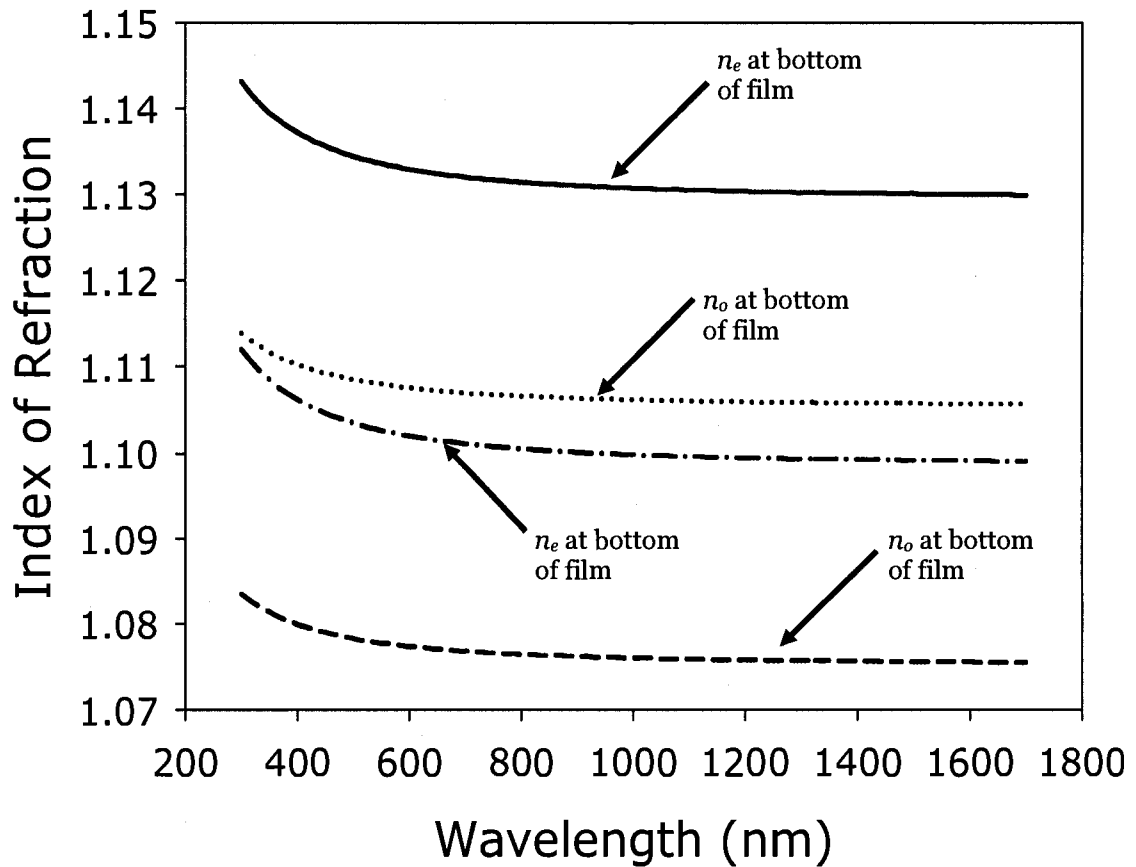


Figure 38 – Index of refraction along the columns at the bottom of the film (solid) and at the top of the film (dash-dot), and the index of refraction in the plane of the substrate at the bottom of the film (dotted) and top of the film (dashed).

Initially, it was thought that the apparent index of refraction gradient in these films was caused by a monotonic increase in the average column size as the film grows due to column broadening. To reduce the column size increase within the film, we also examined the optical properties of a  $\text{SiO}_2$  film that was deposited using the PhiSweep GLAD technique, which has been described briefly in Chapter 1 and detailed in the literature [11]. A characteristic feature of films grown using the PhiSweep technique is a significant reduction in column broadening. This can be seen for the  $\text{SiO}_2$  film examined in this study, shown in Fig. 39.

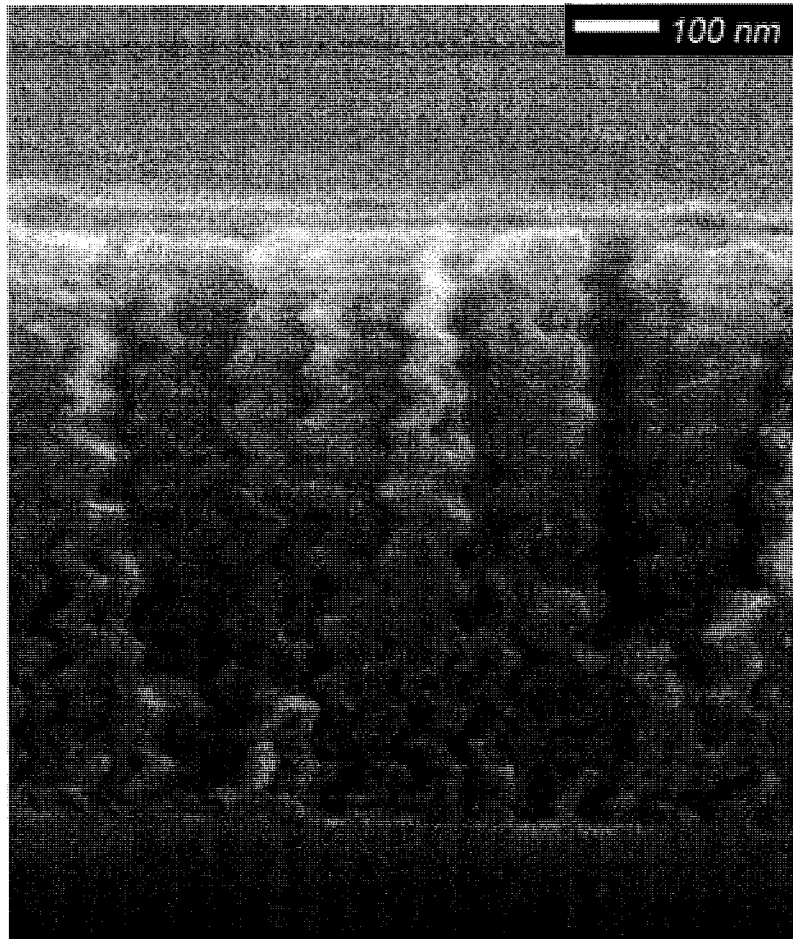


Figure 39 – SiO<sub>2</sub> film produced using the PhiSweep method.

One of the limitations regarding the PhiSweep technique as far as this study is concerned is that it is not possible to orient the columns along substrate normal using the PhiSweep technique, making a direct comparison impossible. The measured index gradient in the PhiSweep produced film was no greater than -0.67%, whereas a film grown using the standard GLAD technique and of similar thickness showed an index gradient of -2.5%. Though this result may suggest that the column size has an impact on the index gradient, there are several other hypotheses for the cause of the index gradient apparent in these films: 1) there is a larger amount of water adsorption in the smaller pores near the substrate due



to the smaller column size, 2) a difference in the amount of light scattering in the various strata of the films, or 3) a depletion or change in the source material during the course of a given deposition. These hypotheses are discussed below. Changes in the column size throughout the films were also examined using FFT image processing of SEM images to obtain quantitative results.

### **5.1 – Adsorption of Water**

The first hypothesis tested was whether or not adsorption of water would affect the apparent gradient. In an attempt to isolate water adsorption in the films as a potential cause of the apparent index gradient, two control tests were performed.

In the first test, films were scanned using the VASE first in an environment of 40% relative humidity (RH). The same measurement was then repeated dry nitrogen blowing on the sample during the measurement. The resultant differences between these two measurements proved to be inconclusive or immeasurable. This result is not inconsistent with other works which studied extensively the effect of relative humidity on the capacitance and properties of GLAD-produced oxide films [16, 112]. It has been shown that for vertical columns composed of  $\text{Al}_2\text{O}_3$  at  $\alpha = 85^\circ$ , the capacitance undergoes a minimal change in the range of 0% RH to 40% RH [16]. It has also been shown that by constructing a spectral hole filter of  $\text{TiO}_2$ , the wavelength that the spectral hole occurs at is dependent on the RH. However, the total shift in the central wavelength of the spectral hole is 14 nm, or 2%, for an RH from 0.3% to 42.3% [112]. This suggests that the average index of refraction in the spectral hole filter

changes by at most 2%, suggesting that any index gradient change would likely be immeasurable using this technique.

In a second test, films were scanned using VASE before and after chemically functionalizing them using self-assembly of hydrophobic siloxanes [99]. This chemical treatment rendered the typically hydrophilic SiO<sub>2</sub> films hydrophobic. Unfortunately, the addition of the functionalization polymer significantly perturbed the overall index of refraction of the films, thus making a direct comparison questionable.

## ***5.2 – Oxygen Depletion of the SiO<sub>2</sub> Source Material***

Another potential cause of the index gradient was attributed to an oxygen depletion of the SiO<sub>2</sub> source material during deposition. It was hypothesised that a shift in the refractive index of the source material over the course of a deposition would cause a gradient in the index of refraction within the GLAD deposited films. To rule out this as a potential cause of the index gradient, SiO<sub>2</sub> was deposited at  $\alpha = 0^\circ$  onto a silicon substrate, where most of the substrate was covered by a deposition flux mask. In the experiment, some material was deposited onto part of the silicon substrate, and then the substrate was rotated to expose a new part of the substrate, in a similar fashion as was done previously for TiO<sub>2</sub> in §3.2. The resultant films would thus be representative of incremental strata in a thick solid SiO<sub>2</sub> film and would reveal changes in the source material over the course of a deposition. The indices of refraction of each of these films were then acquired using the spectroscopic ellipsometer using a Cauchy dispersion equation. As shown in Fig. 40, the refractive index of the films as a

function of the total thickness deposited shows little change in the index of refraction.

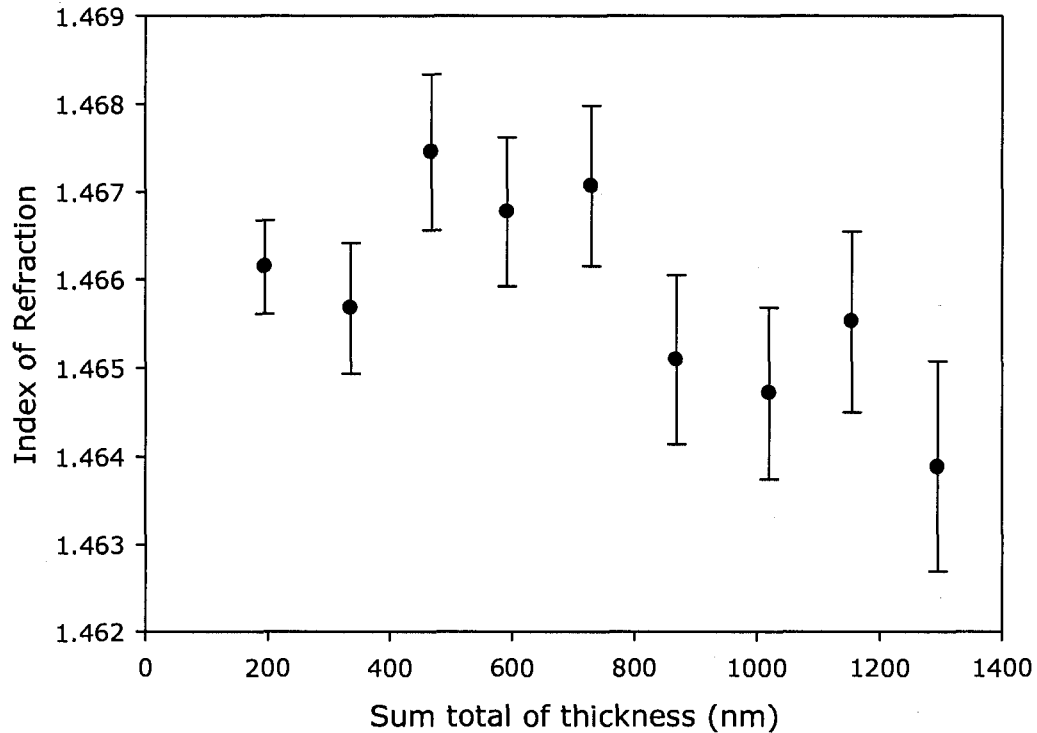
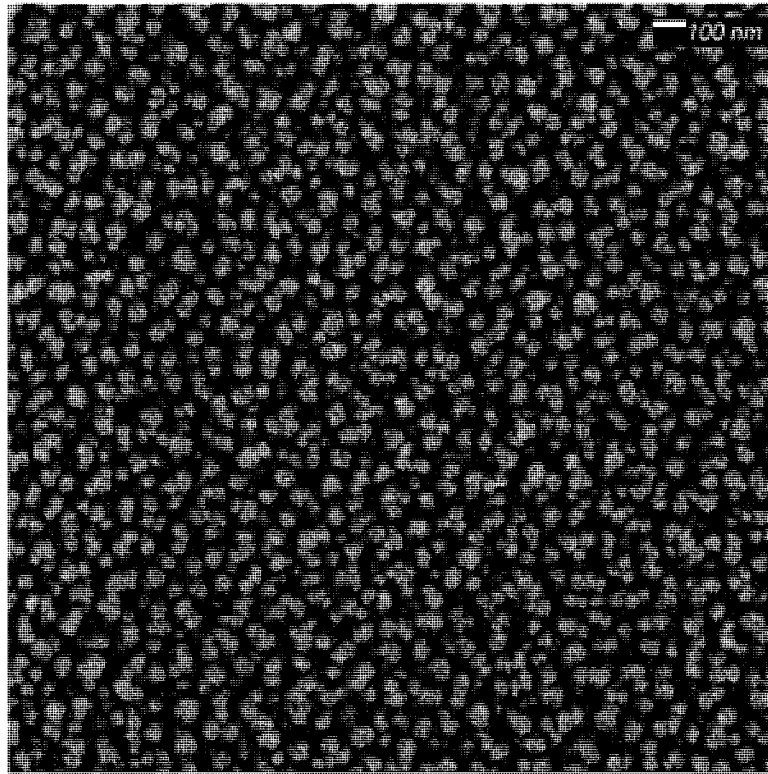


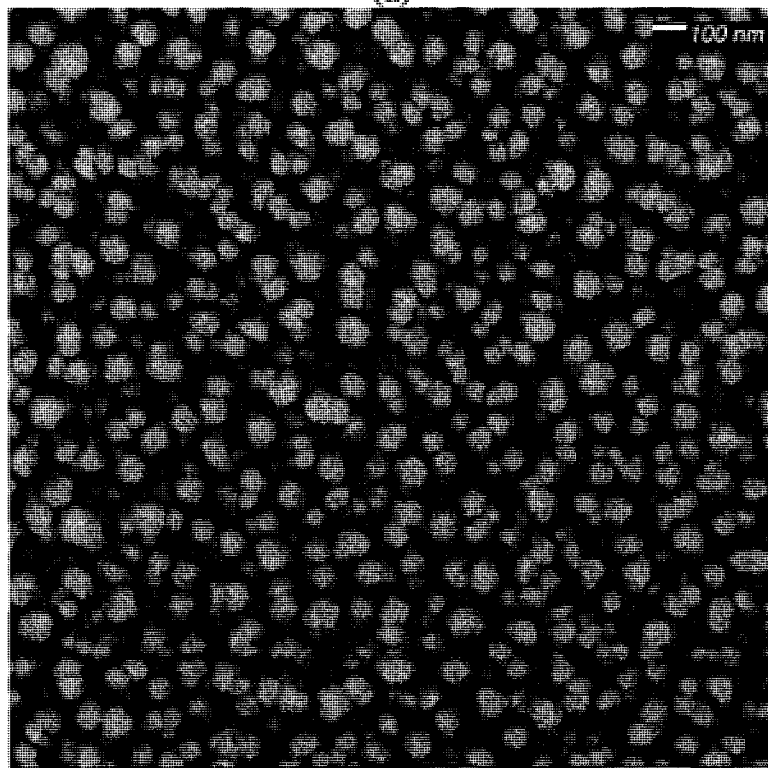
Figure 40 – Index of refraction versus cumulative thickness for normally grown SiO<sub>2</sub>.

### ***5.3 – Scanning Electron Micrograph Image Analysis***

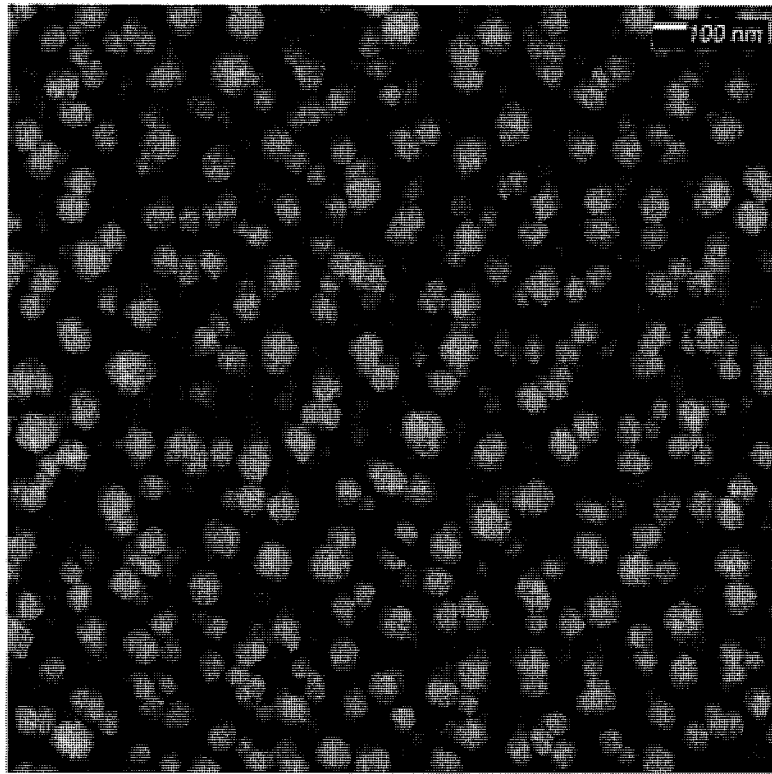
A series of the vertical post SiO<sub>2</sub> films (having thicknesses of 197 nm, 424 nm, 662 nm, 845 nm, 1032 nm, and 1236 nm) were analyzed using a Fast Fourier Transform (FFT) analysis of top-down SEM images, which can be seen in Fig. 41(a) –(f), respectively.



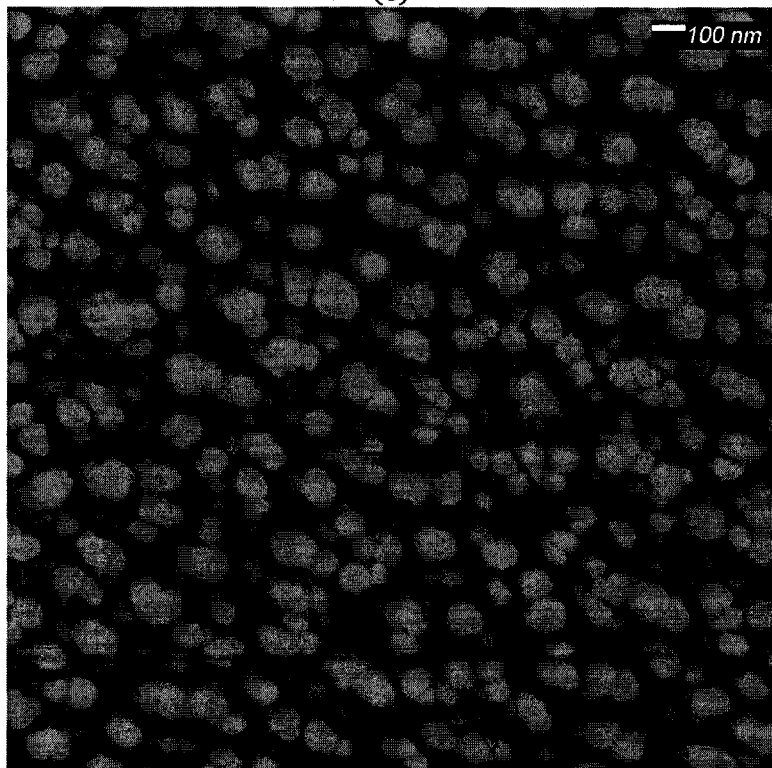
(a)



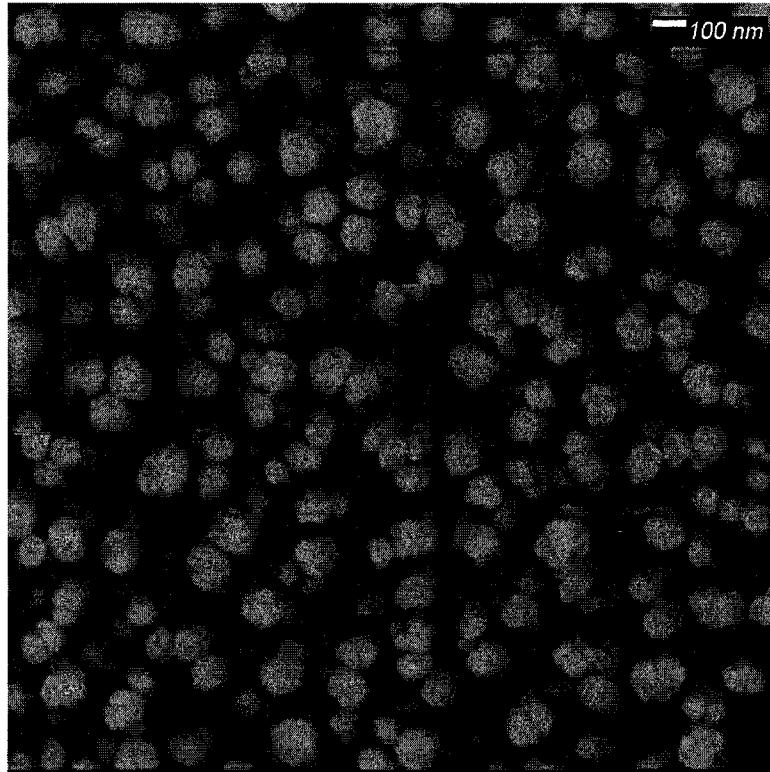
(b)



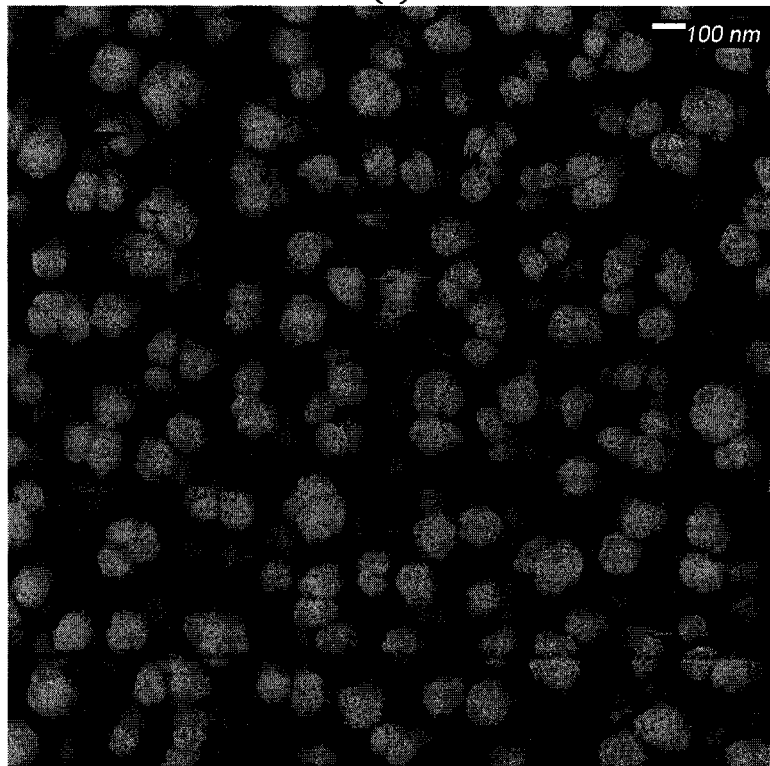
(c)



(d)



(e)



(f)

Figure 41 – Top-down SEM images of SiO<sub>2</sub> GLAD films composed of vertically aligned with a thickness of (a) 197 nm, (b) 424 nm, (c) 662 nm, (d) 845 nm, (e) 1032 nm, and (f) 1236 nm.

This technique allows for an estimation of the average column spacing in the films by computing the spatial frequency of the columns. One limitation of this technique is that when viewing the top-down SEM images, some of the shorter columns that appear in the images have already become extinct, and appear as darker columns within the images, while taller columns of the film that have not yet, or only recently, become extinct appear as brighter spots. To isolate the columns which have not yet become extinct, we first analyzed the pixel value histogram (Fig. 42).

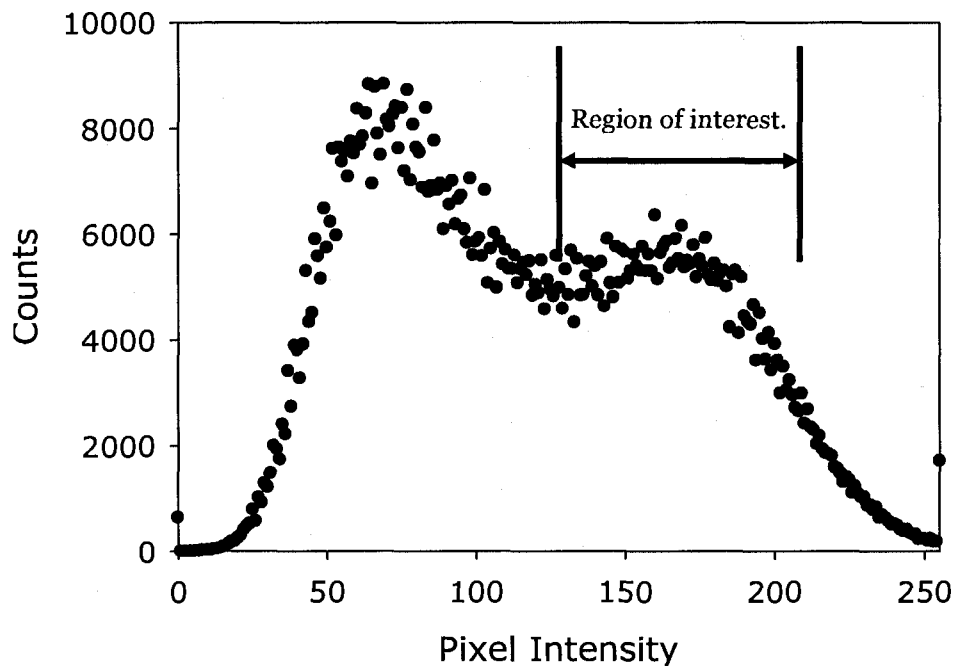
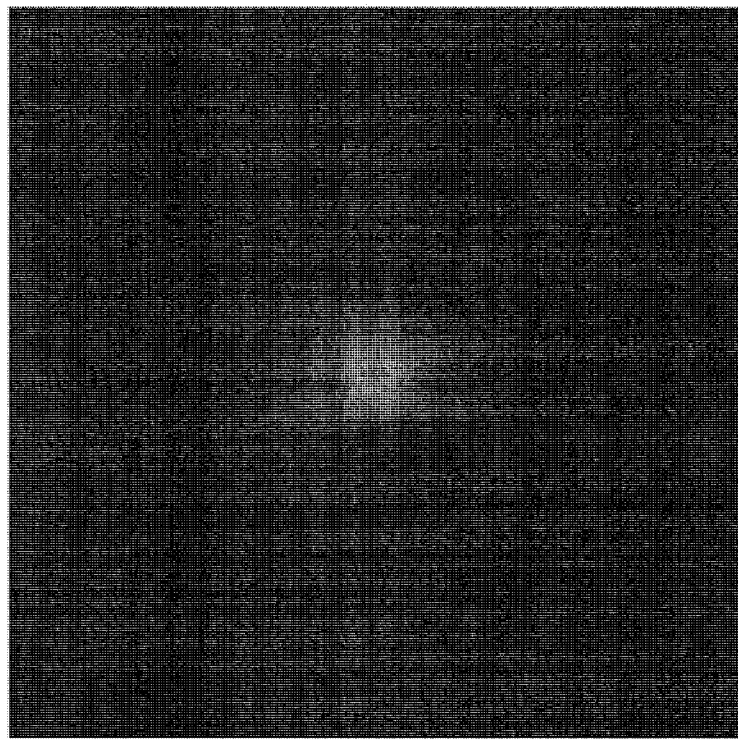


Figure 42 – Histogram of pixel intensity for a top down SEM image shown in the previous figure (Fig. 41a).

As can be seen, there are two maxima within the histogram, which is typical for these top-down SEM images, with the high-valued pixel intensity maxima corresponding to columns that are at the top of the film. After obtaining the

histogram, we then set bounds (illustrated as the region of interest in Fig. 42) on the image by setting all pixels outside of the bounds to a pixel value of 0, thus removing all spots except the columns that have not yet become extinct. An FFT was then applied to the resultant image, producing a 2D image with a doughnut like shape in the center of the image (Fig. 43a). Finally, a radial average of the FFT image yields the spatial frequency of the column separations, or by inverting this, the average column spacing (Fig. 43b).



(a)



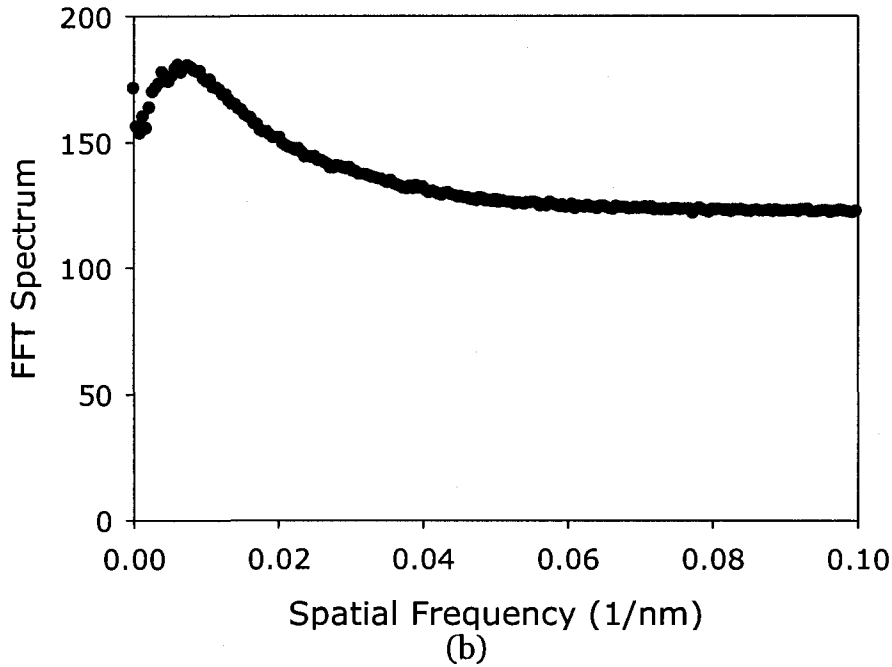


Figure 43 - (a) FFT of the top down image for the film in Fig. 41(a), and (b) the radial average of the FFT, with the spatial frequency calculated.

By analyzing the full series of the films, we obtained an average column spacing of 142 nm, 228 nm, 325 nm, 325 nm, 379 nm, and 455 nm for increasing film thickness for the films shown in Fig. 41. At first glance, this may suggest that the films are less dense at the upper strata of the film than at the lower strata. However this was contradicted by examining the optical model at the wavelengths of 1000 nm and longer, wherein film densities obtained using the Bruggeman EMA were 24.24%, 23.34%, 22.07%, 22.66%, 23.97%, and 21.38% for the thinnest to thickest films, respectively. This lack of significant density change for the increasing thickness suggests that the columns are broadening into the areas left by extinct columns. We can thus compute the average column diameters by multiplying the average column spacing by the film density to be 32

nm, 49 nm, 63 nm, 72 nm, 91 nm, and 97 nm for the films of increasing thickness.

#### **5.4 – Optical Modeling Using Finite Wavelength Effects**

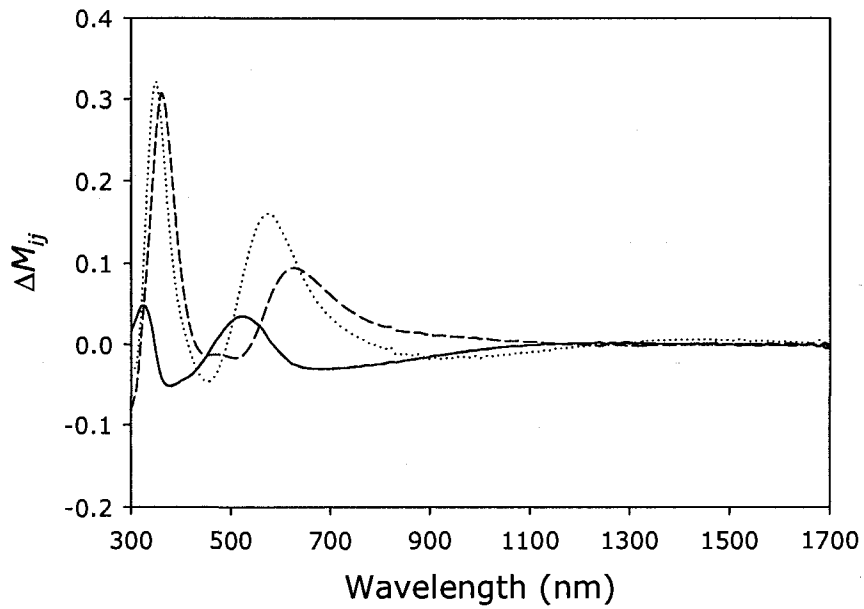
As was pointed out in regards to Fig. 37, the correspondence between experimental and model ellipsometry data was substantially worse at lower wavelengths than at higher wavelengths. This may have been caused by column broadening, which is suggested by the result in the case of the PhiSweep grown SiO<sub>2</sub> film. In the analysis presented here, we used the theoretical basis for generating Mueller matrices for multiple film layers, as was discussed in §1.5. To account for finite wavelength effects (*i.e.*, non-zero column sizes), we used theory presented by several authors based on a dynamic EMA, which attempts to account for effects of particle size on the effective medium. In general, a finite wavelength approximation to the effective medium,  $\epsilon_{FW}$ , can be written as [113, 114]:

$$\epsilon_{FW} = \epsilon_{BEMA} + \frac{\sum_i \frac{\pi^2 d_i^2}{30\lambda^2} f_i (\epsilon_i - \epsilon)}{\frac{3f_{air}\epsilon_{air}}{(\epsilon_{air} + 2\epsilon)^2} + \frac{3f_{material}\epsilon_{material}}{(\epsilon_{material} + 2\epsilon)^2}} \quad (5.4.1)$$

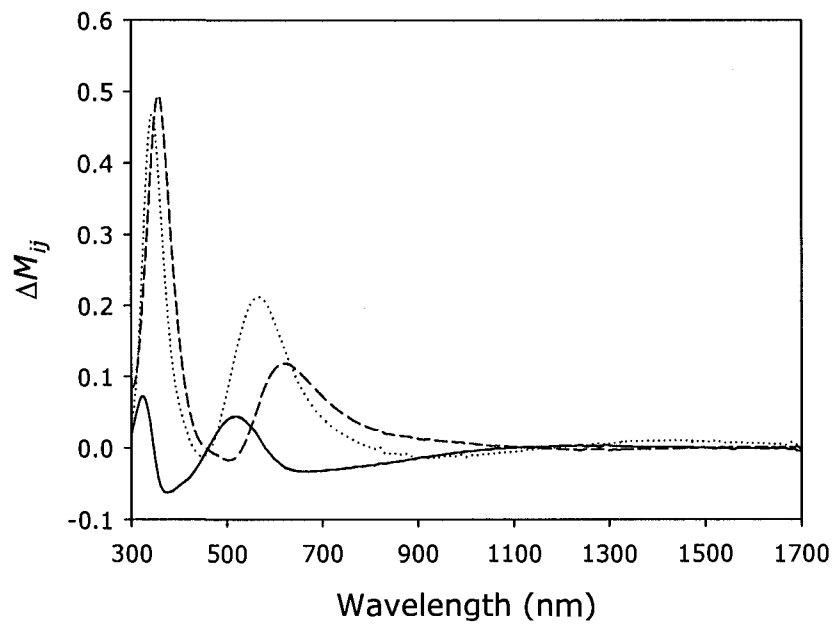
where  $\epsilon_{BEMA}$  is the effective medium found using BEMA, and  $f_i$  is the volume fraction of particles with a dielectric constant  $\epsilon_i$  and a diameter of  $d_i$ . This expression provided a perturbation in the effective dielectric constant on the order of a few percent.

We now assume that the density, film thickness, and depolarization parameters that were obtained using long wavelengths for the films in Fig. 41 are

true to the infinite wavelength assumption; we can then apply the particle size contributions to each successive film. That is, using the multiple layer analysis for generating Mueller matrices presented in §1.5, we can analyze each film in Fig. 41 as being composed of multiple layers with increasing particle sizes. An example of this is as follows: the film shown in Fig. 41c would be theoretically comprised of three layers. The bottom layer has the particle size characteristics and thickness of the film shown in Fig. 41a, the second layer has the particle size characteristics and thickness of the film shown in Fig. 41b minus the thickness of the film in Fig. 41a, and the third layer has the particle size characteristics of that shown in Fig. 41c with a thickness of the film shown in Fig. 41c minus the thickness of the film shown in Fig. 41b. This analysis is then used to generate the model Mueller matrices using a similar Maple code as seen in Appendix 1. The use of Maple here was necessary due to limitations in the inputs that could be provided into the VASE analysis software, though both the VASE software analysis and the theory presented here is based on that seen in §1.5. As can be seen in Fig. 44, by including the finite wavelength effects, the difference between the experimental and theoretical became worse than not including any finite wavelength effects at all. Furthermore, the expression shown in (5.4.1) suggests that the effective index of the film should increase with increasing thickness due to increasing particle size, whereas the observed index gradient decreased with film thickness.



(a)



(b)

Figure 44 – Comparison of the difference between experimental and theoretical Mueller matrix elements using the standard EMA (a), and a finite wavelength EMA (b) for the film shown in Fig. 41c.

Though this analysis has yielded important information about the growth of the film columns by using the Bruggeman EMA and using SEM image processing, it is clear that there are improvements required for a complete optical description of the GLAD film characteristics. Though this study focused on thicker films, another hypothesis could be made to account for the index gradient is that it appears due to the nucleation phase occurring in the first approximately 100 nm of film growth before the density reaches a stable value. Further studies on the index gradient may reveal important information about the growth mechanics of the nucleation process.

## **6 – Applications to Structured Media**

### ***6.1 – Periodically Arranged Columnar Thin Films<sup>8</sup>***

The study and development of photonic crystals continues to be an exciting area of research in the photonics industry. It is believed that photonic crystal devices may pave the way to optical computing, optical transistors, integrated circuit-like optical circuits, and perhaps new devices that have yet to be conceptualized. There have been many proposed architectures for photonic crystals, such as wood-pile structures [115, 116], inverse opal structures [117] and tetragonally arranged square spirals [118, 119].

In this section, a comparison of the optical properties for patterned amorphous silicon posts and unpatterned amorphous silicon posts grown using the GLAD technique is presented. This is done to acquire further information about the posts for use as square spiral photonic crystals, as well as to assess the feasibility of Mueller matrix ellipsometry as a characterization tool for evaluating the square spiral structure.

The fabrication of photonic crystals via GLAD requires three-dimensional periodicity in the thin film microstructure [6, 67, 120, 121]. Periodicity in the vertical thin film growth direction can be introduced through periodic rotations of the substrate in  $\varphi$ . However, nucleation in the early stages of thin film deposition occurs randomly, prohibiting periodicity in the substrate plane. To

---

<sup>8</sup> This section has been largely extracted from: J. Gospodyn, M. A. Summers, M. J. Brett, and J. C. Sit, "Mueller matrix ellipsometry of multilayer porous columnar thin films with applications to square spiral photonic crystals," presented at Photonics West, San Jose, CA, 2005.

bypass this hindrance, pre-patterned substrates consisting of a two-dimensional array of relief structures can be used to selectively shadow the substrate, resulting in preferential nucleation and growth at the seed sites.

The fabrication of three-dimensional photonic crystals via GLAD was initially demonstrated using a tetragonal lattice of substrate seeds patterned with photolithography [12]. However, periodic arrays of sub-micron features can be fabricated using a variety of techniques, including laser interferometric lithography [122], embossing techniques [120], electron beam lithography [121], and laser direct-write lithography[121]. Photolithography is highly reproducible and amenable to economical mass production. However, direct-write lithography techniques such as laser direct-write lithography and electron-beam lithography offer the significant advantage of easy parameter modification, since no master is required. EBL was chosen for this experiment on account of its superior resolution capabilities.

The experimental process began with pre-patterning 1.5 cm silicon dies with a periodic structure. Each die was cleaned in a piranha cleaning solution (1:3 H<sub>2</sub>O<sub>2</sub>:H<sub>2</sub>SO<sub>4</sub>) and spin coated with a 100nm ± 10nm layer of SU-8 2000.1 (MicroChem) epoxy novolak negative tone resist formulation. Pattern exposure was performed with a commercial EBL system (RAITH150, Raith GmbH). The resist was developed in SU-8 Developer solution (MicroChem).

Undoped silicon metal (99.999%, Cerac) was deposited onto the silicon dies using electron-beam evaporation with a vapor incidence of  $\alpha = 85^\circ$ . During each film growth, the evaporation chamber was first brought to a base pressure of approximately  $9 \times 10^{-5}$  Pa, and the deposition pressure did not exceed  $4 \times 10^{-4}$  Pa.

Directly preceding each structured thin film deposition, a seed enhancement layer was deposited to minimize the inter-seed growth. This was accomplished by depositing a thin silicon layer at the same incidence angle as the films of interest, while continuously turning the substrate rotational motor at a rate of approximately 60 RPM.

Thin films were deposited in slanted post configurations to a thickness of  $600 \text{ nm} \pm 50 \text{ nm}$ . Slanted post films were deposited both with and without utilizing the PhiSweep algorithm. For the non-PhiSweep films, the  $\phi$ -motor was held constant throughout the entire deposition. For the PhiSweep films, the rotational angle  $\phi$  was swept between angles of  $\phi = \pm 30^\circ$  from the central line defining the column growth.

The Mueller matrices and ellipsometry data for the films were measured using the VASE. This was done systematically for the series of films, beginning with the seed enhancement layer. First, the seeded area was examined with the ellipsometer, with the focusing probes equipped, so as to reduce the spot size of the light on the sample to approximately 0.5 mm wide, and some length depending on the angle of incidence of the incoming light. This was done to accommodate for the fact that the patterned area was 1 mm by 3 mm. Then, the unseeded area adjacent to the seeded area was examined, with the focusing probes still in place. The separation distance between the two areas examined was typically 0.8 mm. This level of positional accuracy was achieved using the sample translation stage equipped with the ellipsometer. This was considered to be a good configuration for measurement purposes, so that any variations in the film itself over varying positions in the plane of the substrate could be neglected



due to the close proximity of the two measurement spots on the substrate. Thus, any differences could be attributed to the difference between seeded versus unseeded film material. Next, films with a layer of slanted posts, or the first quarter-turn of a square spiral, grown on top of the seed enhancement layer were evaluated by the same procedure. Mueller matrix and spectroscopic ellipsometry of both the patterned and unpatterned areas was performed in reflection mode with a wavelength range of 1000 nm to 1700 nm, and angles of incidences of  $55^\circ$  to  $75^\circ$  with respect to substrate normal. The Mueller matrix data for the slanted post layers for the  $1/4$ -turn films were then modeled by either a uniaxial or biaxial material (which depends on whether or not the layer is a vertical or slanted post, respectively) with dispersion relations along the principal indices of refraction defined by Cauchy dispersion in the index of refraction and by Urbach absorption in the extinction coefficient [38].

The seed enhancement layer was first deposited onto the samples with the pre-patterned area using silicon. The seed enhancement layer is deposited in an effort to increase the effective diameter of the seeds produced by electron beam lithography in the plane of the substrate. This layer was grown as vertical posts using a rapid rotation about  $\phi$  to nominal thicknesses of about 150 nm. The SEM image for the resultant film for the patterned area is shown in Fig. 45. As is evident due to the structural shape of the film, the optical properties of the film in both the patterned and unpatterned case can be described as a uniaxial material, with the extraordinary optical axis lying along the substrate normal, and the ordinary optical axis lying in the plane of the substrate, which has been discussed by other authors [46, 47, 123]. Thus, the seed enhancement layer can be modeled

using the WVASE32 software as a uniaxial material. In the infrared region from 1000 nm to 1700 nm, both of the principal indices can be modeled using Cauchy dispersion with an Urbach absorption tail at the lower wavelength region. This is a common dispersion relation for dielectric materials [38], and is used because in this wavelength regime, silicon is a transparent medium.

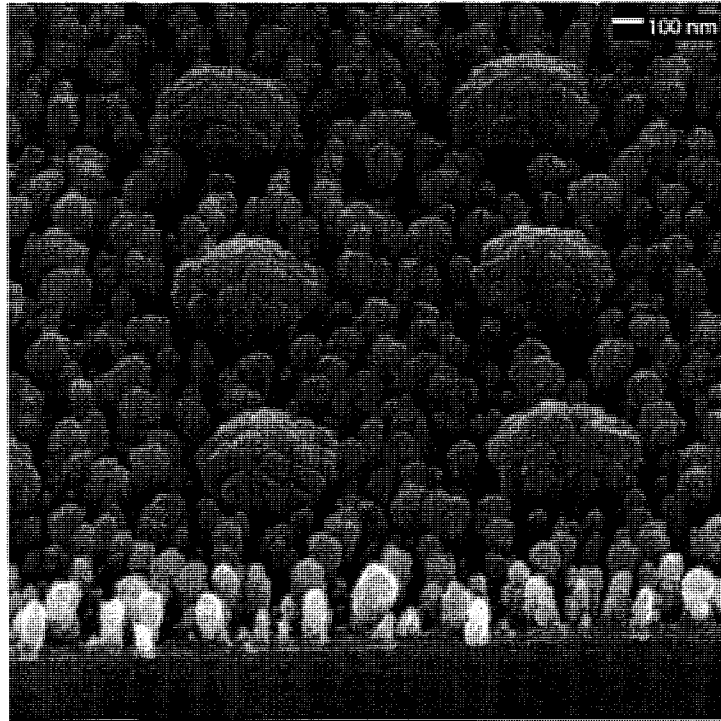


Figure 45 – SEM image of the seed enhancement layer.

An example of the optical model for the seed enhancement layer is shown in Fig. 46. Note that in the model, as will also occur in layer models described later, the layers denoted by “cauchy” and “cauchy2” have thicknesses which are fixed to 0 nm, thus are set as “dummy” layers in the model template so that the optical properties of the film can be determined, where the “cauchy” is the medium defined in the “biaxial” layer as the extraordinary optical axis, and the “cauchy2” is the medium defined in the “biaxial” layer as the ordinary optical axis.

3	biaxial	245.31 nm
2	cauchy2	0 nm
1	cauchy	0 nm
0	Si_substrate	0.25 mm

Figure 46 – An example of the layer modeling of the seed enhancement layer.

An example of the experimental and generated Mueller matrix data is shown in Fig. 47 for comparison. The resultant thicknesses for the seed enhancement layers were 245 nm and 230 nm for the patterned and unpatterned areas, respectively. The extra thickness in the patterned region was attributed to the presence of the SU8 seeds. The index of refraction for the patterned or unpatterned regions is shown in Fig. 48 (a) and (b), respectively. It appears that the indices are slightly higher in the patterned areas as compared with the indices in the unpatterned areas.

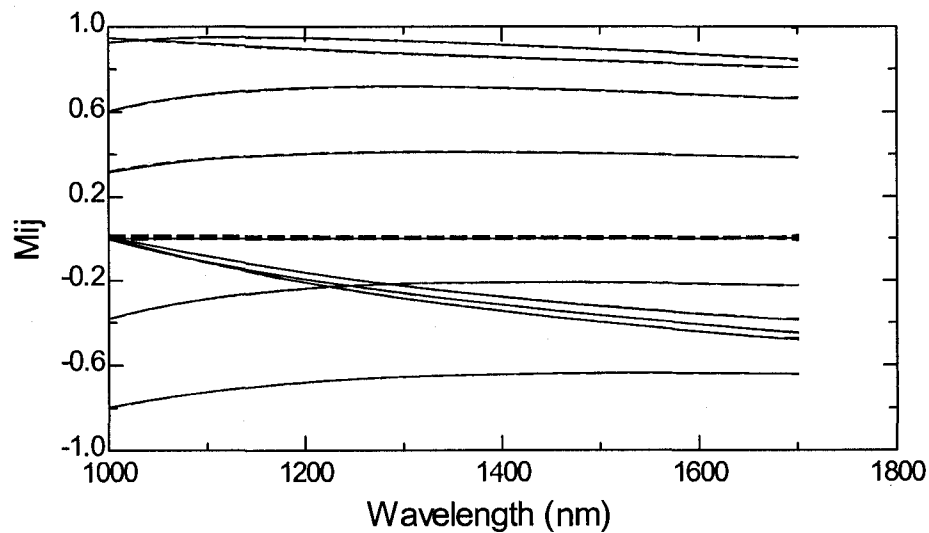
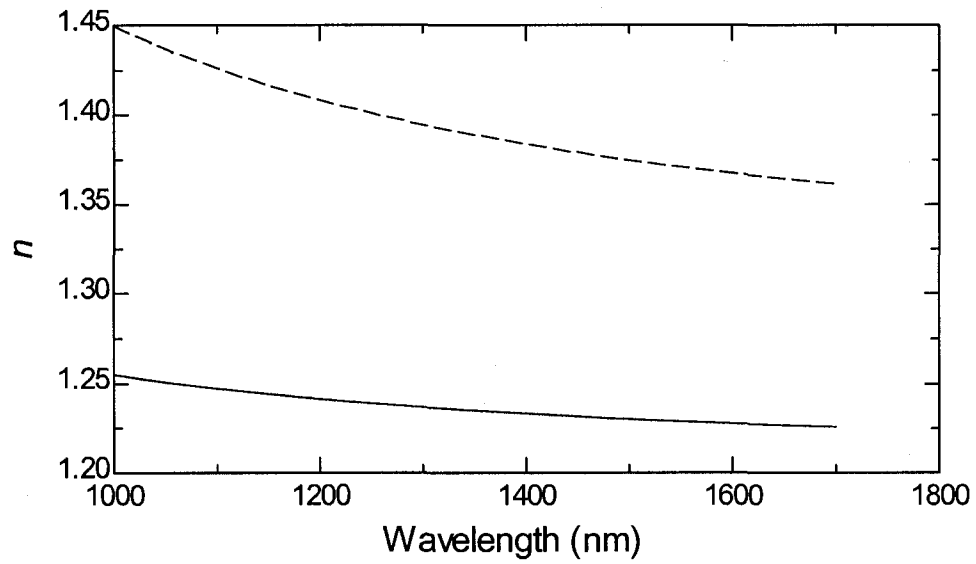
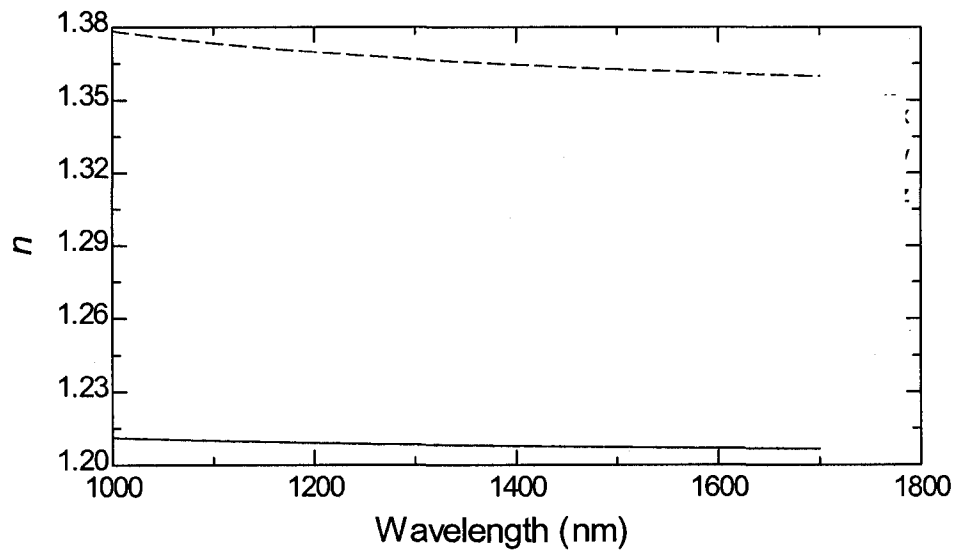


Figure 47– An example of the experimental (dashed) and theoretical (solid) Mueller matrix elements. This example is for the unpatterned region. The matrix element labels are left off for the sake of clarity.



(a)

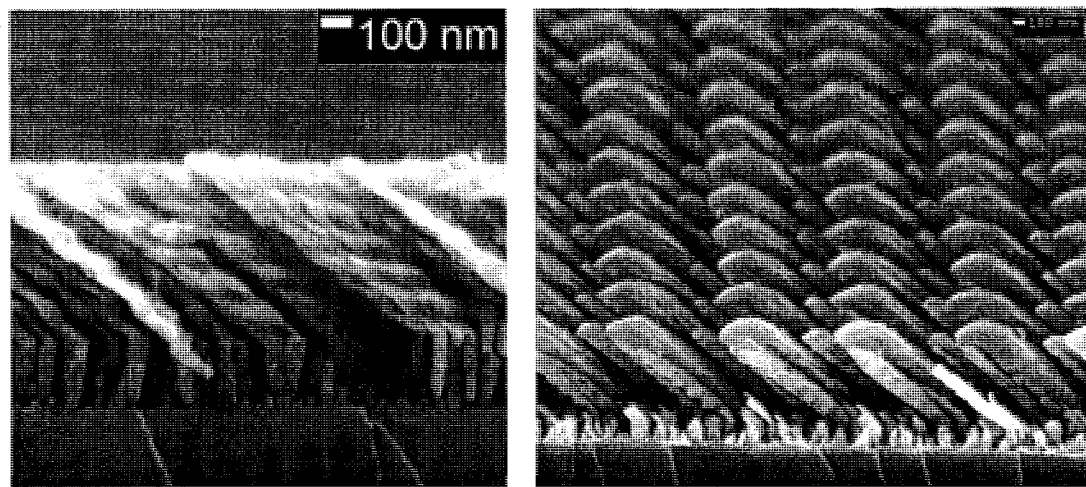


(b)

Figure 48 – The indices of refraction  $n_e$  (dashed) and  $n_o$  (solid) for the seed enhancement layer for (a) the patterned section and (b) the unpatterned section.

With the seed enhancement layer (seen in Fig. 49 as the columns adjacent the substrate which are aligned along substrate normal) deposited and characterized, a slanted post layer, or quarter-turn of a square spiral, could then be deposited on

top of the seed enhancement layer. The SEM images for the resultant films for both the unpatterned and patterned areas for the PhiSweep GLAD deposition techniques are shown in Fig. 49. There are several things to note about the PhiSweep deposited film, compared with that of traditional GLAD. First, in the unpatterned areas, the PhiSweep film looks dense, although it is the same density of that of the traditional GLAD, which has been determined by comparing the thickness of PhiSweep GLAD films and traditional GLAD films and finding that they are approximately equal. More importantly, by comparing the top-down images of the patterned area, it can be seen that for the PhiSweep GLAD, the pillars are shaped more like ideal cylinders, while for the traditional GLAD, the pillars are almost crescent shaped, with the bend pointing toward the direction of incoming flux. These analyses, as well as the possible growth mechanisms, have been described elsewhere [11, 121].



(a)

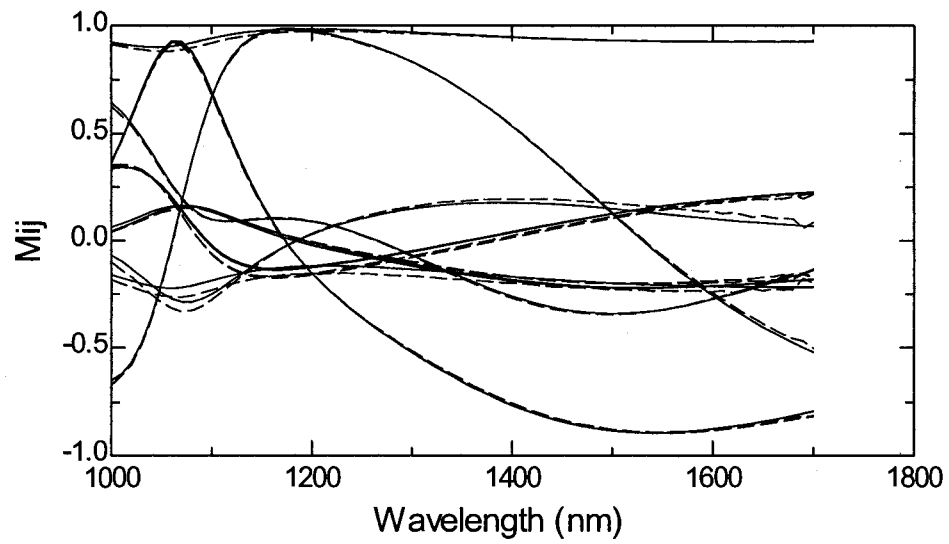
(b)

Figure 49 – SEM images of the unpatterned (a) and patterned (b) areas of the first quarter turn of a square spiral using the PhiSweep method. Note that the small chevron-like features are a result of the PhiSweep method.

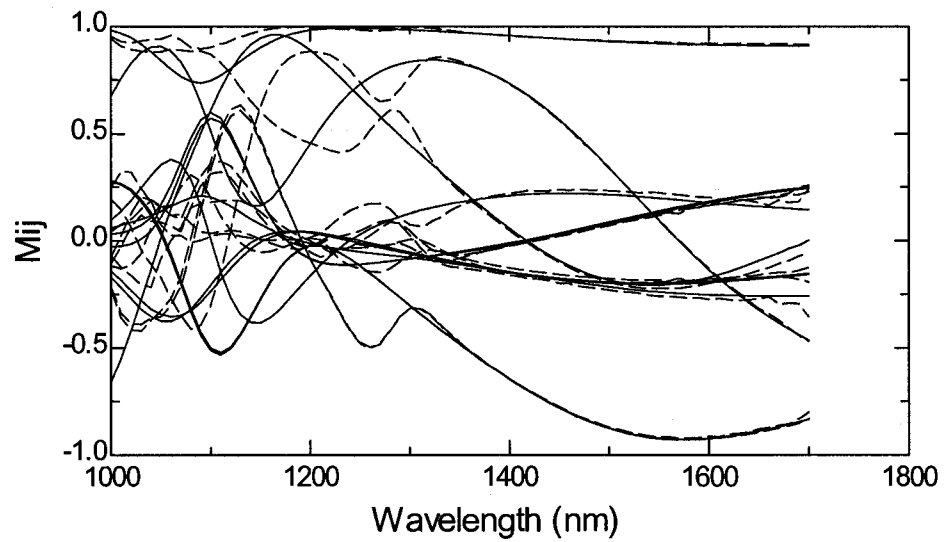
An example of the optical model is shown in Fig. 50. In these cases, the “cauchy” layers for the seed enhancement layer have simply been renamed to their respective “normal” and “in-plane” descriptions. To evaluate the optical properties of the slanted post layers, we have now defined the slanted post layer as a biaxial medium. As can be seen from the geometry of the slanted posts, one of the principal indices,  $n_z$ , lies along the direction of the posts, the second,  $n_y$ , being perpendicular to the deposition plane, and the third,  $n_x$ , in the deposition plane perpendicular to the columns [46, 47, 123]. The tilt angle of the posts with respect to substrate normal,  $\theta$ , was also required to be a fit parameter in the model in order to determine the values of the principal indices. The generated and experimental Mueller matrix data for both the patterned and unpatterned areas are also shown in Fig. 51(a) and (b) grown with the traditional GLAD deposition method. The index of refraction for both the patterned and unpatterned areas are shown in Fig. 52, and the angles  $\theta$  for the data sets were found to be in the range of  $54^\circ$  to  $58^\circ$  with respect to substrate normal, according to the best model fit. These angles are comparable to the angles found in the SEM images.

7 biaxial2	644.88 nm
6 cauchy3	0 nm
5 cauchy2	0 nm
4 cauchy	0 nm
3 biaxial	230.5 nm
2 inplane	0 nm
1 normal	0 nm
0 Si_substrate	0.25 mm

Figure 50 – Example of the layer modeling for the seed enhancement layer plus a  $\frac{1}{4}$ -turn square spiral.

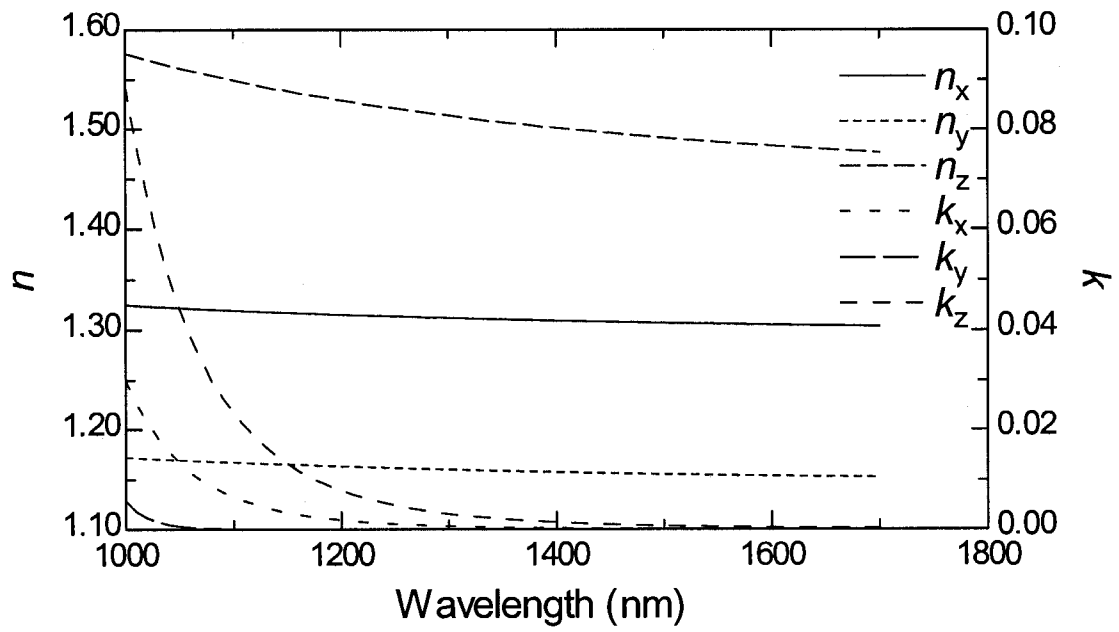


(a)

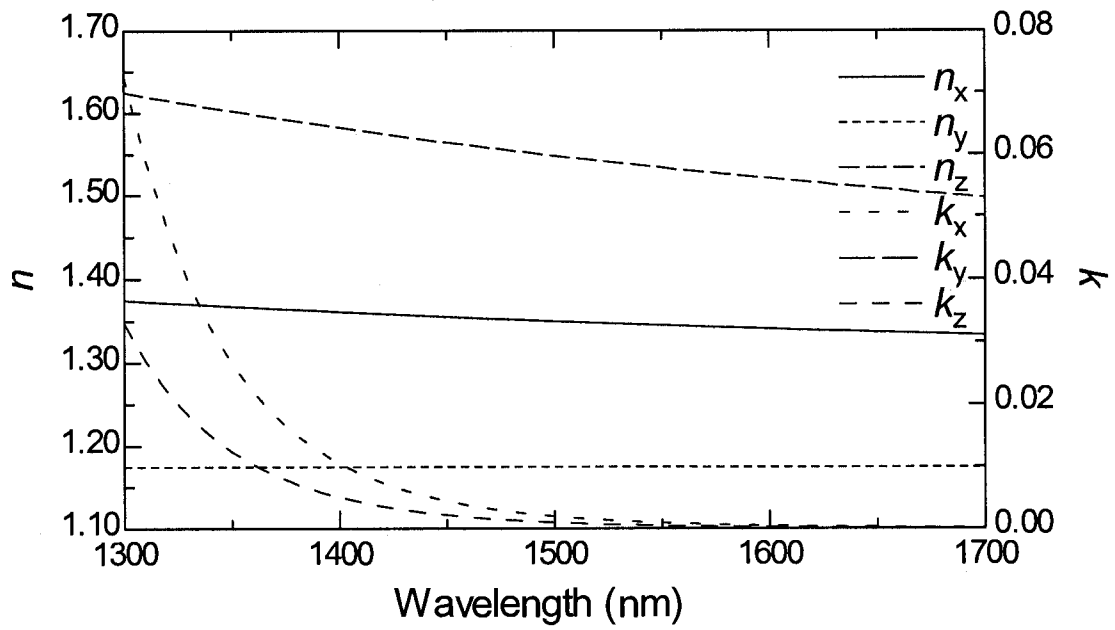


(b)

Figure 51 – Example of the experimental (dashed) and theoretical (solid) Mueller matrix elements at a  $75^\circ$  angle of incidence for the (a) unpatterned and (b) patterned regions of the PhiSweep grown film. The matrix element labels are left off for the sake of clarity.



(a)



(b)



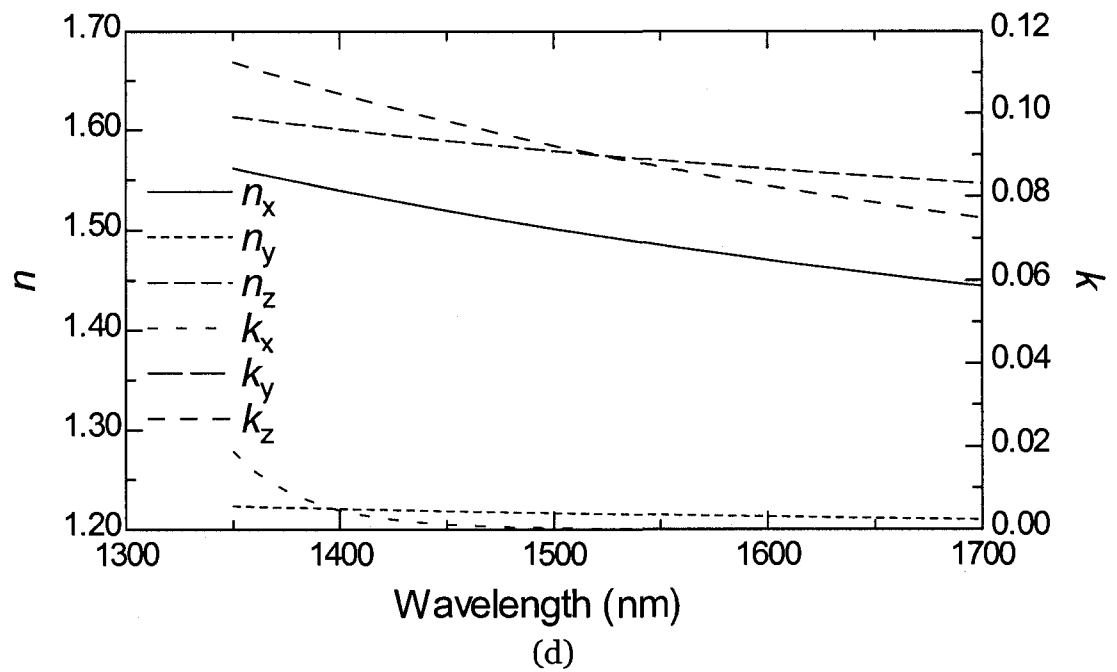
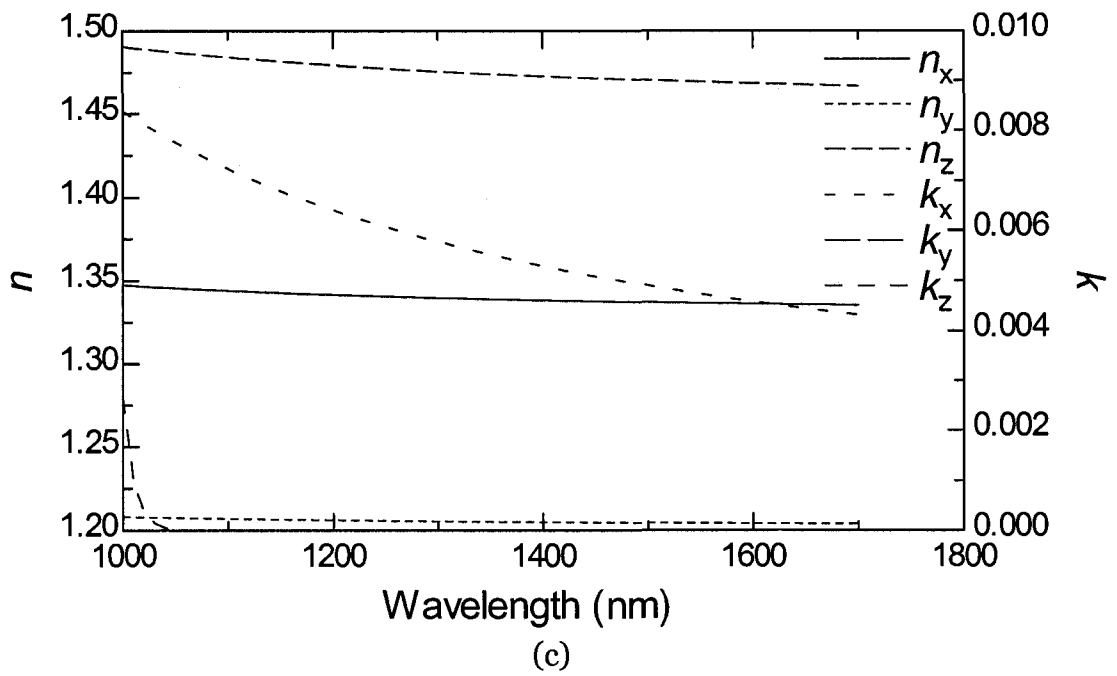


Figure 52 – Optical constants for the unpatterned (a) and patterned (b) sections of the traditional GLAD film and for the unpatterned (c) and patterned (d) regions of the PhiSweep GLAD film.

It has been shown in previous sections that for various other materials [46, 47, 123] that  $n_z > n_x > n_y$  and has been found to also be true here. Again, it

appears that the indices in the patterned areas are slightly higher than those in the unpatterned regions. This trend has been attributed to a few different possible causes. The first possibility is the posts are more dense and robust due to lower bifurcation of the posts. The other possibility is that due to the larger size of the posts in the patterned region, the surface area would be smaller, thus the presence of oxide in the sample would therefore be lower overall.

The Mueller matrix data for the unpatterned area fit well with the model over the entire spectrum, while the generated Mueller matrix data for the model diverged from the experimental data below approximately 1350 nm. This behavior has been attributed to the size scale of the periodicity of the posts themselves, which likely behaves similarly to a diffraction grating.

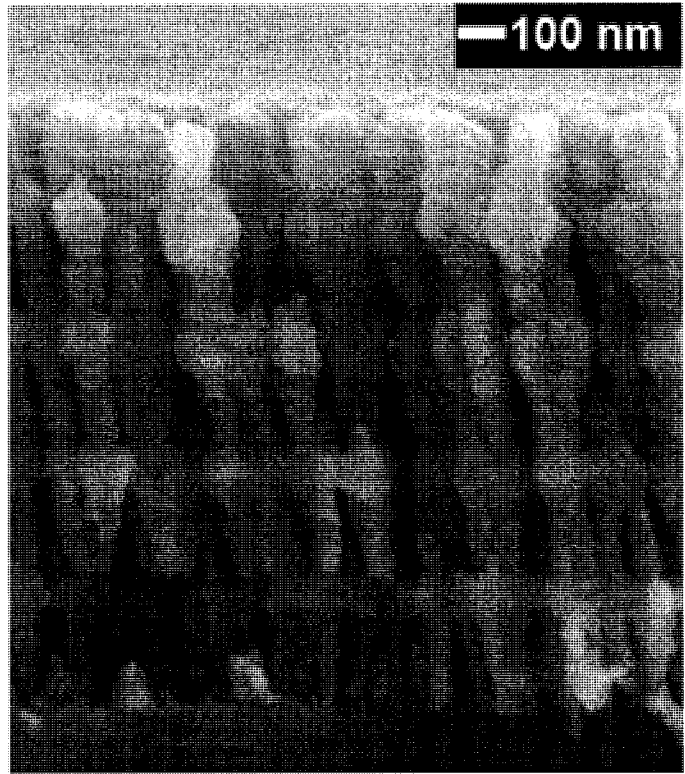
## **6.2 – Periodically Layered Luminescent Media<sup>9</sup>**

Films composed of  $\text{Y}_2\text{O}_3:\text{Eu}$  (source material: 6.5% wt doping concentration, Phosphor Type 2342, OSRAM Sylvania Inc.) were grown by GLAD using electron beam evaporation onto silicon and fused silica substrates. The deposition pressures were maintained from  $3 \times 10^{-4}$  Pa to  $5 \times 10^{-4}$  Pa by control of the electron beam current and addition of  $\text{O}_2$  gas as necessary. The first layer of the film was formed of  $\text{Y}_2\text{O}_3:\text{Eu}$  vertical columns deposited with a constant  $\alpha = 85^\circ$  and continuous, rapid rotation in  $\phi$ . After the desired film thickness was achieved,  $\alpha$  was decreased exponentially as a function of thickness added [69]

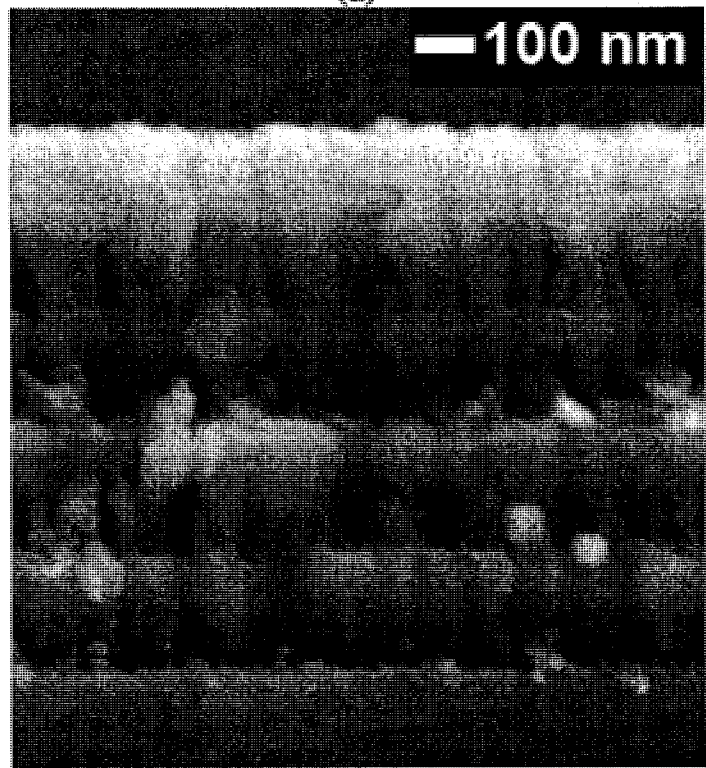
---

<sup>9</sup> This section has been largely extracted from: J. Gospodyn, M. T. Taschuk, P. C. P. Hrudey, Y. Y. Tsui, R. Fedosejevs, M. J. Brett, and J. C. Sit, "Emission profiles of  $\text{Y}_2\text{O}_3:\text{Eu}$  films composed of high-low density stacks produced by glancing angle deposition", *submitted to Appl. Optics*, 2007.

causing a gradual increase in film density. The deposition angle was then held at  $\alpha = 30^\circ$  for several nanometers of film growth. This procedure resulted in a low density layer with a high density cap. After a cap layer of the desired thickness was grown, the deposition angle  $\alpha$  was rapidly switched back to  $85^\circ$ . This process generated a unit layer with a large region of low density and a capping layer of high density  $\text{Y}_2\text{O}_3:\text{Eu}$ , and was repeated to produce four unit layers. This profile was chosen to produce a high-low dielectric stack of an index profile similar to previous studies on ITO [124]. A final low-density surface layer was added to reduce the interface refractive index. The physical periodicities were varied for different sets of films, herein referred to as sample sets A and B. A summary of the physical and optical parameters from the film sets is given in Table 4, with the resonance wavelengths being averaged for all annealing conditions. An example of each film set can be seen in the scanning electron micrographs in Fig. 53 (a) and (b). The Bragg resonances of the films were designed such that in the case of films in set A, the PL emission at normal incidence would occur between the primary and second harmonic Bragg resonances for the as-deposited films, and in set B the primary Bragg resonance would occur at the PL emission wavelength for the as-deposited films.



(a)



(b)

Figure 53 – Cross sectional SEM image of a film from set A (a) and set B (b).

Film Set	Physical Periodicity as-deposited	2nd harmonic Bragg resonance		Primary Bragg resonance	
		as-deposited	annealed	as-deposited	annealed
A	261 nm	414 nm	349 nm	822 nm	673 nm
B	199 nm	321 nm	278 nm	653 nm	543 nm

Table 4 – Summary of the physical and optical parameters for the films.

To activate intense PL emission intensities [20, 21, 125], a sample in each set was annealed at a temperature of 600°C, 700°C, 750°C, 800°C, 850°C, 900°C, or 1000°C in atmospheric air. The temperature was increased from room temperature to the annealing temperature at a rate of 5°C/min, held at the annealing temperature for one hour, and then allowed to cool passively.

The films were optically characterized by spectroscopic Mueller matrix ellipsometry using the VASE in the wavelength range from 300 nm to 1700 nm. The films grown on silicon substrates were measured in reflection mode at angles between 50° and 70°, while the films grown on fused silica substrates were measured in normal incidence transmission mode. The resultant data were then analyzed and modeled.

The experimental setup used to characterize the angular distribution of the PL was similar to that used in previous studies [126]. Briefly, a frequency-quadrupled Nd:YAG (Big Sky Ultra CFR) generates ~ 7 ns pulses at 266 nm with ~ 130 μJ delivered to the sample film. The resulting photoluminescence was measured using a 0.25 m, f/3.9 spectrometer (Oriel MS260i) which had been calibrated for absolute intensity measurements. The emission from the films was measured at angles from normal to the substrate to an angle parallel to the

substrate in  $10^\circ$  steps, with the angle of the irradiation beam changing correspondingly as the sample was turned. The specular reflection of the laser light from the films was monitored with a calibrated photodiode, allowing a precise estimate of the total amount of energy coupled into the film. Combined with the angularly resolved emission measurements, this allowed for an estimate of the total photoluminescent conversion efficiency.

An example PL emission spectra for  $Y_2O_3:Eu$  observed in these films is shown in Fig. 54 with an emission line at 611 nm, which is characteristic of this material [127]. The emission intensity at several emission angles was measured for films annealed at  $800^\circ C$  on both silicon and fused silica substrates. As shown in Fig. 55, the angular emission profile of these films did not follow a Lambertian emission pattern, contrary to previous studies on  $Y_2O_3:Eu$  GLAD films [20, 21]. There was an observed maximum in emission at an angle of approximately  $60^\circ$  for films from both sets. It is expected that the emission in the normal direction was suppressed due to the primary Bragg resonance transmission minimum near 600 nm. At higher emission angles the transmission minima should shift to lower wavelengths, reducing the effect of the transmission minima on the  $Y_2O_3:Eu$  PL.

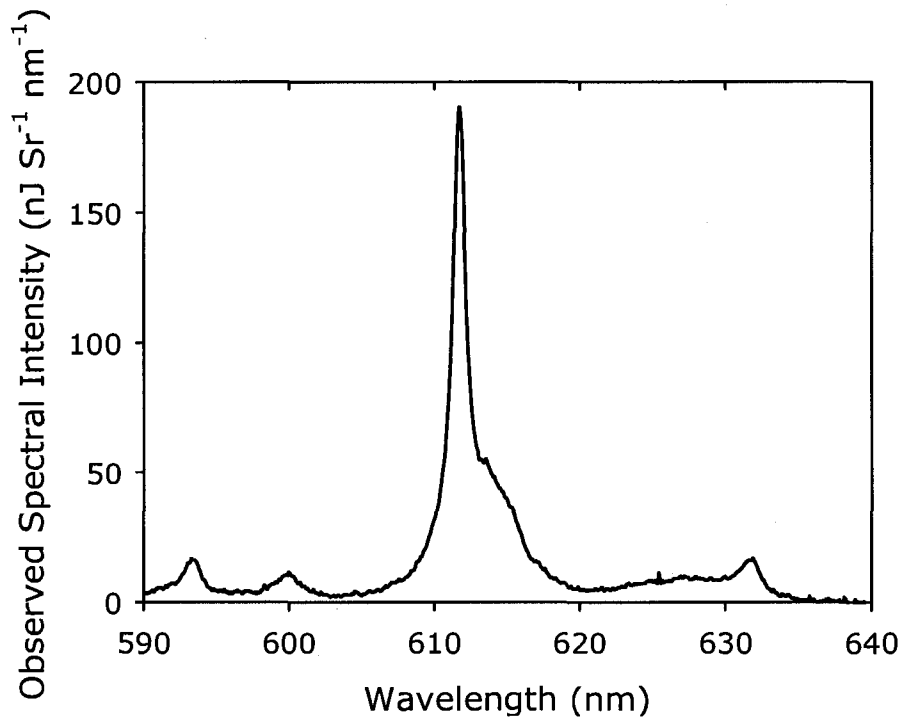


Figure 54 – Example of the PL emission spectra, taken from film set A annealed at 800°C.

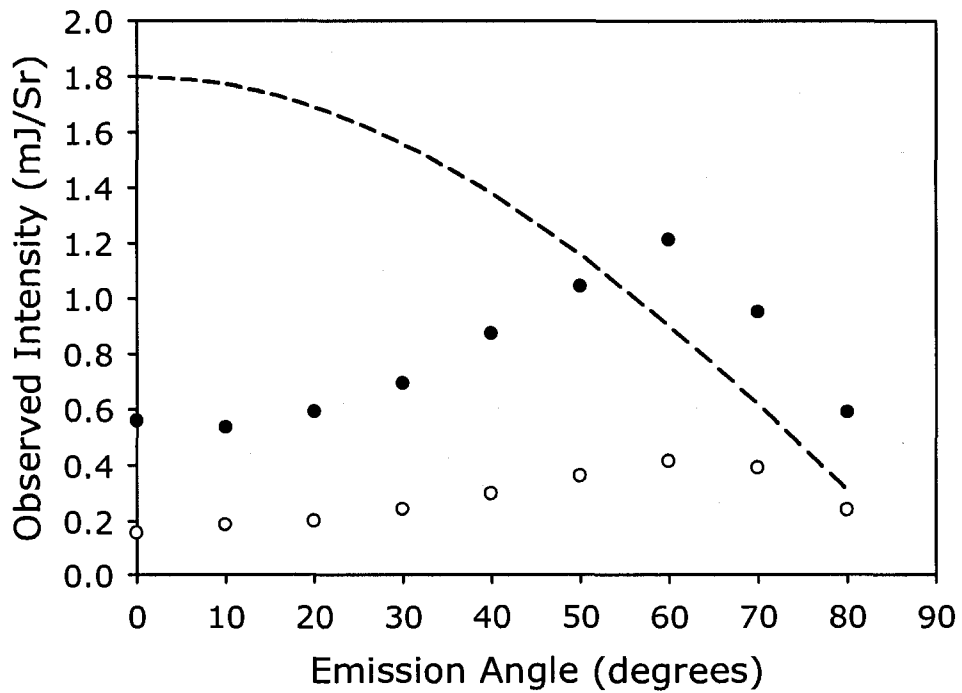
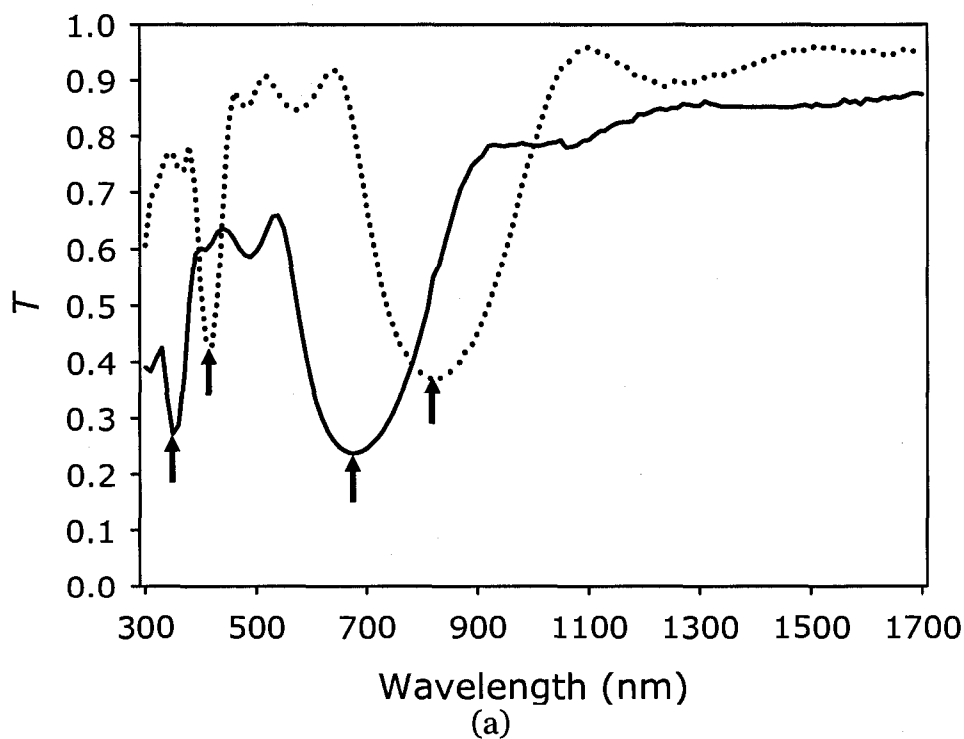


Figure 55 – Angular emission profile of film set A (●) and film set B (○) annealed at 800°C on fused silica substrates. The dashed line is an example of a Lambertian emission profile given in arbitrary units.

The transmittance of the films was measured using the ellipsometer and is shown in Fig. 56. Two principle minima in the transmission spectra were observed. The lower wavelength minimum was consistent with the first harmonic Bragg resonance expected from the periodic structure of the film, while the higher wavelength minimum was consistent with the second harmonic of the Bragg wavelength. It was found that the ratio of the high wavelength minima to the low wavelength minima ranged from 1.93 to 2.03 (this ratio being consistent with the two harmonics if one accounts for optical constant dispersion) for all of the available measurements for films from set A and B, and it was found that the Bragg resonances appeared within a few percent of the design wavelength. Annealing was found to cause a blue shift in the locations of the transmission minima for all samples. Similarly, blue-shifts due to annealing of Bragg phenomena have been observed for other materials [128]. Since it was found that the final spectral locations of the transmission minima for all annealing conditions were within 9 nm of each other for any given film set, we then used films annealed at 800°C for PL analysis, while simultaneously performing ellipsometry analysis on films annealed at 600°C. For samples annealed at 600°C, in film set A, the high  $\lambda$  blue shift was 149 nm (18.1%) while the low  $\lambda$  blue shift was 65 nm (15.7%), seen in Fig. 56(a). For film set B the high  $\lambda$  blue shift was 110 nm (16.8%), while the low  $\lambda$  blue shift was 43 nm (13.4%), seen in Fig. 56(b). These blue-shifts were consistent with an observed film thickness decrease of 9% to 10% from the SEM images, and an approximate 2% reduction in the effective index of refraction of the film due to annealing, as was obtained



from the ellipsometry models. Also note that the primary Bragg resonance in film set A was found to be near the emission wavelength, and that for film set B the second harmonic Bragg resonance occurs at 278 nm, which is quite close to the laser excitation wavelength. Since the laser was incident at off-normal angles, we expect that the second harmonic resonance would coincide with the laser wavelength for film set B due to the blue shift in the transmission spectra at off-normal angles, causing a high reflectance at the laser wavelength. This was confirmed by monitoring the reflected laser energy during PL excitation, and is consistent with the lowered emission intensity of films from this set. It was found that the final spectral locations of the transmission minima for all annealing conditions were within 9 nm of each other for any given film set.



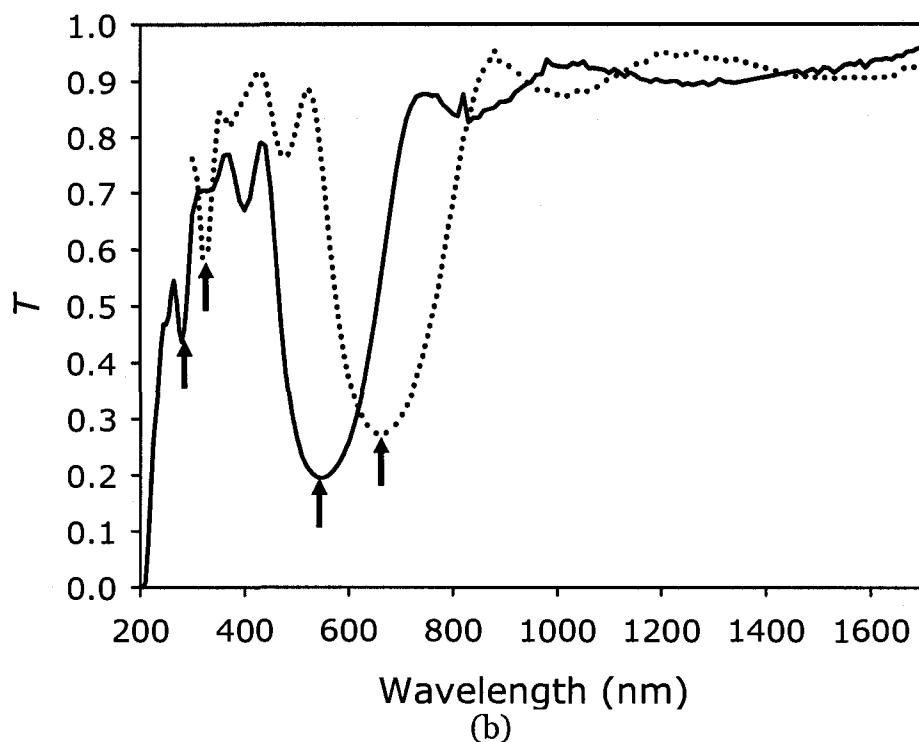


Figure 56 – Transmittance of film (a) set A and (b) set B on fused silica substrates as-deposited (dashed) and annealed at 600°C for 1 hour (solid). The arrows indicate the transmission minima. The data for the wavelength range from 200 nm to 300 nm was measured using a spectrophotometer (Lambda 900 Spectrophotometer, Perkin-Elmer Inc.)

An estimate of the film reflectivity at the laser wavelength was made by measuring the specularly reflected laser energy at  $\sim 15^\circ$  with respect to substrate normal, and was found to be 8% and 72% for films from set A and B, respectively. As was seen by the blue shift in Bragg resonances from post deposition annealing, it was expected that the reflectivity at the laser wavelength of 266 nm for films from set B was quite high compared to films from the other set, as suggested by the transmission spectra for the films before and after the annealing process, as in Fig. 56. The estimated reflectivity in turn allows for an estimate of the total absorbed energy for each set of measurements. To calculate the conversion efficiency, the total emission was numerically integrated for all angles. For the

films grown on fused silica substrates, the conversion efficiencies were in the range of  $2.6 \times 10^{-4}$  to  $4.3 \times 10^{-4}$ , which is approximately 50% smaller than the conversion efficiencies of vertical column  $Y_2O_3:Eu$  films, and approximately the same as solid  $Y_2O_3:Eu$  grown using our methods [126].

The Mueller matrix of the films was characterized using ellipsometry. The normalized Mueller matrices of the films were measured in reflection mode at angles of incidence between  $50^\circ$  and  $70^\circ$  with respect to substrate normal. The data was then modeled using nine film layers in the modeling software, with each layer corresponding to a layer of the films. The layers were described as uniaxial BEMA of void and film material [23, 50], where the optical constants of  $Y_2O_3:Eu$  were found by characterizing a solid  $Y_2O_3:Eu$  film grown at  $\alpha = 0^\circ$  which resulted in optical constants at a wavelength of 610 nm of  $n = 1.7404$  and  $k = 0.0021$ . An example of the model template with the best fit results for the density and thickness of the layers is shown in Fig. 57. The densities obtained were consistent with previous studies of other inorganic materials [16, 64], and has been shown in previous chapters.

9 BEMA Void/32.7% $Y_2O_3:Eu$	207 nm
8 BEMA Void/89.4% $Y_2O_3:Eu$	57 nm
7 BEMA Void/36.7% $Y_2O_3:Eu$	233 nm
6 BEMA Void/89.4% $Y_2O_3:Eu$	83 nm
5 BEMA Void/36.7% $Y_2O_3:Eu$	219 nm
4 BEMA Void/89.4% $Y_2O_3:Eu$	104 nm
3 BEMA Void/36.7% $Y_2O_3:Eu$	177 nm
2 BEMA Void/89.4% $Y_2O_3:Eu$	102 nm
1 BEMA Void/36.7% $Y_2O_3:Eu$	210 nm
0 Si Substrate or Fused Silica Substrate	0.25 mm or 0.8 mm

Figure 57– Optical model layers to describe a film from set A as-deposited.

The normalized Mueller matrix and the transmittance data were fit simultaneously in the modeling software. The thicknesses and the film densities of all of the layers were defined as fit parameters in the model. Since the densities of the layers grown at  $\alpha = 85^\circ$  (odd-numbered film layers) were expected to be equivalent, the density values were constrained to be equal and a similar approach was used for the capping layers (even-numbered film layers). The only exception to this was that the density of the topmost layer was fit independently from the others as its density appeared to be different from all the other layers as seen in the SEM images. The resulting fit for the case of non-annealed film from set A has a mean squared error of 23.6, and is shown in Fig. 58. Most of the discrepancy arose at lower wavelengths, which was due to an increase in scattering in the films at such wavelengths. Inconsistencies in the layer thicknesses that are found between the model and SEM images are attributed to the simplification of the model into discrete layers of a specific density, whereas in the SEM images there it can be seen that there is no clear demarcation defining each individual layer. Furthermore, the sum total of the thickness given by the optical model is within 10% of that of the SEM. Using this approach, we can use the theoretically generated model to predict the transmissivity behavior of the films for varying angles of incidence.

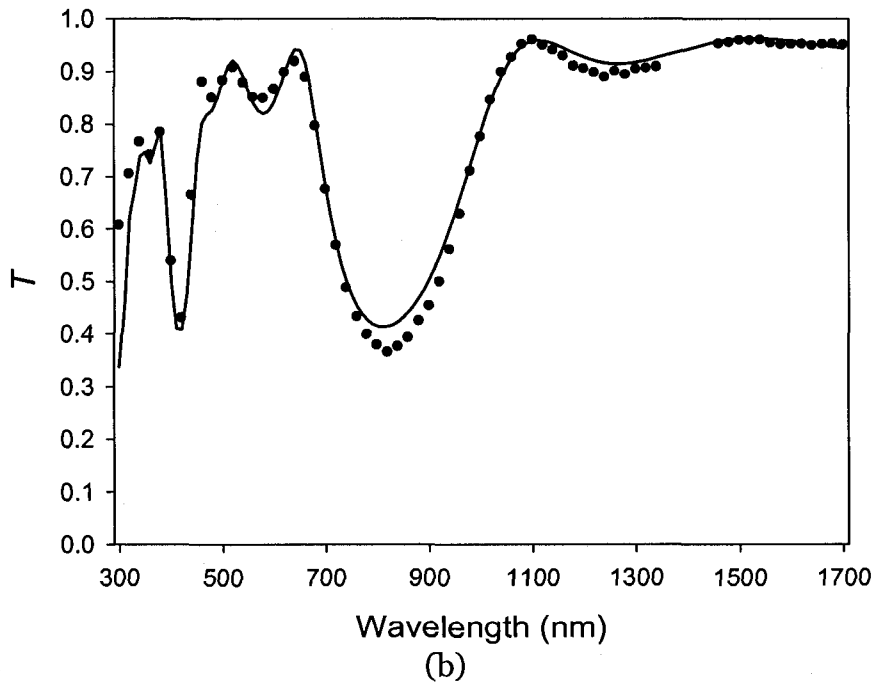
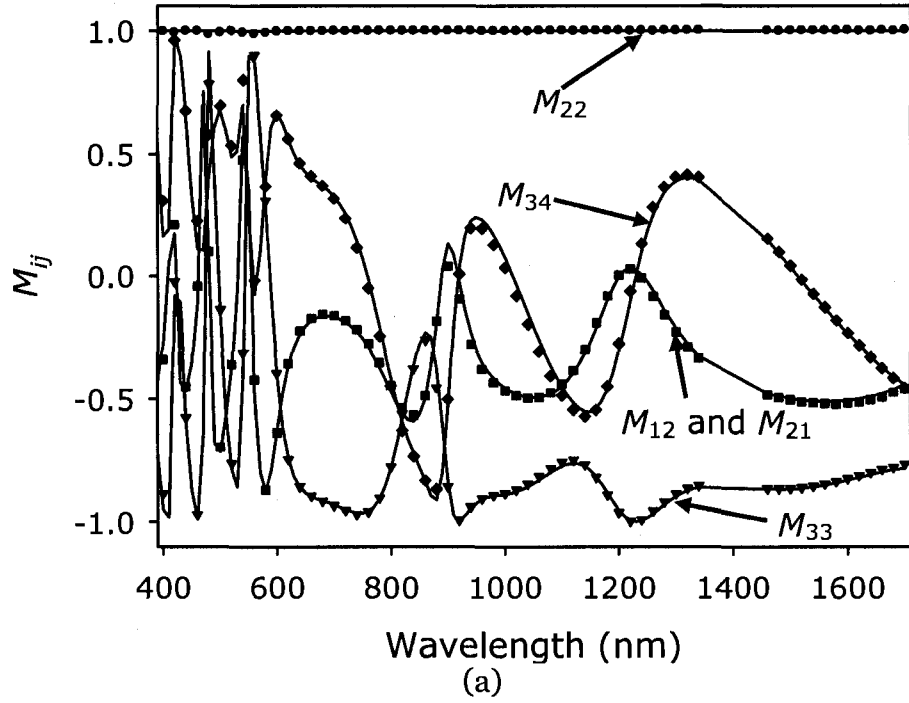


Figure 58 – Experimental (●,◆,■,▼) and model (solid line) curves for (a) normalized Mueller matrix data of the as-deposited film from set A on a silicon substrate measured at a reflectance angle of  $50^\circ$ , and (b) the normal incidence transmissivity for the as-deposited film from set A on a fused silica substrate. For the sake of clarity, the  $M_{ij}$  elements near zero were not shown, and only every second experimental data point is shown.

To apply this approach to the annealed films, we characterized the large change in the optical constants caused by the annealing process by studying a  $\text{Y}_2\text{O}_3:\text{Eu}$  film grown at  $\alpha = 0^\circ$  to produce a solid film of approximate thickness of 70 nm. We then obtained the optical constants for the material both as-deposited and annealed. The resultant model fit for a sample annealed at  $600^\circ\text{C}$ , along with its optical constants using Cauchy and Urbach dispersion (with a band-edge set to 200 nm) are shown in Fig. 59. These resultant optical constants were then applied to the model transmittance for film set A annealed at  $600^\circ\text{C}$ , which is shown in Fig. 60. Initial attempts to better describe the optical constants were made by fitting previously published charge transitions for micro-crystalline and nano-crystalline  $\text{Y}_2\text{O}_3:\text{Eu}$  [129] to Tauc-Lorentz oscillator shapes [90, 91] (Fig. 61). The nanocrystalline fit is shown as the solid line in the inset of Fig. 61. It is also important to note at this point that although the oscillator peak in reference [129] occurs at a wavelength of 254 nm for the nano-crystalline case (which would more accurately represent our films), the laser wavelength of 266 nm is significantly enough removed from this peak that the use of Urbach absorption is not an unreasonable approximation, as can be seen in Fig. 61. It was found that although the electron transitions worked well with a Tauc-Lorentz description, these results did not apply well to our films. Further investigation is required to account for this inconsistency.

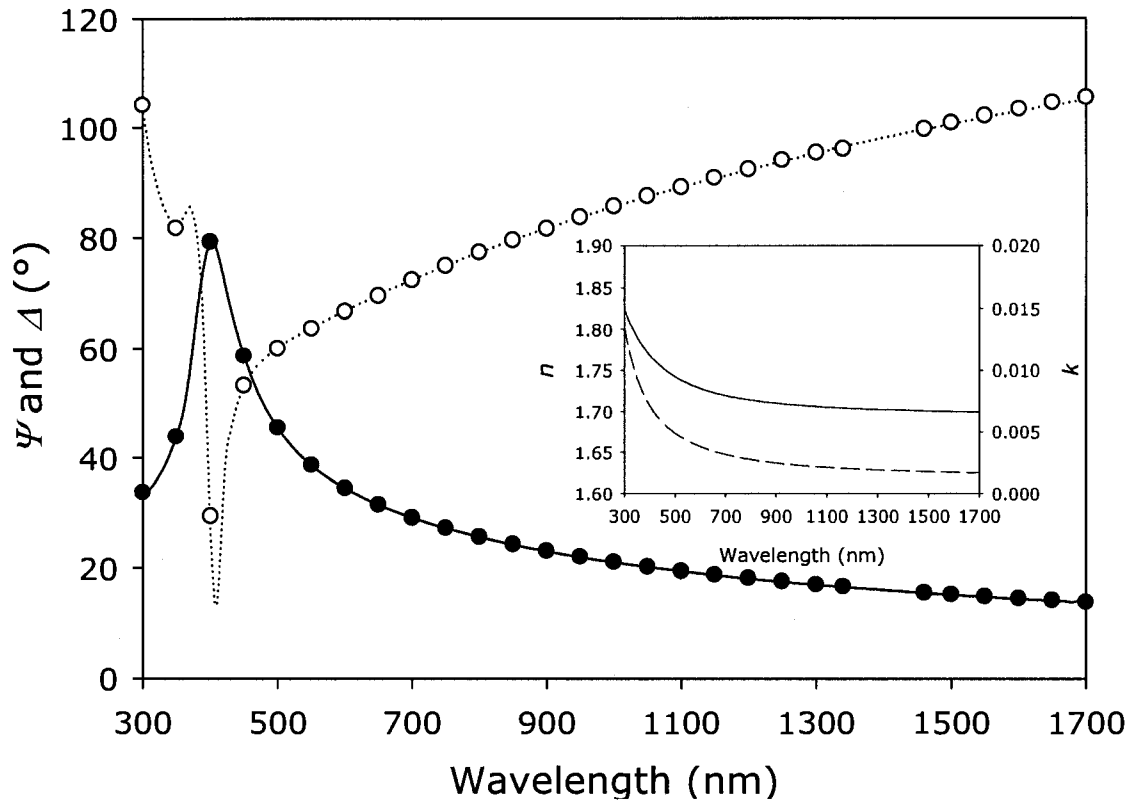


Figure 59 – Experimental Psi (●) and Delta (○) and with best model fits (solid and dashed lines) for a 69 nm thick  $Y_2O_3:Eu$  film deposited at  $\alpha = 0^\circ$  annealed at  $600^\circ C$ . Only every 5<sup>th</sup> experimental point and only an angle of incidence of  $70^\circ$  is shown for the sake of clarity. Also shown (inset) is the resultant  $n$  (solid) and  $k$  (dashed) using Cauchy and Urbach dispersion.

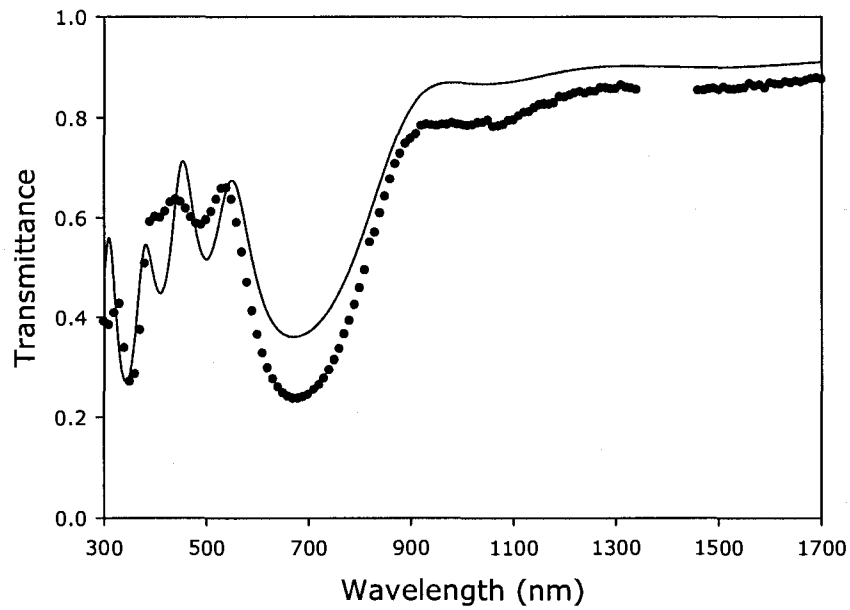


Figure 60 – Model (-) and experimental (●) transmission of film set A on fused silica after annealing at 600°C.

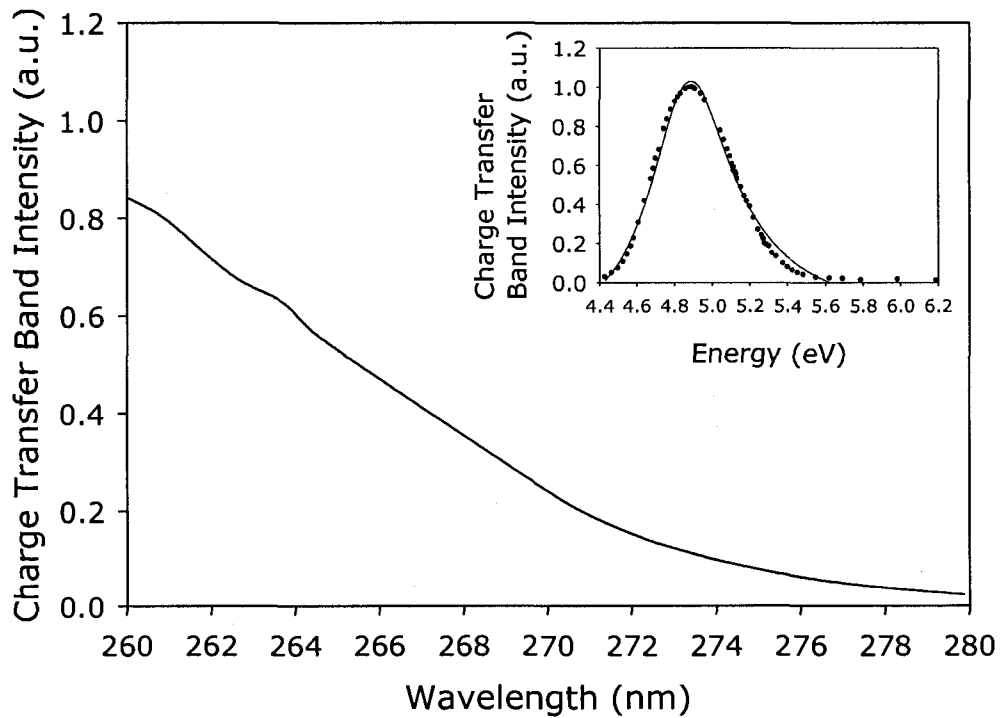


Figure 61 – Charge transfer band intensity for nano-crystalline  $Y_2O_3:Eu$  as a function of wavelength as quoted by Igarishi *et al*[129]. The inset is the complete band as a function of energy (●) with a Tauc-Lorentz oscillator function[90, 91] applied to it (solid).



By using the previous model result for films from set A annealed at 600°C, we then predicted the emission profile,  $EP$ , for films from set A for angles of incidence from 0° to 80°, by multiplying a weighted average of the  $p$ - and  $s$ -transmission (which accounts for preferential emission of  $p$ -polarized light) at a wavelength of 611 nm by the  $p$ -polarized transmission at the linearly polarized laser wavelength of 266 nm as a function of detector angle (accounting for the angular difference between the viewing angle and the laser incidence angle) to generate the expected emission profile (in arbitrary units). This expression is given in (6.2.1):

$$EP = \frac{T_{p,266nm}}{2} \left( T_{p,611nm} \left( \frac{T_{p,611nm}}{T_{p,611nm} + T_{s,611nm}} \right) + T_{s,611nm} \left( \frac{T_{s,611nm}}{T_{p,611nm} + T_{s,611nm}} \right) \right) \quad (6.2.1)$$

By applying (6.2.1), we obtain a comparison between the measured emission and predicted profile, as can be seen in Fig. 62 with the result in Fig. 55 overlaid for comparison. Although the agreement is not exact, the general trend is quite similar in that the emission decreases slightly at off-normal viewing angles, and then increases with viewing angle, peaking around 60° to 70° with respect to substrate normal. The most probable reason for the discrepancy is that the model's primary Bragg resonance does not occur at precisely the same wavelength as the experimental one (shown in Fig. 60), and that there is an artificially high level of transmission in the model. Other sources of discrepancy between the model and experimental data are: uncertainty in the accuracy of the optical constants to describe this particular film; cracking and delamination of

the film after annealing not accounted for in the optical model; and increased scattering in the annealed films.

Although Fig. 62 accounted for the changing angle at which the laser light was incident on the surface of the sample at the various emission angles, the angular emission profile for the case of normally incident excitation laser light for all emission angles is of more interest. Using the model, we can predict the emission profile for normal incidence excitation light was developed by calculating the weighted average of the *p*- and *s*-polarized light transmission for the emission wavelength as a function of emission angle. This result is shown in Fig. 63. As can be seen, this suggests that by tailoring the periodicity as well as tailoring the excitation wavelength angle of incidence, it is possible to tune the angular distribution of the emission.

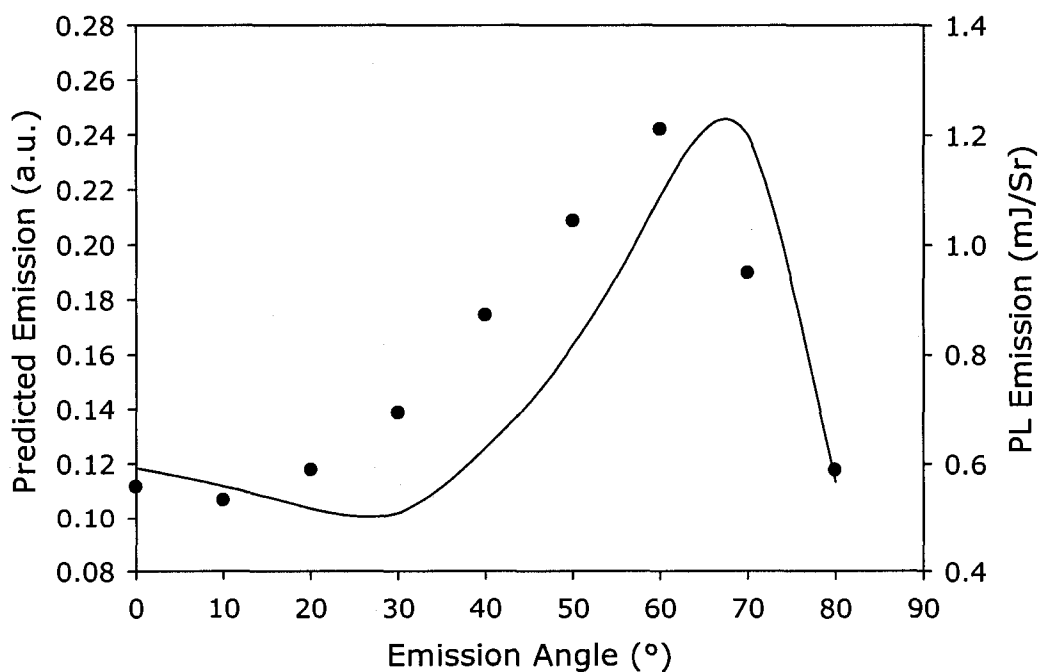


Figure 62 - Angular emission pattern for films from set A (●) along with the predicted angular emission pattern from the model (solid) with a correction factor accounting for the laser incidence angle.

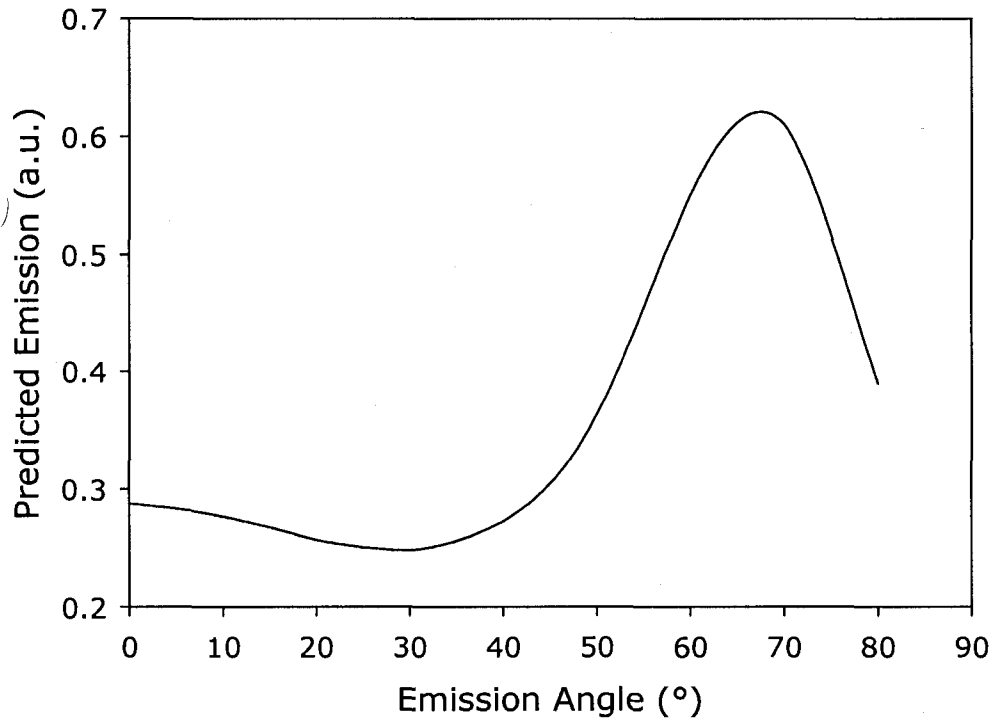


Figure 63 - Predicted angular emission pattern for films from set A using the model assuming the excitation source is normally incident for all emission angles.

## **7 – Summary and Conclusions**

### ***7.1 – Summary***

Thin films produced by glancing angle deposition (GLAD) have been shown by numerous authors to have interesting and useful physical properties. GLAD-grown films of optical materials can be characterized using ellipsometry leading eventually to optimization of the optical properties.

In this study, spectroscopic ellipsometry techniques were used to characterize GLAD produced films. The theoretical framework for the optical description of GLAD produced films was examined using effective medium approximations and Berreman's method. Also examined was the theory behind optical constant dispersion and various dispersion relations to describe optical media.

This framework was then applied to both inorganic and organic columnar films produced by GLAD. Inorganic films composed of  $\text{MgF}_2$ ,  $\text{SiO}_2$ ,  $\text{Al}_2\text{O}_3$ , and  $\text{TiO}_2$  were found to have biaxial or uniaxial optical anisotropy, which depended on the morphology of the film. The index of refraction and density in these materials were characterized as function of deposition angle, and were found to be in agreement with previous works. This framework was then applied to organic  $\text{Alq}_3$  revealing properties distinct from the inorganic metal oxides and fluorides typically used in GLAD. The index of refraction gradient for  $\text{SiO}_2$  was examined by characterizing the index change in solid films throughout long

depositions, as well as through experiments on eliminating water in the pores, and by examining finite wavelength EMAs.

An extension to this work was then applied to examining the effect of periodic arrangement of GLAD columns on the global film properties. It was found that periodically arranged silicon posts had a higher overall index of refraction in the IR as compared with the same film with random column growth. Also examined was the usage of ellipsometry models to predict the photoluminescent emission patterns of periodically layered GLAD films composed of a photoluminescent material. Periodic high-low stacks of  $Y_2O_3:Eu$  were found to have a non-Lambertian emission profile, which was predicted by using ellipsometry models.

## ***7.2 – Impact of this Work***

Ellipsometry was found to be a powerful tool for characterizing GLAD films. Through the flexibility of the tool, as demonstrated throughout this work, we can examine GLAD films at the most basic level by starting with a simple solid film and model it using various dispersion relations, which can then be extended to a simple GLAD structure such as tilted or vertical columns. This yields much information about the fundamental nature of the material, such as the indices of refraction, the film density, and the optical dispersion relations. Alternatively, we can use the fundamental properties of the aforementioned simple films, and apply the information to the study of GLAD films with complex morphologies. In this case, we can use the model to predict complicated optical properties of these

complex film morphologies. From this, we can use other characterization techniques to further enhance the body of knowledge for a given film.

At the onset of this work, any discussion involving the fundamental optical properties of GLAD films was limited to a handful of measurements related to chiral Bragg resonances, and approximate calculations of the average index based on rough estimates of the film density. As this work first began development, it yielded much information on the most basic GLAD film structures such as the index of refraction and packing fraction. Since then, the technique has been used to evaluate complex materials and structures, and is now routinely used by many within the research group. Over the course of this study, ellipsometry data on GLAD films has provided useful wavelength resolved calibration data for studies from sensor applications for GLAD, to the development of Bragg optical filters, and has further provided useful information on the growth of various materials.

This work extended the body of knowledge of GLAD films. In that, this work has yielded the optical constants for inorganic and organic GLAD columns. It has yielded information about the density of GLAD produced films, as well as the structural orientation of the columns in the films. Further, this work has demonstrated the applicability of the technique to the characterization of complicated GLAD structures. More importantly, this work has provided a recipe for the characterization of future GLAD films through the use of the methods and techniques examined throughout this thesis.

### **7.3 – Future Work**

This work has provided the back-bone for many possible future studies using ellipsometric characterization of GLAD films. One possible examination would be to study GLAD films which have been infiltrated with a liquid, polymer or liquid crystal material. This may be used as a powerful measurement to understanding the effects of liquid adsorption within the porous GLAD structure, as well as possible information about the alignment of the molecules within the liquid. Another possible study could be to examine the optical properties of GLAD films during the early stages of growth, since ellipsometry is, in principle, sensitive to the presence of very thin films. This may lead to important information about the film growth evolution. Another study could be to examine the morphological changes in GLAD films during variable  $\alpha$  depositions to examine the effect that the change in effective shadowing due to the changing  $\alpha$ , as compared with depositions at a fixed  $\alpha$ . Another examination that could be performed is the examination of the optical properties of films deposited using the PhiSweep technique, as the resultant films can be produced with varying degrees of porosity. These are but a few ideas that could be examined using the ellipsometry technique; it is certain that there is many more that the reader could dream up.

## References

- [1] D. Vick, Y. Y. Tsui, M. J. Brett, and R. Fedosejevs, "Production of porous carbon thin films by pulsed laser deposition," *Thin Solid Films*, vol. 350, pp. 49-52, 1999.
- [2] K. Robbie and M. J. Brett, "Glancing angle deposition of thin films," in *US Patent*. United States: The Governors of the University of Alberta and Alberta Microelectronic Corporation, 2001.
- [3] K. Robbie and M. J. Brett, "Shadow sculpted thin films," in *US Patent*. United States: Micralyne Inc., 2001.
- [4] K. Robbie, J. C. Sit, and M. J. Brett, "Advanced techniques for glancing angle deposition," *J. Vac. Sci. Technol. B*, vol. 16, pp. 1115-1122, 1998.
- [5] M. J. Colgan and M. J. Brett, "Field emission from carbon and silicon films with pillar microstructure," *Thin Solid Films*, vol. 389, pp. 1-4, 2001.
- [6] B. Dick, M. J. Brett, and T. Smy, "Controlled growth of periodic pillars by glancing angle deposition," *J. Vac. Sci. Technol. B*, vol. 21, pp. 23-28, 2003.
- [7] B. Dick, M. J. Brett, T. J. Smy, M. R. Freeman, M. Malac, and R. F. Egerton, "Periodic magnetic microstructures by glancing angle deposition," *J. Vac. Sci. Technol. A*, vol. 18, pp. 1838-1844, 2000.
- [8] K. D. Harris, A. Huizinga, and M. J. Brett, "High-speed porous thin film humidity sensors," *Electrochem. Solid-State Lett.*, vol. 5, pp. H27-H29, 2002.
- [9] K. D. Harris, D. Vick, T. Smy, and M. J. Brett, "Column angle variations in porous chevron thin films," *J. Vac. Sci. Technol. A*, vol. 20, pp. 2062-2067, 2002.
- [10] K. D. Harris, D. Vick, E. J. Gonzalez, T. Smy, K. Robbie, and M. J. Brett, "Porous thin films for thermal barrier coatings," *Surf. Coat. Tech.*, vol. 138, pp. 185-191, 2001.
- [11] M. O. Jensen and M. J. Brett, "Porosity engineering in glancing angle deposition thin films," *Appl. Phys. A-Mater.*, vol. 80, pp. 763-768, 2005.
- [12] S. R. Kennedy, M. J. Brett, O. Toader, and S. John, "Fabrication of tetragonal square spiral photonic crystals," *Nano Lett.*, vol. 2, pp. 59-62, 2002.
- [13] M. Malac, R. F. Egerton, M. J. Brett, and B. Dick, "Fabrication of submicrometer regular arrays of pillars and helices," *J. Vac. Sci. Technol. B*, vol. 17, pp. 2671-2674, 1999.
- [14] M. W. Seto, B. Dick, and M. J. Brett, "Microsprings and microcantilevers: studies of mechanical response," *J. Micromech. Microeng.*, vol. 11, pp. 582-588, 2001.
- [15] M. W. Seto, B. Dick, and M. J. Brett, "Nanoindentation of microspring thin films," presented at Materials Science of Microelectromechanical Systems (MEMS) Devices III. Symposium, Boston, MA, USA, 2001.



- [16] J. J. Steele, J. Gospodyn, J. C. Sit, and M. J. Brett, "Impact of morphology on high-speed humidity sensor performance," *IEEE Sensors*, vol. 6, pp. 24-27, 2006.
- [17] D. Vick, T. Smy, and M. J. Brett, "Growth behavior of evaporated porous thin films," *J. Mater. Res.*, vol. 17, pp. 2904-2911, 2002.
- [18] T. Karabacak, G. C. Wang, and T. M. Lu, "Physical self-assembly and the nucleation of three-dimensional nanostructures by oblique angle deposition," *J. Vac. Sci. Technol. A*, vol. 22, pp. 1778-1784, 2004.
- [19] M. M. Hawkeye and M. J. Brett, "Narrow bandpass optical filters fabricated with one-dimensionally periodic inhomogeneous thin films," *J. Appl. Phys.*, vol. 100, pp. 044322, 2006.
- [20] P. C. P. Hrudey, M. Taschuk, Y. Y. Tsui, R. Fedosejevs, J. C. Sit, and M. J. Brett, "Evaporated nanostructured  $Y_2O_3 : Eu$  thin films," *J. Nanosci. Nanotechnol.*, vol. 5, pp. 229-234, 2005.
- [21] P. C. P. Hrudey, M. Taschuk, Y. Y. Tsui, R. Fedosejevs, and M. J. Brett, "Optical properties of porous nanostructured  $Y_2O_3 : Eu$  thin films," *J. Vac. Sci. Technol. A*, vol. 23, pp. 856-861, 2005.
- [22] M. O. Jensen and M. J. Brett, "Square spiral 3D photonic bandgap crystals at telecommunications frequencies," *Opt. Express.*, vol. 13, pp. 3348, 2005.
- [23] K. Kaminska, A. Amassian, L. Martinu, and K. Robbie, "Growth of vacuum evaporated ultraporous silicon studied with spectroscopic ellipsometry and scanning electron microscopy," *J. Appl. Phys.*, vol. 97, pp. 013511, 2005.
- [24] K. Kaminska and K. Robbie, "Birefringent omnidirectional reflector," *Appl. Optics*, vol. 43, pp. 1570-1576, 2004.
- [25] K. Kaminska, T. Brown, G. Beydaghyan, and K. Robbie, "Vacuum evaporated porous silicon photonic interference filters," *Appl. Optics*, vol. 42, pp. 4212-4219, 2003.
- [26] K. Kaminska, M. Suzuki, K. Kimura, Y. Taga, and K. Robbie, "Simulating structure and optical response of vacuum evaporated porous rugate filters," *J. Appl. Phys.*, vol. 95, pp. 3055-62, 2004.
- [27] S. R. Kennedy and M. J. Brett, "Porous broadband antireflection coating by glancing angle deposition," *Appl. Optics*, vol. 42, pp. 4573-4579, 2003.
- [28] S. R. Kennedy, J. C. Sit, D. J. Broer, and M. J. Brett, "Optical activity of chiral thin film and liquid crystal hybrids," *Liquid Crystals*, vol. 28, pp. 1799-1803, 2001.
- [29] K. Robbie, M. J. Brett, and A. Lakhtakia, "First thin film realization of a helicoidal bianisotropic medium," *J. Vac. Sci. Technol. A*, vol. 13, pp. 2991-2993, 1995.
- [30] J. C. Sit, D. J. Broer, and M. J. Brett, "Liquid crystal alignment and switching in porous chiral thin films," *Adv. Mater.*, vol. 12, pp. 371-373, 2000.

- [31] J. C. Sit, D. J. Broer, and M. J. Brett, "Alignment and switching of nematic liquid crystals embedded in porous chiral thin films," *Liquid Crystals*, vol. 27, pp. 387-391, 2000.
- [32] A. C. van Popta, M. J. Brett, and J. C. Sit, "Double-handed circular Bragg phenomena in polygonal helix thin films," *J. Appl. Phys.*, vol. 98, pp. 083517, 2005.
- [33] A. C. van Popta, J. C. Sit, and M. J. Brett, "Optical properties of porous helical thin films," *Appl. Optics*, vol. 43, pp. 3632-3639, 2004.
- [34] A. C. van Popta, S. R. Kennedy, D. J. Broer, J. C. Sit, and M. J. Brett, "Optical performance of porous TiO<sub>2</sub> chiral thin films," presented at Nanomaterials and their optical applications, San Diego, CA, USA, 2003.
- [35] A. C. van Popta, M. M. Hawkeye, J. C. Sit, and M. J. Brett, "Gradient-index narrow-bandpass filter fabricated with glancing-angle deposition," *Opt. Lett.*, vol. 29, pp. 2545-2547, 2004.
- [36] S. H. Woo and C. K. Hwangbo, "Optical anisotropy of TiO<sub>2</sub> and MgF<sub>2</sub> thin films prepared by glancing angle deposition," *J. Korean Phys. Soc.*, vol. 49, pp. 2136-2142, 2006.
- [37] R. M. A. Azzam and N. M. Bashara, *Ellipsometry and polarized light*. New York: North-Holland Pub. Co., 1977.
- [38] H. G. Tompkins and W. A. McGahan, *Spectroscopic ellipsometry and reflectometry: A user's guide*. New York: Wiley, 1999.
- [39] J. A. Woollam, B. Johs, C. M. Herzinger, J. Hilfiker, R. Synowicki, and C. L. Bungay, "Overview of Variable Angle Spectroscopic Ellipsometry (VASE), Part I: Basic Theory and Typical Applications," presented at Optical Metrology, Denver, 1999.
- [40] B. Johs, J. A. Woollam, C. M. Herzinger, J. Hilfiker, R. Synowicki, and C. L. Bungay, "Overview of Variable Angle Spectroscopic Ellipsometry (VASE), Part II: Advanced Applications," presented at Optical Metrology, Denver, 1999.
- [41] R. W. Collins, I. An, C. Chen, A. S. Ferlauto, and J. A. Zapien, "Advances in multichannel ellipsometric techniques for in-situ and real-time characterization of thin films," *Thin Solid Films*, vol. 469-470, pp. 38-46, 2004.
- [42] R. W. Collins, "Automatic rotating element ellipsometers - calibration, operation, and real-time applications," *Rev. Sci. Instrum.*, vol. 61, pp. 2029-2062, 1990.
- [43] G. E. Jellison, "The calculation of thin film parameters from spectroscopic ellipsometry data," *Thin Solid Films*, vol. 291, pp. 40-45, 1996.
- [44] J. Lee, J. Koh, and R. W. Collins, "Multichannel Mueller matrix ellipsometer for real-time spectroscopy of anisotropic surfaces and films," *Opt. Lett.*, vol. 25, pp. 1573-1575, 2000.
- [45] M. Schubert, "Generalized ellipsometry and complex optical systems," *Thin Solid Films*, vol. 313, pp. 323-332, 1998.

- [46] I. Hodgkinson and Q. H. Wu, "Vacuum deposited biaxial thin films with all principal axes inclined to the substrate," *J. Vac. Sci. Technol. A*, vol. 17, pp. 2928-2932, 1999.
- [47] I. Hodgkinson, Q. H. Wu, and S. Collet, "Dispersion equations for vacuum-deposited tilted-columnar biaxial media," *Appl. Optics*, vol. 40, pp. 452-457, 2001.
- [48] M. Schubert, B. Rheinlander, C. Cramer, H. Schmiedel, J. A. Woollam, C. M. Herzinger, and B. Johs, "Generalized transmission ellipsometry for twisted biaxial dielectric media: Application to chiral liquid crystals," *J. Opt. Soc. Am. A*, vol. 13, pp. 1930-1940, 1996.
- [49] M. Schubert and W. Dollase, "Generalized ellipsometry for biaxial absorbing materials: determination of crystal orientation and optical constants of  $Sb_2S_3$ ," *Opt. Lett.*, vol. 27, pp. 2073-2075, 2002.
- [50] J. Gospodyn and J. C. Sit, "Characterization of dielectric columnar thin films by variable angle Mueller matrix and spectroscopic ellipsometry," *Optical Materials*, vol. 29, pp. 318-325, 2006.
- [51] T. C. Choy, *Effective medium theory : principles and applications*. New York: Clarendon Press, 1999.
- [52] D. E. Aspnes, "Optical properties of thin films," *Thin Solid Films*, vol. 89, pp. 249-262, 1982.
- [53] C. Brosseau, A. Beroual, and A. Boudida, "How do shape anisotropy and spatial orientation of the constituents affect the permittivity of dielectric heterostructures?," *J. Appl. Phys.*, vol. 88, pp. 7278-7288, 2000.
- [54] D. Gershon, J. P. Calame, and A. Birnboim, "Complex permittivity measurements and mixing laws of porous alumina," *J. Appl. Phys.*, vol. 89, pp. 8117-8120, 2001.
- [55] B. Sareni, L. Krahenbuhl, A. Beroual, and C. Brosseau, "Effective dielectric constant of random composite materials," *J. Appl. Phys.*, vol. 81, pp. 2375-2383, 1997.
- [56] B. Sareni, L. Krahenbuhl, and C. Brosseau, "Effective dielectric constant of periodic composite materials," *J. Appl. Phys.*, vol. 80, pp. 1688-1696, 1996.
- [57] S. Teitler and B. W. Henvis, "Refraction in Stratified, Anisotropic Media," *J. Opt. Soc. Am.*, vol. 60, pp. 830-834, 1970.
- [58] D. W. Berreman, "Optics in Stratified and Anisotropic Media - 4x4-Matrix Formulation," *J. Opt. Soc. Am.*, vol. 62, pp. 502-510, 1972.
- [59] P. Yeh, "Electromagnetic Propagation in Birefringent Layered Media," *J. Opt. Soc. Am.*, vol. 69, pp. 742-756, 1979.
- [60] P. Yeh, "Optics of Anisotropic Layered Media - a New 4x4 Matrix Algebra," *Surf Sci*, vol. 96, pp. 41-53, 1980.
- [61] M. Schubert, "Polarization-dependent optical parameters of arbitrarily anisotropic homogeneous layered systems," *Phys. Rev. B*, vol. 53, pp. 4265-4274, 1996.

- [62] B. A. Movchan and A. Demchishin, "Study of structure and properties of thick vacuum condensates of nickel, titanium, tungsten, aluminium oxide and zirconium dioxide," *Phys. Metals Metallog.*, vol. 28, pp. 83, 1969.
- [63] J. A. Thornton, "High-rate thick-film growth," *Annu. Rev. Mater. Sci.*, vol. 7, pp. 239-260, 1977.
- [64] R. N. Tait, T. Smy, and M. J. Brett, "Modeling and characterization of columnar growth in evaporated-films," *Thin Solid Films*, vol. 226, pp. 196-201, 1993.
- [65] J. C. Sit, D. Vick, K. Robbie, and M. J. Brett, "Thin film microstructure control using glancing angle deposition by sputtering," *J. Mater. Res.*, vol. 14, pp. 1197-1199, 1999.
- [66] K. Robbie and M. J. Brett, "Sculptured thin films and glancing angle deposition: Growth mechanics and applications," *J. Vac. Sci. Technol. A*, vol. 15, pp. 1460-1465, 1997.
- [67] M. O. Jensen, S. R. Kennedy, and M. J. Brett, "Fabrication of periodic arrays of nanoscale square helices," presented at Nano-/Microstructured Materials, San Francisco, CA, USA, 2002.
- [68] S. R. Kennedy and M. J. Brett, "Advanced techniques for the fabrication of square spiral photonic crystals by glancing angle deposition," *J. Vac. Sci. Technol. B*, vol. 22, pp. 1184-1190, 2004.
- [69] M. W. Seto, K. Robbie, D. Vick, M. J. Brett, and L. Kuhn, "Mechanical response of thin films with helical microstructures," *J. Vac. Sci. Technol. B*, vol. 17, pp. 2172-2177, 1999.
- [70] A. Lakhtakia, "Dielectric sculptured thin films for polarization-discriminatory handedness-inversion of circularly polarized light," *Opt. Eng.*, vol. 38, pp. 1596-1602, 1999.
- [71] L. Hodgkinson, Q. H. Wu, B. Knight, A. Lakhtakia, and K. Robbie, "Vacuum deposition of chiral sculptured thin films with high optical activity," *Appl. Optics*, vol. 39, pp. 642-9, 2000.
- [72] K. Robbie, D. J. Broer, and M. J. Brett, "Chiral nematic order in liquid crystals imposed by an engineered inorganic nanostructure," *Nature*, vol. 399, pp. 764-766, 1999.
- [73] K. Robbie, M. J. Brett, and A. Lakhtakia, "Chiral sculptured thin films," *Nature*, vol. 384, pp. 616-616, 1996.
- [74] K. Kaminska, T. Brown, G. Beydaghyan, and K. Robbie, "Rugate filters grown by glancing angle deposition," *Proceedings of the SPIE - The International Society for Optical Engineering*, vol. 4833, pp. 633-9, 2002.
- [75] A. Lakhtakia, V. C. Venugopal, and M. W. McCall, "Spectral holes in Bragg reflection from chiral sculptured thin films: circular polarization filters," *Opt. Commun.*, vol. 177, pp. 57-68, 2000.

- [76] J. A. Woollam, "Ellipsometry, Variable Angle Spectroscopic," in *Wiley Encyclopedia of Electrical and Electronics Engineering*, J. G. Webster, Ed. Toronto: John Wiley & Sons, Inc., 2000, pp. 109-117.
- [77] R. W. Collins, I. An, H. Fujiwara, J. C. Lee, Y. W. Lu, J. Y. Koh, and P. I. Rovira, "Advances in multichannel spectroscopic ellipsometry," *Thin Solid Films*, vol. 313, pp. 18-32, 1998.
- [78] J. Lee, P. I. Rovira, I. An, and R. W. Collins, "Rotating-compensator multichannel ellipsometry: Applications for real time Stokes vector spectroscopy of thin film growth," *Rev. Sci. Instrum.*, vol. 69, pp. 1800-1810, 1998.
- [79] J. Lee, J. Koh, and R. W. Collins, "Dual rotating-compensator multichannel ellipsometer: Instrument development for high-speed Mueller matrix spectroscopy of surfaces and thin films," *Rev. Sci. Instrum.*, vol. 72, pp. 1742-1754, 2001.
- [80] B. E. A. Saleh and M. C. Teich, *Fundamentals of photonics*. New York: Wiley, 1991.
- [81] P. Yeh and C. Gu, *Optics of Liquid Crystal Displays*. New York: Wiley, 1999.
- [82] C. F. Bohren and D. R. Huffman, *Absorption and scattering of light by small particles*. New York: Wiley, 1983.
- [83] R. A. Chipman, "Depolarization index and the average degree of polarization," *Appl. Optics*, vol. 44, pp. 2490-2495, 2005.
- [84] C. Chen, I. An, G. M. Ferreira, N. J. Podraza, J. A. Zapien, and R. W. Collins, "Multichannel Mueller matrix ellipsometer based on the dual rotating compensator principle," *Thin Solid Films*, vol. 455-56, pp. 14-23, 2004.
- [85] N. J. Podraza, C. Chen, I. An, G. M. Ferreira, P. I. Rovira, R. Messier, and R. W. Collins, "Analysis of the optical properties and structure of sculptured thin films from spectroscopic Mueller matrix ellipsometry," *Thin Solid Films*, vol. 455-56, pp. 571-575, 2004.
- [86] D. J. Griffiths, *Introduction to electrodynamics*, 3rd ed. Upper Saddle River, N.J.: Prentice Hall, 1999.
- [87] H. Goldstein, *Classical mechanics*. Cambridge, Mass.: Addison-Wesley Press, 1950.
- [88] G. E. Jellison, "Spectroscopic ellipsometry data analysis: measured versus calculated quantities," *Thin Solid Films*, vol. 313, pp. 33-39, 1998.
- [89] A. C. van Popta, K. R. van Popta, J. C. Sit, and M. J. Brett, "Sidelobe suppression in chiral optical filters by apodization of the local form birefringence," *J. Opt. Soc. Am. A*, 2007.
- [90] G. E. Jellison and F. A. Modine, "Parameterization of the optical functions of amorphous materials in the interband region," *Appl. Phys. Lett.*, vol. 69, pp. 371-373, 1996.

- [91] G. E. Jellison and F. A. Modine, "Parameterization of the optical functions of amorphous materials in the interband region (erratum)," *Appl. Phys. Lett.*, vol. 69, pp. 2137-2137, 1996.
- [92] J. D. Jackson, *Classical Electrodynamics*, 3rd ed. New York: Wiley, 1999.
- [93] G. Ghosh, "Dispersion-equation coefficients for the refractive index and birefringence of calcite and quartz crystals," *Opt. Commun.*, vol. 163, pp. 95-102, 1999.
- [94] W. H. Press, *Numerical recipes in C : the art of scientific computing*. Cambridge [Cambridgeshire] ; New York: Cambridge University Press, 1988.
- [95] M. J. Dodge, "Refractive properties of magnesium fluoride," *Appl. Optics*, vol. 23, pp. 1980-1985, 1984.
- [96] C. M. Herzinger, B. Johs, W. A. McGahan, J. A. Woollam, and W. Paulson, "Ellipsometric determination of optical constants for silicon and thermally grown silicon dioxide via a multi-sample, multi-wavelength, multi-angle investigation," *J. Appl. Phys.*, vol. 83, pp. 3323-3336, 1998.
- [97] E. D. Palik, "Handbook of optical constants of solids," E. D. Palik, Ed. San Diego: Academic Press, 1998, pp. 804.
- [98] M. J. Brett, S. K. Dew, and T. J. Smy, "Thin Film Microstructure and Process Simulation using SIMBAD," in *Modelling of Film Deposition for Microelectronic Applications*, vol. Thin Films Volume 22, *Thin Films*, S. Rosnagel and A. Ulman, Eds.: Academic Press, 1996, pp. 1-79.
- [99] S. Tsoi, E. Fok, J. C. Sit, and J. G. C. Veinot, "Superhydrophobic, high surface area, 3-D SiO<sub>2</sub> nanostructures through siloxane-based surface functionalization," *Langmuir*, vol. 20, pp. 10771-10774, 2004.
- [100] Z. M. Rittersma, "Recent achievements in miniaturised humidity sensors - a review of transduction techniques," *Sensor. Actuat. a-Phys.*, vol. 96, pp. 196-210, 2002.
- [101] T. Smy, D. Vick, M. J. Brett, S. K. Dew, A. T. Wu, J. C. Sit, and K. D. Harris, "Three-dimensional simulation of film microstructure produced by glancing angle deposition," *J. Vac. Sci. Technol. A*, vol. 18, pp. 2507-2512, 2000.
- [102] F. Vratny and F. Micale, "Reflectance Spectra of Non-Stoichiometric Titanium Oxide, Niobium Oxide, and Vanadium Oxide," *T Faraday Soc*, vol. 59, pp. 2739-&, 1963.
- [103] M. M. Hawkeye, "personal communication." Edmonton, 2006.
- [104] P. C. P. Hrudey, K. L. Westra, and M. J. Brett, "Highly ordered organic Alq<sub>3</sub> chiral luminescent thin films fabricated by glancing-angle deposition," *Adv. Mater.*, vol. 18, pp. 224-228, 2006.
- [105] P. C. P. Hrudey, B. Szeto, and M. J. Brett, "Strong circular Bragg phenomena in self-ordered porous helical nanorod arrays of Alq(3)," *Appl. Phys. Lett.*, vol. 88, pp. -, 2006.

- [106] B. Szeto, P. C. P. Hrudey, J. Gospodyn, J. C. Sit, and M. J. Brett, "Obliquely deposited tris(8-hydroxyquinoline) aluminium (Alq<sub>3</sub>) biaxial thin films with negative in-plane birefringence," *J. Opt. A-Pure Appl. Op.*, vol. 9, pp. 457-462, 2007.
- [107] A. B. Djuricic, C. Y. Kwong, W. L. Guo, T. W. Lau, E. H. Li, Z. T. Liu, H. S. Kwok, L. S. M. Lam, and W. K. Chan, "Spectroscopic ellipsometry of the optical functions of tris (8-hydroxyquinoline) aluminum (Alq<sub>3</sub>)," *Thin Solid Films*, vol. 416, pp. 233-241, 2002.
- [108] A. B. Djuricic, C. Y. Kwong, T. W. Lau, E. H. Li, Z. T. Liu, H. S. Kwok, L. S. M. Lam, and W. K. Chan, "Optical functions of tris (8-hydroxyquinoline) aluminum (Alq<sub>3</sub>) by spectroscopic ellipsometry," *Appl. Phys. A-Mater.*, vol. 76, pp. 219-223, 2003.
- [109] D. Vick and M. J. Brett, "Conduction anisotropy in porous thin films with chevron microstructures," *J. Vac. Sci. Technol. A*, vol. 24, pp. 156-164, 2006.
- [110] Y. Taga and T. Motohiro, "Growth of Birefringent Films by Oblique Deposition," *J Cryst Growth*, vol. 99, pp. 638-642, 1990.
- [111] T. Motohiro and Y. Taga, "Thin film retardation plate by oblique deposition," *Appl. Optics*, vol. 28, pp. 2466-2482, 1989.
- [112] J. J. Steele, A. C. van Popta, M. M. Hawkeye, J. C. Sit, and M. J. Brett, "Nanostructured gradient index optical filter for high-speed humidity sensing," *Sensor Actuat B-Chem*, vol. 120, pp. 213-219, 2006.
- [113] D. Stroud and F. P. Pan, "Self-Consistent Approach to Electromagnetic-Wave Propagation in Composite Media - Application to Model Granular Metals," *Phys. Rev. B*, vol. 17, pp. 1602-1610, 1978.
- [114] W. G. Egan and D. E. Aspnes, "Finite-Wavelength Effects in Composite Media," *Phys. Rev. B*, vol. 26, pp. 5313-5320, 1982.
- [115] K. M. Ho, C. T. Chan, C. M. Soukoulis, R. Biswas, and M. Sigalas, "Photonic band gaps in three dimensions: new layer-by-layer periodic structures," *Solid State Commun.*, vol. 89, pp. 413-416, 1994.
- [116] H. S. Sozuer and J. P. Dowling, "Photonic band calculations for woodpile structures," *J. Mod. Optic.*, vol. 41, pp. 231-239, 1994.
- [117] F. Meseguer, A. Blanco, H. Miguez, F. Garcia-Santamaria, M. Ibisate, and C. Lopez, "Synthesis of inverse opals," *Colloid. Surface A*, vol. 202, pp. 281-290, 2002.
- [118] O. Toader and S. John, "Proposed square spiral microfabrication architecture for large three-dimensional photonic band gap crystals," *Science*, vol. 292, pp. 1133-1135, 2001.
- [119] O. Toader and S. John, "Square spiral photonic crystals: Robust architecture for microfabrication of materials with large three-dimensional photonic band gaps," *Phys. Rev. E*, vol. 66, pp. 016610, 2002.

- [120] B. Dick, J. C. Sit, M. J. Brett, I. M. N. Votte, and C. W. M. Bastiaansen, "Embossed polymeric relief structures as a template for the growth of periodic inorganic microstructures," *Nano Lett.*, vol. 1, pp. 71-73, 2001.
- [121] M. O. Jensen and M. J. Brett, "Periodically structured glancing angle deposition thin films," *IEEE Transactions on Nanotechnology*, vol. 4, pp. 269-277, 2005.
- [122] T. A. Savas, M. Farhoud, H. I. Smith, M. Hwang, and C. A. Ross, "Properties of large-area nanomagnet arrays with 100nm period made by interferometric lithography," *J. Appl. Phys.*, vol. 85, pp. 6160-6162, 1999.
- [123] I. Hodgkinson, Q. H. Wu, and J. Hazel, "Empirical equations for the principal refractive indices and column angle of obliquely deposited films of tantalum oxide, titanium oxide, and zirconium oxide," *Appl. Optics*, vol. 37, pp. 2653-2659, 1998.
- [124] M. F. Schubert, J. Q. Xi, J. K. Kim, and E. F. Schubert, "Distributed Bragg reflector consisting of high- and low-refractive-index thin film layers made of the same material," *Appl. Phys. Lett.*, vol. 90, pp. 141115, 2007.
- [125] S. L. Jones, D. Kumar, K. G. Cho, R. Singh, and P. H. Holloway, "Pulsed laser deposition of Y<sub>2</sub>O<sub>3</sub> : Eu thin film phosphors," *Displays*, vol. 19, pp. 151-167, 1999.
- [126] P. C. P. Hruday, M. Taschuk, Y. Y. Tsui, R. Fedosejevs, and M. J. Brett, "Effects of film structure on photoluminescence emission properties of nanostructured Y<sub>2</sub>O<sub>3</sub>:Eu thin films," presented at Nanophotonic Materials, Denver, CO, 2004.
- [127] G. Blasse and B. C. Grabmaier, *Luminescent materials*. Berlin ; New York: Springer-Verlag, 1994.
- [128] S. M. Pursel, M. W. Horn, and A. Lakhtakia, "Blue-shifting of circular Bragg phenomenon by annealing of chiral sculptured thin films," *Opt. Express.*, vol. 14, pp. 8001-8012, 2006.
- [129] T. Igarashi, M. Ihara, T. Kusunoki, K. Ohno, T. Isobe, and M. Senna, "Relationship between optical properties and crystallinity of nanometer Y<sub>2</sub>O<sub>3</sub> : Eu phosphor," *Appl. Phys. Lett.*, vol. 76, pp. 1549-1551, 2000.



## Appendices

### ***Appendix 1 – Maple Calculation for an Anisotropic Film Layer***

The following is a Maple calculation given as an example to the theory presented in §1.4 and 1.5, which applies a solution to the Bruggeman EMA for a GLAD film and then calculates the Mueller matrices for the system using Berreman's method.

```
> restart:
> with(plots):
Warning, the name changecoords has been redefined
> with(linalg):
Warning, the protected names norm and trace have been redefined and
unprotected
Enter the density of the layer
> rho:=24.24 /100:
Enter the thickness of the layer in nanometers
> d:=184.091:
Enter the depolarization factor for principal index along the posts, qz
> q[3]:=0.04028:
Enter the depolarization split factor between x and y
> xy_split:=0.49157:
Enter the Euler angle Phi
> phi:=0 *Pi/180:
Enter the Euler angle Theta
> theta:=0 *Pi/180:
Enter the Euler angle Psi
> psi:= 0:
Enter the light angle of incidence
> Pa:=60 *Pi/180:
Enter the Wavelength array to be used
> lambda:=ImportVector("H:\\Calculations\\Mueller Matrix
Biaxial Film Isotrop Substrate\\Wavelength Array 10
nm.txt",transpose=true):
Enter the film material dielectric constant array (no absorption material)
> e_mat:=ImportVector("H:\\Calculations\\Mueller Matrix
Biaxial Film Isotrop Substrate\\SiO2 epsilon Array 10
nm.txt",transpose=true):
Enter the index of refraction for substrate
```

```

> n_Si:=ImportVector("H:\\Calculations\\Mueller Matrix
Biaxial Film Isotrop Substrate\\Si n Array 10
nm.txt",transpose=true):
Enter the extinction coefficient array for the substrate
> k_Si:=ImportVector("H:\\Calculations\\Mueller Matrix
Biaxial Film Isotrop Substrate\\Si k Array 10
nm.txt",transpose=true):
> a:=vectdim(convert(lambda, 'array')):
Calculation for the x-depolarization factor, qx
> q[1]:=(1-q[3])*xy_split:
Calculation for the y-depolarization factor, qy
> q[2]:=1-q[3]-q[1]:
And we define the dielectric constant of ambient, which is air (epsilon_a = na =
1)
> e_void:=1:
We must first compute the dielectric tensor for my film, we must start with the
rotation in Euler angle Phi
> P:=matrix(3,3,[cos(phi),sin(phi),0, -sin(phi),cos(phi),0,
0,0,1]):
And now the rotation in Theta
> Q:=matrix(3,3,[1,0,0, 0,cos(theta),sin(theta), 0,-
sin(theta),cos(theta)]):
And finally, psi
> R:=matrix(3,3,[cos(psi),sin(psi),0, -sin(psi),cos(psi),0,
0,0,1]):
Finally, we have the general rotation matrix that can be applied to our dielectric
tensor (see Goldstein Classical Mechanics, 1980)
> A:=multiply(P,Q,R):
We now define arrays for the Mueller matrix elements
> M12:=[]:
> M13:=[]:
> M14:=[]:
> M21:=[]:
> M22:=[]:
> M23:=[]:
> M24:=[]:
> M31:=[]:
> M32:=[]:
> M33:=[]:
> M34:=[]:
Here is where we must start the For-Loop Process, starting with the Bruggeman
EMA for the indices
> for i from 1 to a do
>   for j from 1 to 3 do

```

```

> e[j][i]:=1/2/(-1+q[j])*(-
rho*e_mat[i]+e_void*q[j]+e_mat[i]*q[j]-e_void+rho*e_void-
sqrt(-2*rho^2*e_mat[i]*e_void+ 2*rho*e_mat[i]*e_void+
rho^2*(e_mat[i])^2+e_void^2- 2*rho*e_void^2+
rho^2*e_void^2+2*e_void^2*q[j]*rho-
2*e_void*q[j]^2*e_mat[i]- 2*rho*(e_mat[i])^2*q[j]+
2*e_mat[i]*e_void*q[j]+(e_mat[i])^2*q[j]^2-
2*e_void^2*q[j]+e_void^2*q[j]^2)):

```

```
> od:
```

```
> ex[i]:=e[1][i]:
```

```
> ey[i]:=e[2][i]:
```

```
> ez[i]:=e[3][i]:
```

We now define the principal axes of the dielectric function

```
> e0[i]:=matrix(3,3,[ex[i],0,0, 0,ey[i],0, 0,0,ez[i]]):
```

And we can now apply a general rotation in the dielectric tensor (eg. tilted columns)

```
> epsilon[i]:=multiply(A,e0[i],inverse(A)):
```

Now we must compute the matrix Delta (eq. 13 from Schubert), we start by getting kx using the ambient index e\_void and the angle of incidence P

```
> kx:=e_void*sin(Pa):
```

Now we compute the matrix Delta, which we will need later to get the Transfer matrix for this layer

```

> Delta[i]:=matrix(4,4,[-kx*epsilon[i][3,1]/epsilon[i][3,3],
-kx*epsilon[i][3,2]/epsilon[i][3,3], 0, 1-
kx^2/epsilon[i][3,3], 0, 0, -1, 0,
epsilon[i][2,3]*epsilon[i][3,1]/epsilon[i][3,3]-
epsilon[i][2,1], kx^2-
epsilon[i][2,2]+epsilon[i][2,3]*epsilon[i][3,2]/epsilon[i][
3,3], 0, kx*epsilon[i][2,3]/epsilon[i][3,3],
epsilon[i][1,1]-
epsilon[i][1,3]*epsilon[i][3,1]/epsilon[i][3,3],
epsilon[i][1,2]-
epsilon[i][1,3]*epsilon[i][3,2]/epsilon[i][3,3], 0, -
kx*epsilon[i][1,3]/epsilon[i][3,3]]):

```

In order to do get the Partial Transfer Matrix for the film, we need to solve the eigenvalues for Delta

```
> r[i]:=array([eigenvalues(Delta[i])]):
```

Now we must compute the Beta terms so that we use the Cayley-Hamilton expansion to get the Partial Transfer matrix for the film

```

>
eqns[i]:={exp(2*Pi*r[i][1]*d*I/lambda[i])=sum(x[k][i]*r[i][
1]^(k-1),k=1..4),
exp(2*Pi*r[i][2]*d*I/lambda[i])=sum(x[k][i]*r[i][2]^(k-
1),k=1..4),
exp(2*Pi*r[i][3]*d*I/lambda[i])=sum(x[k][i]*r[i][3]^(k-
1),k=1..4),

```

```
exp(2*Pi*r[i][4]*d*I/lambda[i])=sum(x[k][i]*r[i][4]^(k-1),k=1..4)}:
```

```
> sols[i]:=solve(eqns[i]):
```

And now, using the solutions, we can get the necessary Beta terms

```
> beta_1[i]:=subs(sols[i], x[1][i]):
```

```
> beta_2[i]:=subs(sols[i], x[2][i]):
```

```
> beta_3[i]:=subs(sols[i], x[3][i]):
```

```
> beta_4[i]:=subs(sols[i], x[4][i]):
```

```
> E:=Matrix(4,4,shape=identity):
```

Which allow us to compute the Film Partial Transfer Matrix, Tp

```
> Tp[i]:=evalm(beta_1[i]*E + beta_2[i]*Delta[i] +
beta_3[i]*(Delta[i])^2 + beta_4[i]*(Delta[i])^3):
```

Now we must enter the equations for the air (ambient) and substrate matrices, La\_inv and Lf respectively. We first need to define the angle Pf for the substrate angle of light entry, using the ambient index and the substrate complex index

```
> nf[i]:=n_Si[i] - I*k_Si[i]:
```

```
> Pf[i]:=arccos(sqrt(1-((e_void/nf[i])*sin(Pa))^2)):
```

Now we can obtain the partial matrix corresponding to air (ambient), La\_inv

```
> La_inv:=0.5*matrix(4,4, [0,1,-1/(e_void*cos(Pa)),0,
0,1,1/(e_void*cos(Pa)),0, 1/cos(Pa),0,0,1/e_void, -
1/cos(Pa),0,0,1/e_void]):
```

And we also define the substrate partial matrix, Lf

```
> Lf[i]:=matrix(4,4, [0,0,cos(Pf[i]),0, 1,0,0,0, -
nf[i]*cos(Pf[i]),0,0,0, 0,0,nf[i],0]):
```

Finally, we can now compute the Transfer matrix for the air-film-substrate medium:

```
> T[i]:=scalarmul(multiply(La_inv,Tp[i],Lf[i]),-d):
```

Now, we must obtain from this the Jones reflection coefficients from the Transfer matrix, T

```
> Rss[i]:=(T[i][2,1]*T[i][3,3]-
T[i][2,3]*T[i][3,1])/(T[i][3,3]*T[i][1,1]-
T[i][1,3]*T[i][3,1]):
```

```
> Rpp[i]:=(T[i][4,1]*T[i][1,3]-
T[i][1,1]*T[i][4,3])/(T[i][1,3]*T[i][3,1]-
T[i][3,3]*T[i][1,1]):
```

```
> Rps[i]:=(T[i][2,1]*T[i][1,3]-
T[i][2,3]*T[i][1,1])/(T[i][1,3]*T[i][3,1]-
T[i][3,3]*T[i][1,1]):
```

```
> Rsp[i]:=(T[i][4,1]*T[i][3,3]-
T[i][3,1]*T[i][4,3])/(T[i][1,1]*T[i][3,3]-
T[i][1,3]*T[i][3,1]):
```

Thus the Jones reflection matrix is

```
> J[i]:=evalf(matrix(2,2, [Rpp[i],Rps[i],Rsp[i],Rss[i]])):
```

Now in order to get the Mueller matrix of this Jones matrix, we must first define one necessary matrix B (used as a conversion matrix), see Jellison, Thin Solid Films 313-314 (1998) 33-39

```

> B:=matrix(4,4,[1,0,0,1, 1,0,0,-1, 0,1,1,0, 0,I,-I,0]):
And now we must take the conjugate transpose of the Jones matrix
> K[i]:=htranspose(J[i]):
Compute the Direct (Kronecker) Product of Jones matrix and its adjoint
>
L[i]:=matrix(4,4,[J[i][1,1]*K[i][1,1],J[i][1,1]*K[i][1,2],J
[i][1,2]*K[i][1,1],J[i][1,2]*K[i][1,2],
J[i][1,1]*K[i][2,1],J[i][1,1]*K[i][2,2],J[i][1,2]*K[i][2,1]
,J[i][1,2]*K[i][2,2],
J[i][2,1]*K[i][1,1],J[i][2,1]*K[i][1,2],J[i][2,2]*K[i][1,1]
,J[i][2,2]*K[i][1,2],
J[i][2,1]*K[i][2,1],J[i][2,1]*K[i][2,2],J[i][2,2]*K[i][2,1]
,J[i][2,2]*K[i][2,2]]):
Now, we finally obtain the Mueller matrix, M, using the previous matrices:
> m[i]:=simplify(multiply(B,L[i],inverse(B))):
> M[i]:=scalarmul(m[i],1/m[i][1,1]):
> M12:=[op(M12),M[i][1,2]]:
> M13:=[op(M13),M[i][1,3]]:
> M14:=[op(M14),M[i][1,4]]:
> M21:=[op(M21),M[i][2,1]]:
> M22:=[op(M22),M[i][2,2]]:
> M23:=[op(M23),M[i][2,3]]:
> M24:=[op(M24),M[i][2,4]]:
> M31:=[op(M31),M[i][3,1]]:
> M32:=[op(M32),M[i][3,2]]:
> M33:=[op(M33),M[i][3,3]]:
> M34:=[op(M34),M[i][3,4]]:
> od:
> lambda_convert:=convert(lambda,'list'):
We now import experimental data to compare to
> M12_points:={lambda_convert,M12}:
> M12_pair:=(lambda_convert,M12)-
> [eval(lambda_convert),M12]:
> M12_zip:=zip(M12_pair,lambda_convert,M12):
> M13_points:={lambda_convert,M13}:
> M13_pair:=(lambda_convert,M13)-
> [eval(lambda_convert),M13]:
> M13_zip:=zip(M13_pair,lambda_convert,M13):
> M14_points:={lambda_convert,M14}:
> M14_pair:=(lambda_convert,M14)-
> [eval(lambda_convert),M14]:
> M14_zip:=zip(M14_pair,lambda_convert,M14):
> M21_points:={lambda_convert,M21}:
> M21_pair:=(lambda_convert,M21)-
> [eval(lambda_convert),M21]:

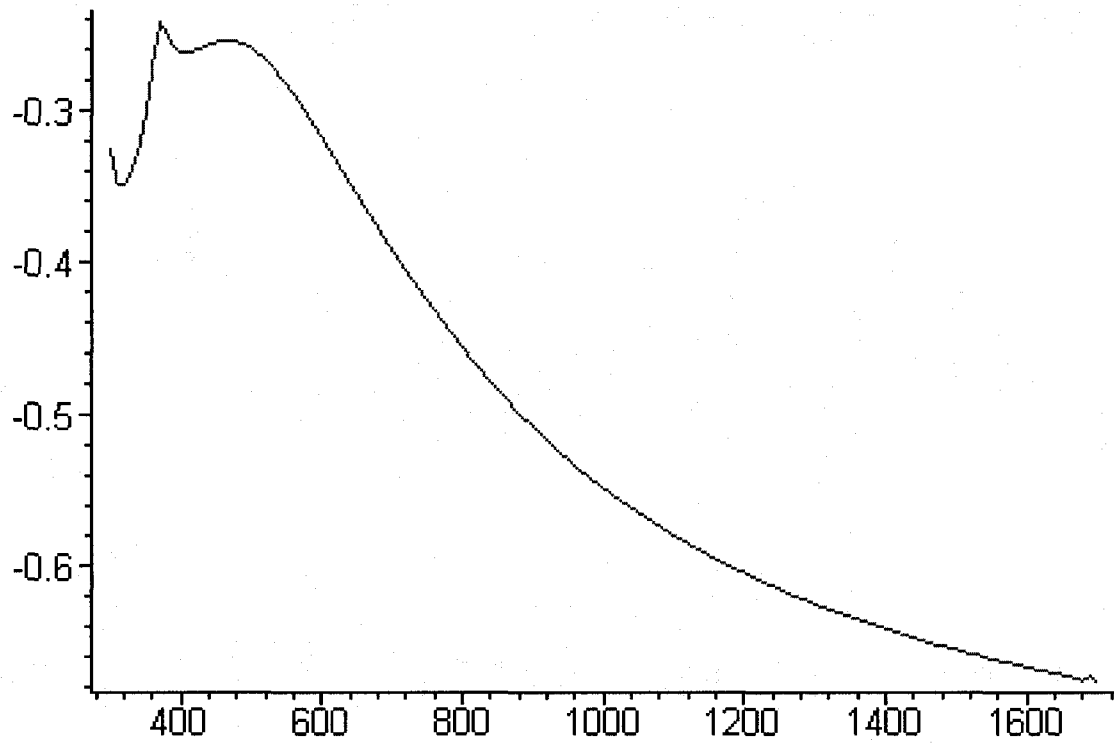
```

```

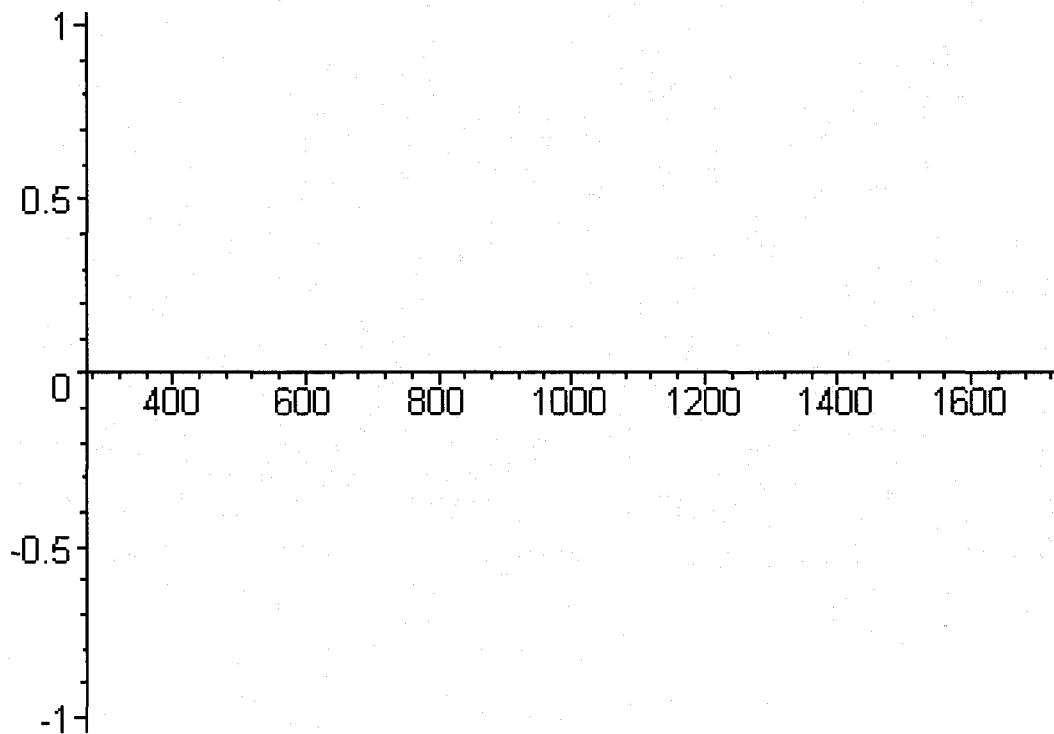
> M21_zip:=zip(M21_pair,lambda_convert,M21):
> M22_points:={lambda_convert,M22}:
> M22_pair:=(lambda_convert,M22)-
> [eval(lambda_convert),M22]:
> M22_zip:=zip(M22_pair,lambda_convert,M22):
> M23_points:={lambda_convert,M23}:
> M23_pair:=(lambda_convert,M23)-
> [eval(lambda_convert),M23]:
> M23_zip:=zip(M23_pair,lambda_convert,M23):
> M24_points:={lambda_convert,M24}:
> M24_pair:=(lambda_convert,M24)-
> [eval(lambda_convert),M24]:
> M24_zip:=zip(M24_pair,lambda_convert,M24):
> M31_points:={lambda_convert,M31}:
> M31_pair:=(lambda_convert,M31)-
> [eval(lambda_convert),M31]:
> M31_zip:=zip(M31_pair,lambda_convert,M31):
> M32_points:={lambda_convert,M32}:
> M32_pair:=(lambda_convert,M32)-
> [eval(lambda_convert),M32]:
> M32_zip:=zip(M32_pair,lambda_convert,M32):
> M33_points:={lambda_convert,M33}:
> M33_pair:=(lambda_convert,M33)-
> [eval(lambda_convert),M33]:
> M33_zip:=zip(M33_pair,lambda_convert,M33):
> M34_points:={lambda_convert,M34}:
> M34_pair:=(lambda_convert,M34)-
> [eval(lambda_convert),M34]:
> M34_zip:=zip(M34_pair,lambda_convert,M34):
We now plot the theoretical curves generated above as a function of wavelength
> plot(M12_zip,title="M12 vs. Wavelength");

```

M12 vs. Wavelength

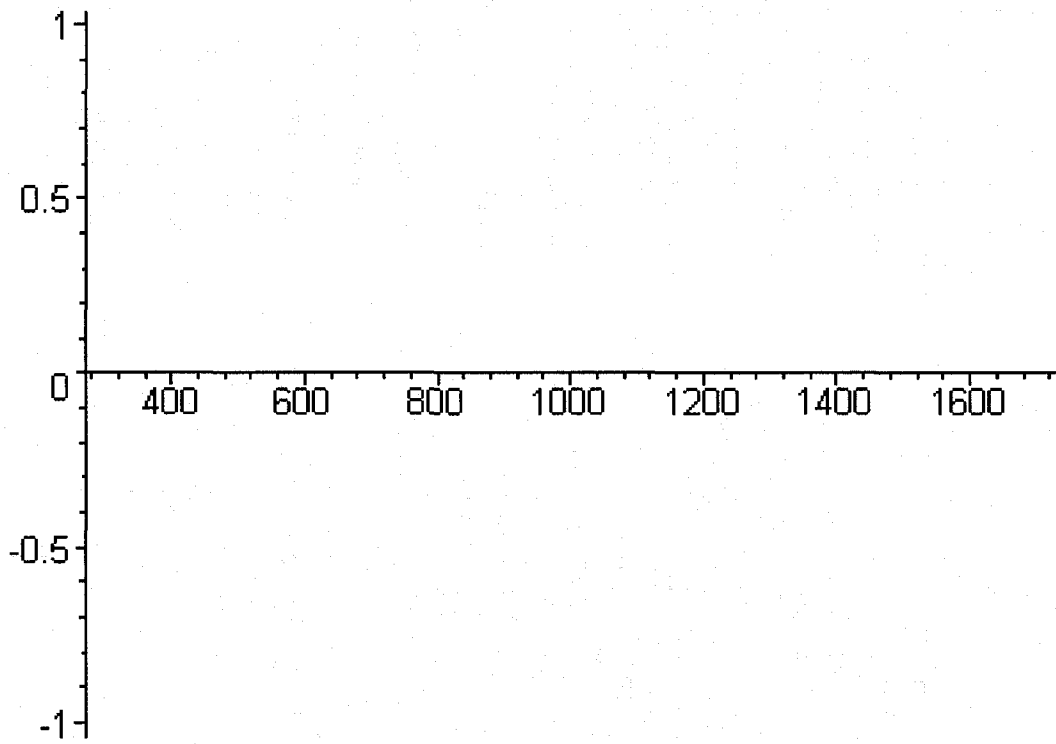


```
> plot(M13_zip, title="M13 vs. Wavelength");  
M13 vs. Wavelength
```



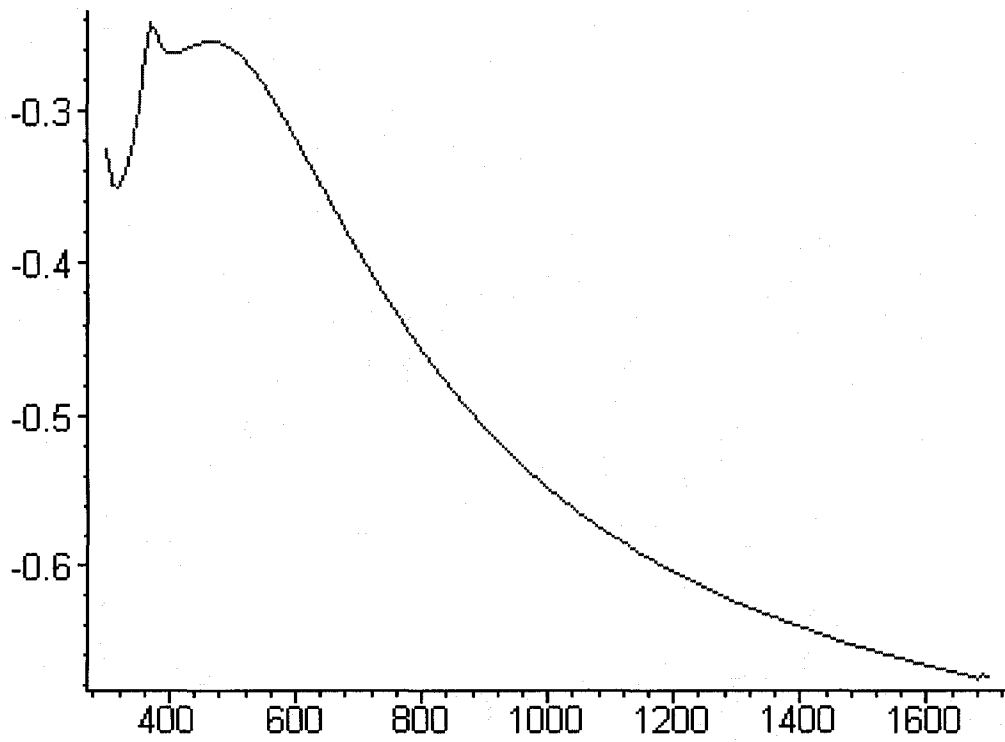
```
> plot(M14_zip, title="M14 vs. Wavelength", title="M14 vs.  
Wavelength(nm)");
```

M14 vs. Wavelength(nm)



```
> plot(M21_zip, title="M21 vs. Wavelength", title="M21 vs. Wavelength(nm)");
```

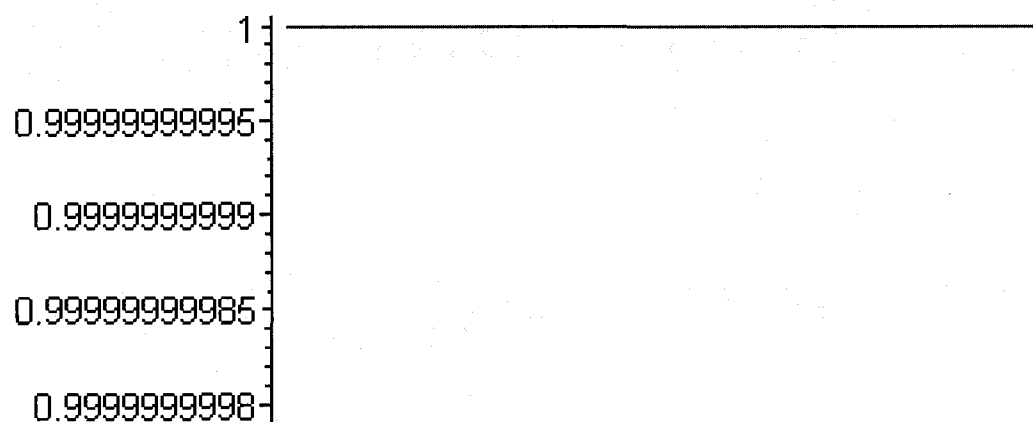
M21 vs. Wavelength(nm)





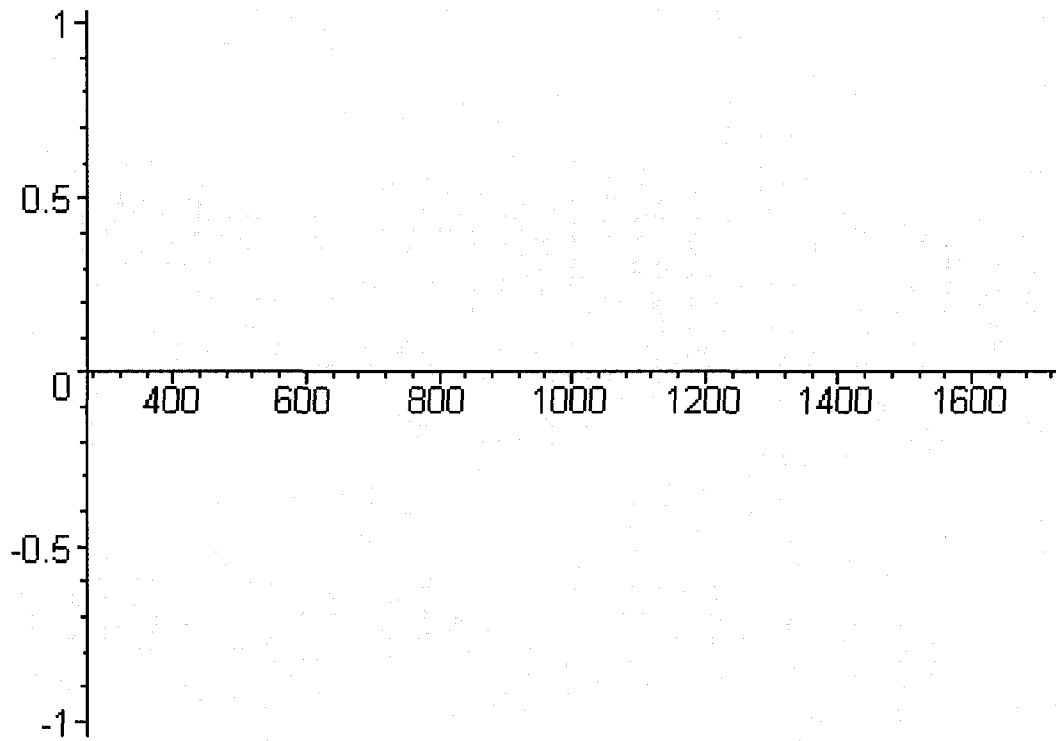
```
> plot(M22_zip, title="M22 vs. Wavelength", title="M22 vs.  
Wavelength(nm)");
```

M22 vs. Wavelength(nm)



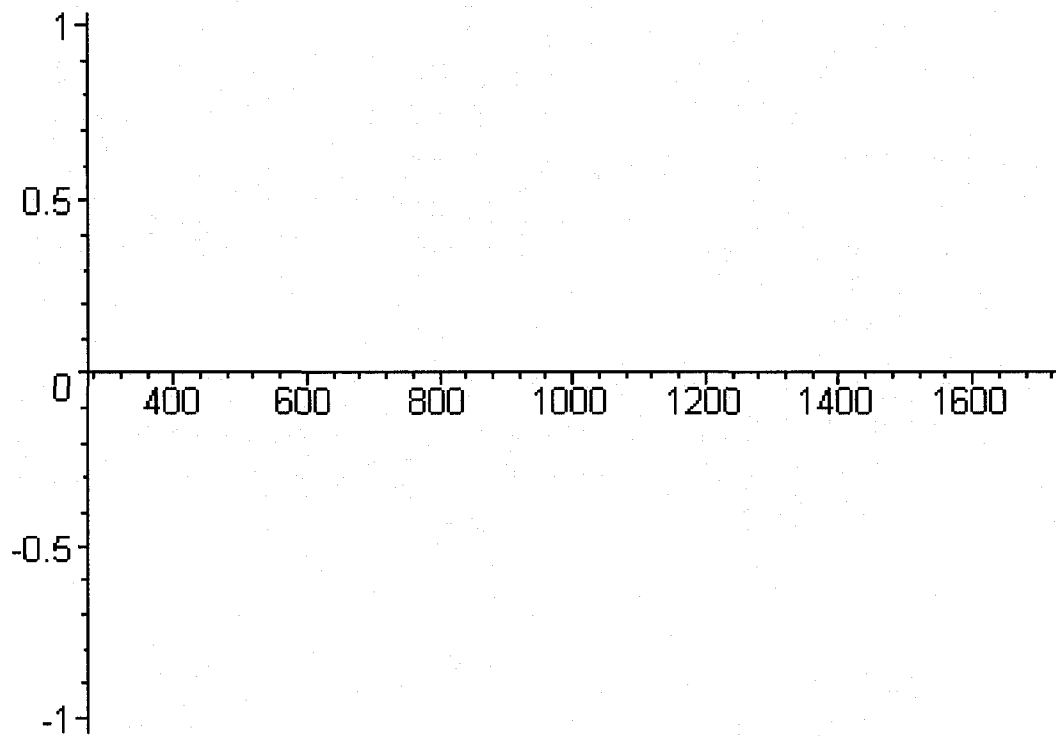
```
> plot(M23_zip, title="M23 vs. Wavelength", title="M23 vs.  
Wavelength(nm)");
```

M23 vs. Wavelength(nm)

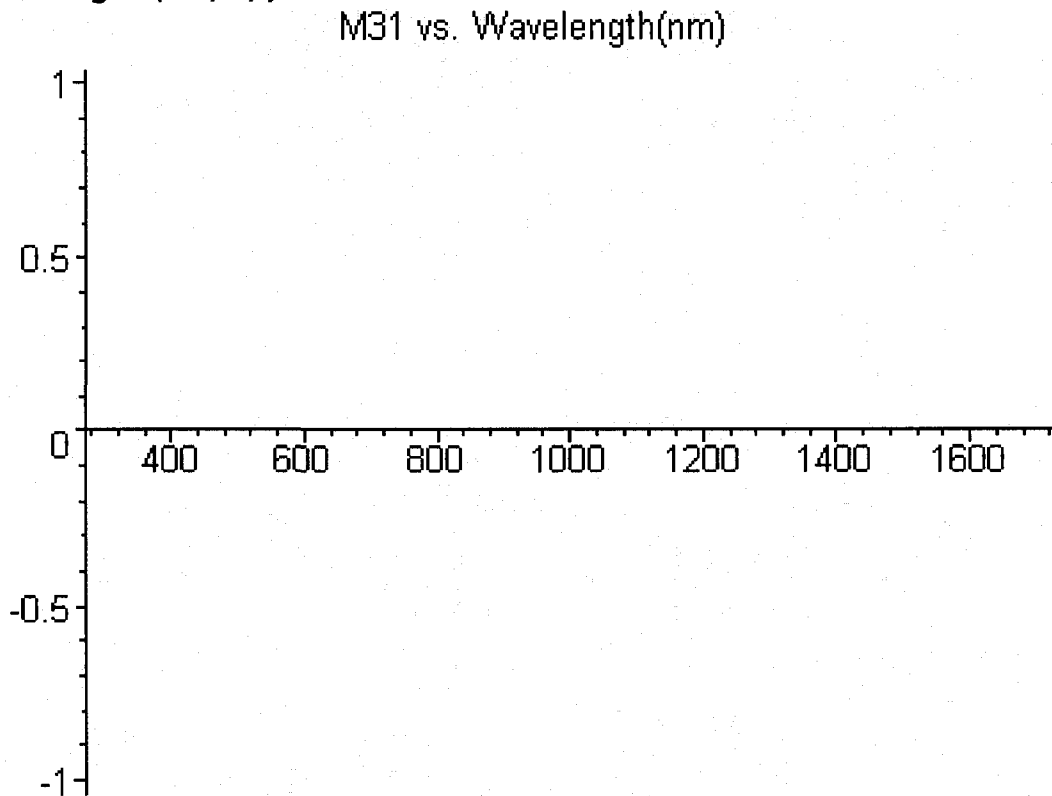


```
> plot(M24_zip, title="M24 vs. Wavelength", title="M24 vs.  
Wavelength(nm)");
```

M24 vs. Wavelength(nm)

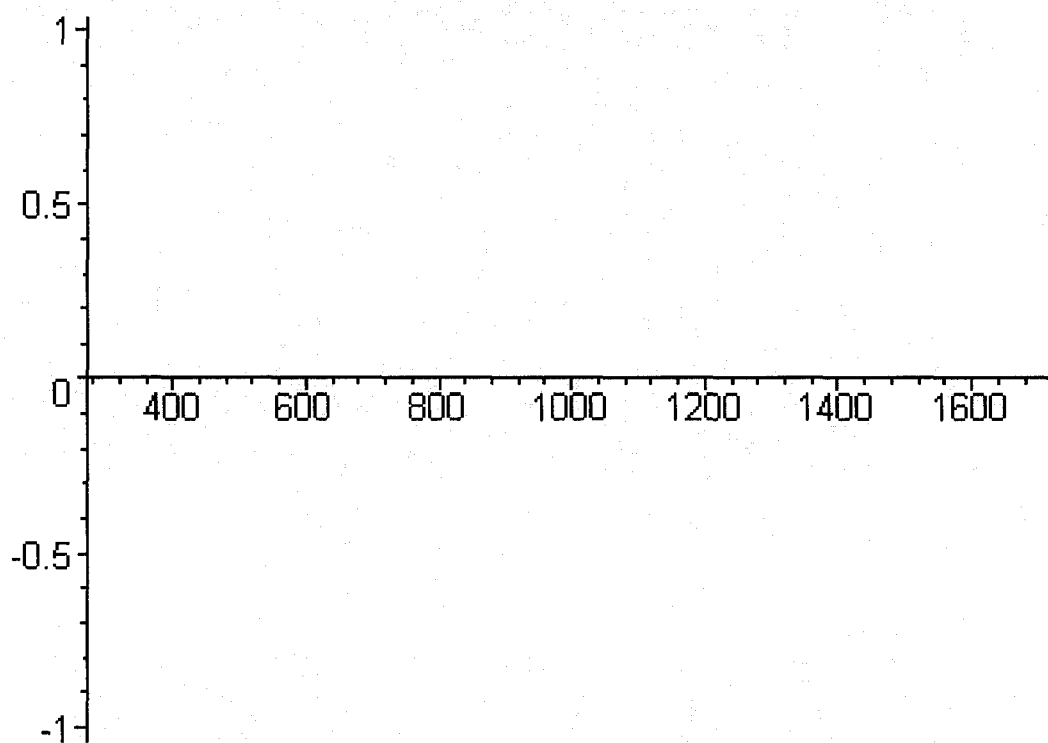


```
> plot(M31_zip, title="M31 vs. Wavelength", title="M31 vs.  
Wavelength(nm)");
```



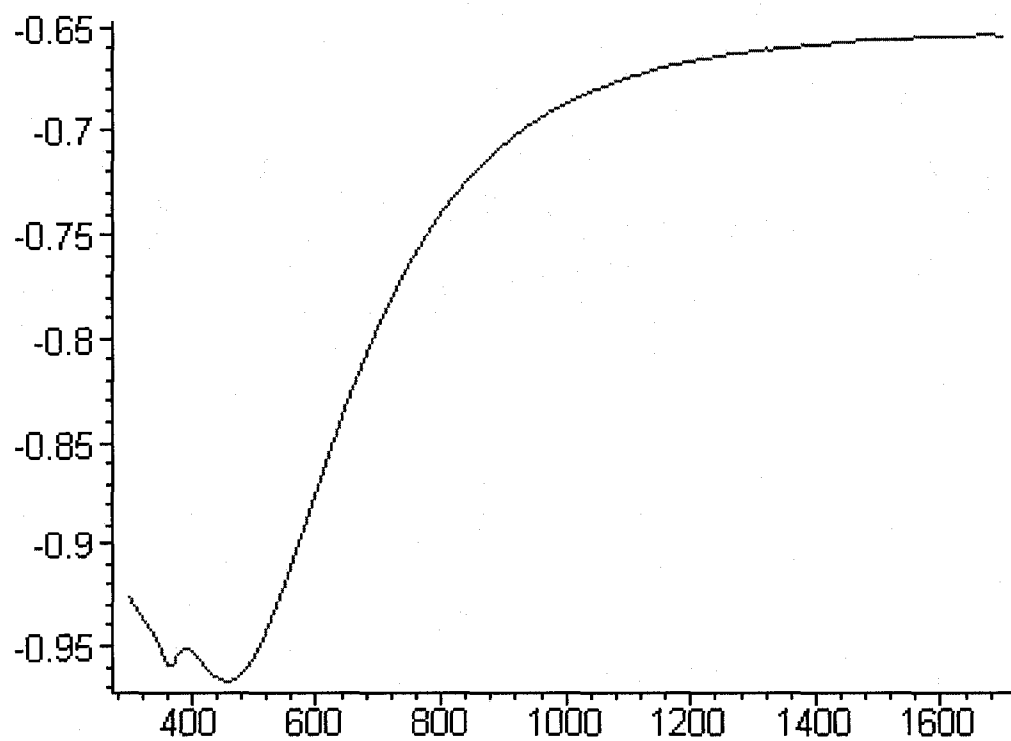
```
> plot(M32_zip, title="M32 vs. Wavelength", title="M32 vs.  
Wavelength(nm)");
```

M32 vs. Wavelength(nm)

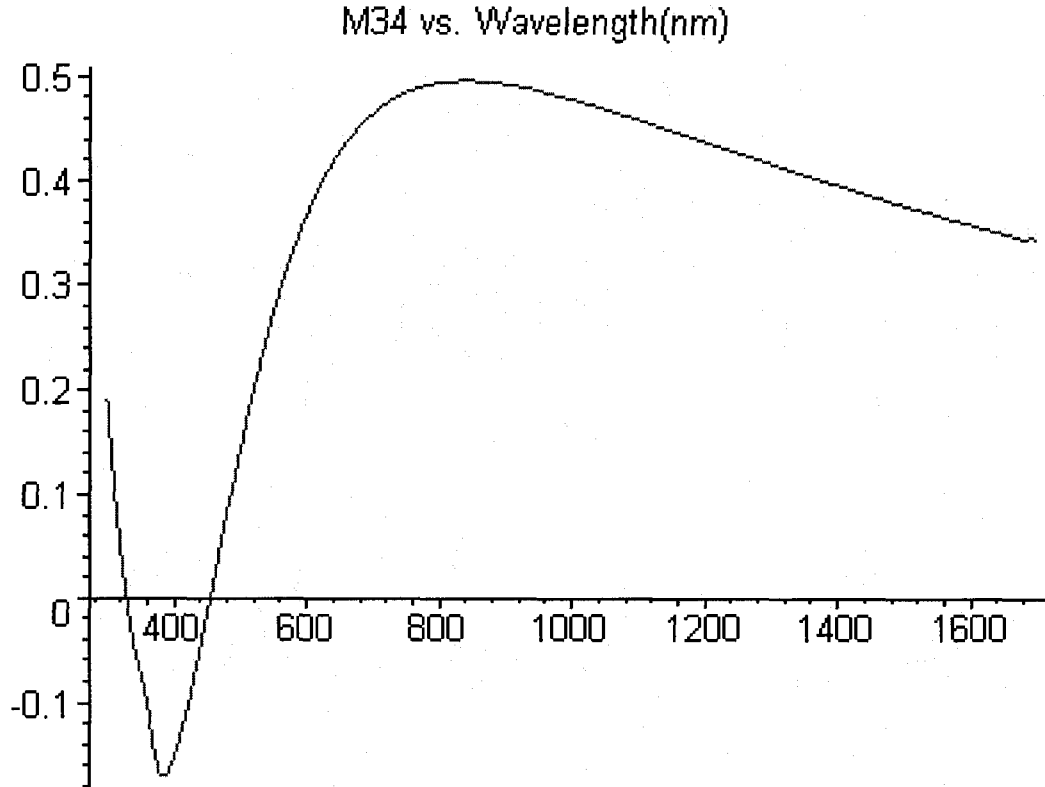


```
> plot(M33_zip,title="M33 vs. Wavelength",title="M33 vs. Wavelength(nm)");
```

M33 vs. Wavelength(nm)



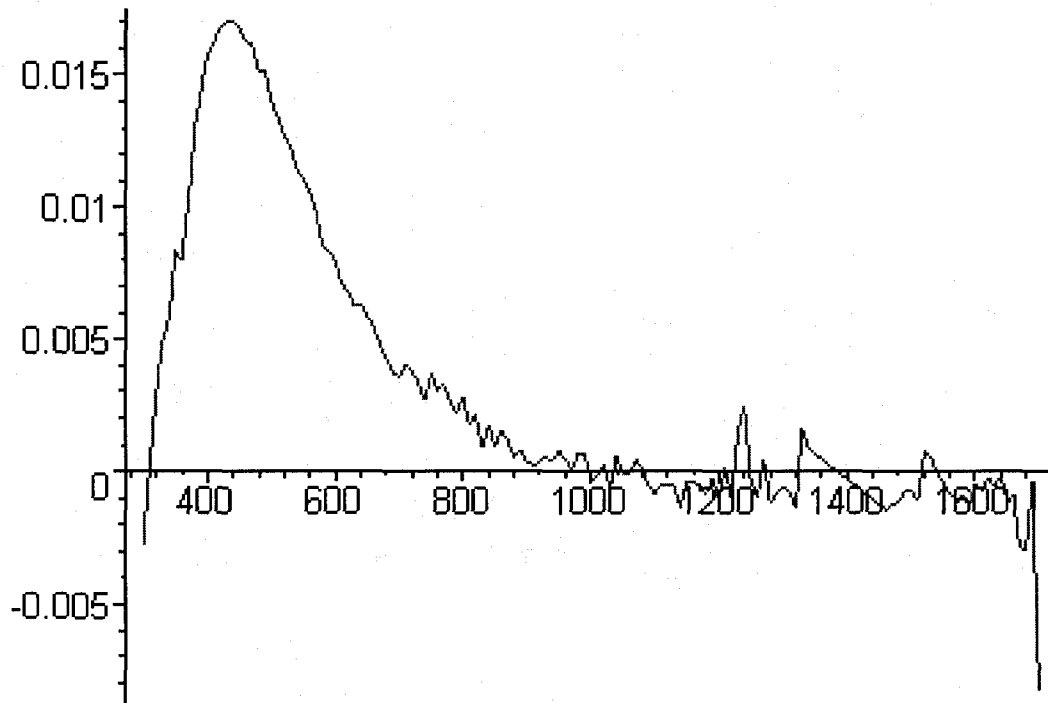
```
> plot(M34_zip,title="M34 vs. Wavelength",title="M34 vs.
Wavelength(nm)");
```



```
> M12_expt:=ImportVector("H:\\Calculations\\Mueller Matrix
Biaxial Film Isotrop Substrate\\Multilayer FFT BEMA
Corrections\\Raw Data\\20050623-1 M12 60
deg.txt",transpose=true):
> M21_expt:=ImportVector("H:\\Calculations\\Mueller Matrix
Biaxial Film Isotrop Substrate\\Multilayer FFT BEMA
Corrections\\Raw Data\\20050623-1 M21 60
deg.txt",transpose=true):
> M33_expt:=ImportVector("H:\\Calculations\\Mueller Matrix
Biaxial Film Isotrop Substrate\\Multilayer FFT BEMA
Corrections\\Raw Data\\20050623-1 M33 60
deg.txt",transpose=true):
> M34_expt:=ImportVector("H:\\Calculations\\Mueller Matrix
Biaxial Film Isotrop Substrate\\Multilayer FFT BEMA
Corrections\\Raw Data\\20050623-1 M34 60
deg.txt",transpose=true):
> M12_expt_convert:=convert(M12_expt,'list'):
> M12_diff:=M12-M12_expt_convert:
> M12_diff_points:={lambda_convert,M12_diff}:
> M12_diff_pair:=(lambda_convert,M12_diff)-
> [lambda_convert,M12_diff]:
> M12_diff_zip:=zip(M12_diff_pair,lambda_convert,M12_diff):
```

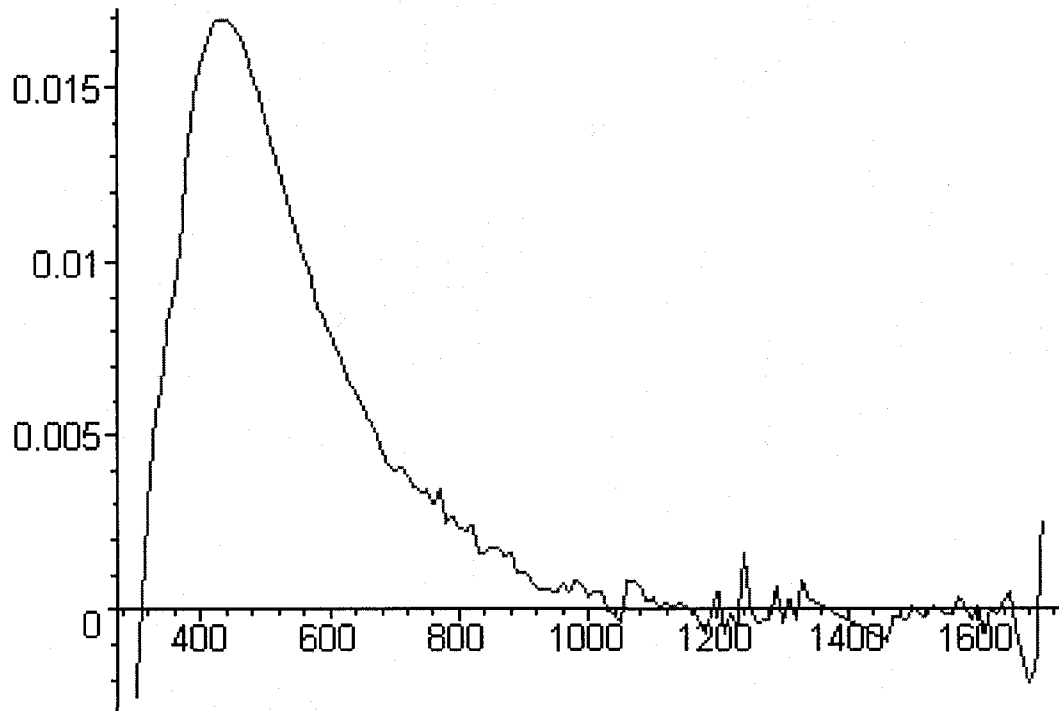
We now plot the differences between the theoretical and experimental curves  
> plot(M12\_diff\_zip,title="M12 expt. theory difference vs.  
Wavelength");

M12 expt. theory difference vs. Wavelength



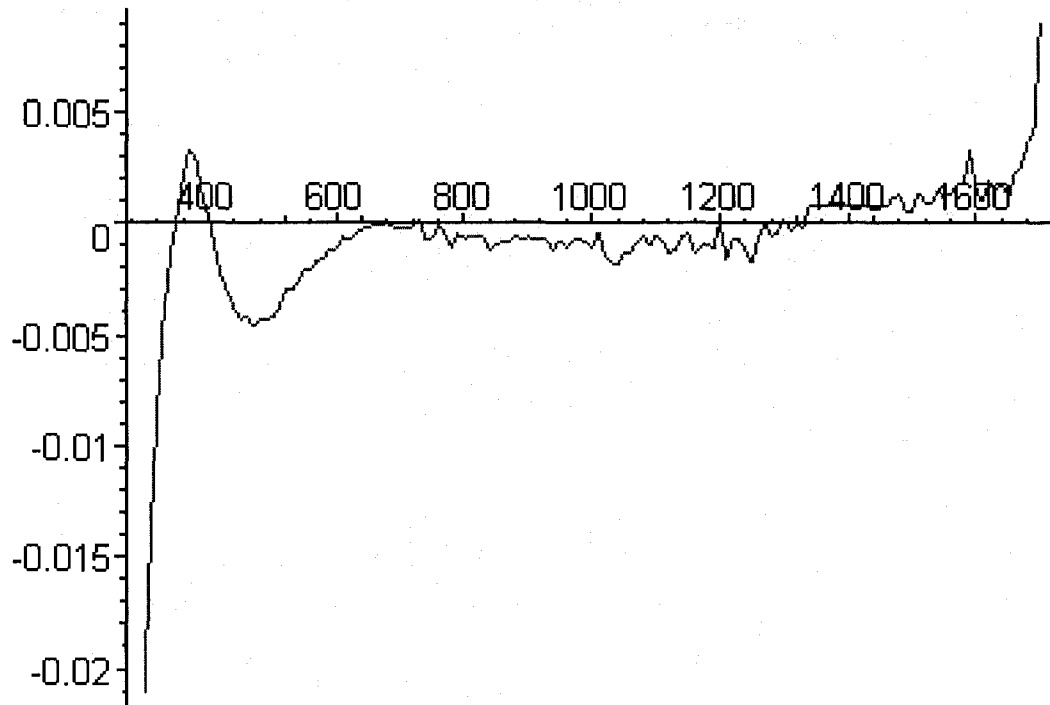
```
> M21_expt_convert:=convert(M21_expt,'list');
> M21_diff:=M21-M21_expt_convert:
> M21_diff_points:={lambda_convert,M21_diff}:
> M21_diff_pair:=(lambda_convert,M21_diff)-
> [lambda_convert,M21_diff]:
> M21_diff_zip:=zip(M21_diff_pair,lambda_convert,M21_diff):
> plot(M21_diff_zip,title="M21 expt. theory difference vs.
Wavelength");
```

M21 expt. theory difference vs. Wavelength



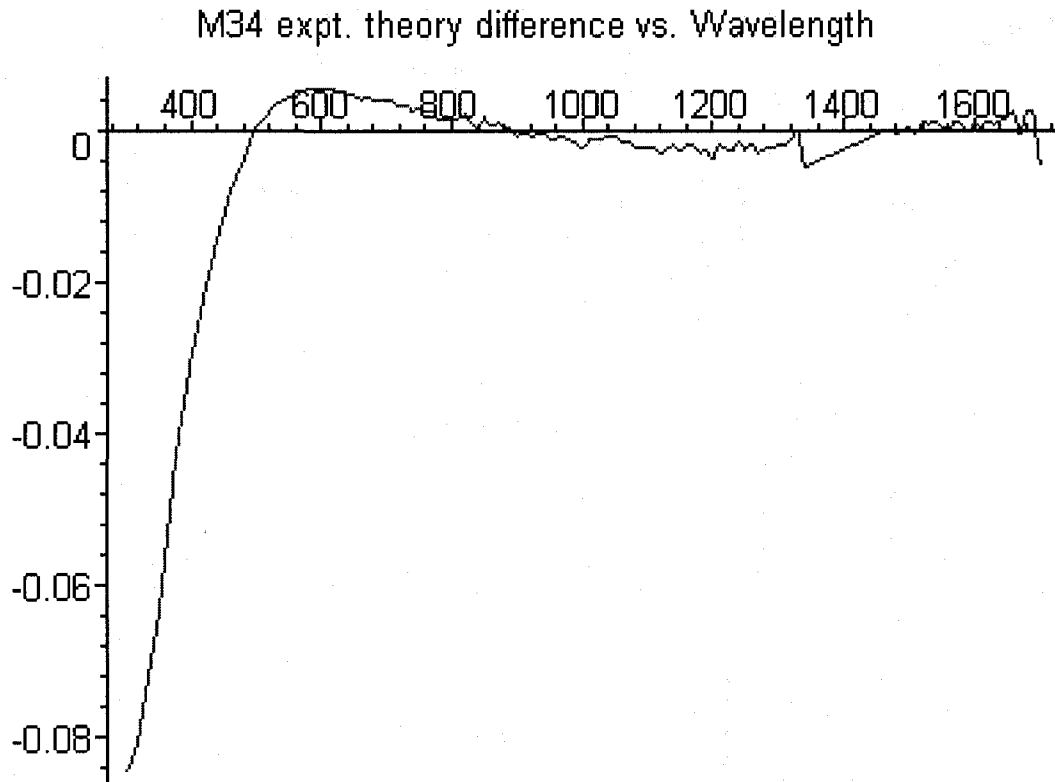
```
> M33_expt_convert:=convert(M33_expt,'list'):
> M33_diff:=M33-M33_expt_convert:
> M33_diff_points:={lambda_convert,M33_diff}:
> M33_diff_pair:=(lambda_convert,M33_diff)-
> [lambda_convert,M33_diff]:
> M33_diff_zip:=zip(M33_diff_pair,lambda_convert,M33_diff):
> plot(M33_diff_zip,title="M33 expt. theory difference vs.
Wavelength");
```

M33 expt. theory difference vs. Wavelength



```
> M34_expt_convert:=convert(M34_expt,'list'):
> M34_diff:=M34-M34_expt_convert:
> M34_diff_points:={lambda_convert,M34_diff}:
> M34_diff_pair:=(lambda_convert,M34_diff)-
> [lambda_convert,M34_diff]:
> M34_diff_zip:=zip(M34_diff_pair,lambda_convert,M34_diff):
> plot(M34_diff_zip,title="M34 expt. theory difference vs.
Wavelength");
```





And calculate the total percent difference between the theoretical and experimental curves for the non-zero elements

```
> (sum('abs(M12_diff[i])/abs(M12_expt_convert[i])', 'i'=1..a)
+ sum('abs(M21_diff[i])/abs(M21_expt_convert[i])', 'i'=1..a)
+ sum('abs(M33_diff[i])/abs(M33_expt_convert[i])', 'i'=1..a)
+
sum('abs(M34_diff[i])/abs(M34_expt_convert[i])', 'i'=1..a))/
(4*a);
.04685730120
```

## ***Appendix 2 – Kramers-Kronig Analysis for a Lorentz Oscillator***

The following calculation demonstrates the Kramers-Kronig consistency for a Lorentz Oscillator using Maple, as discussed in §1.6:

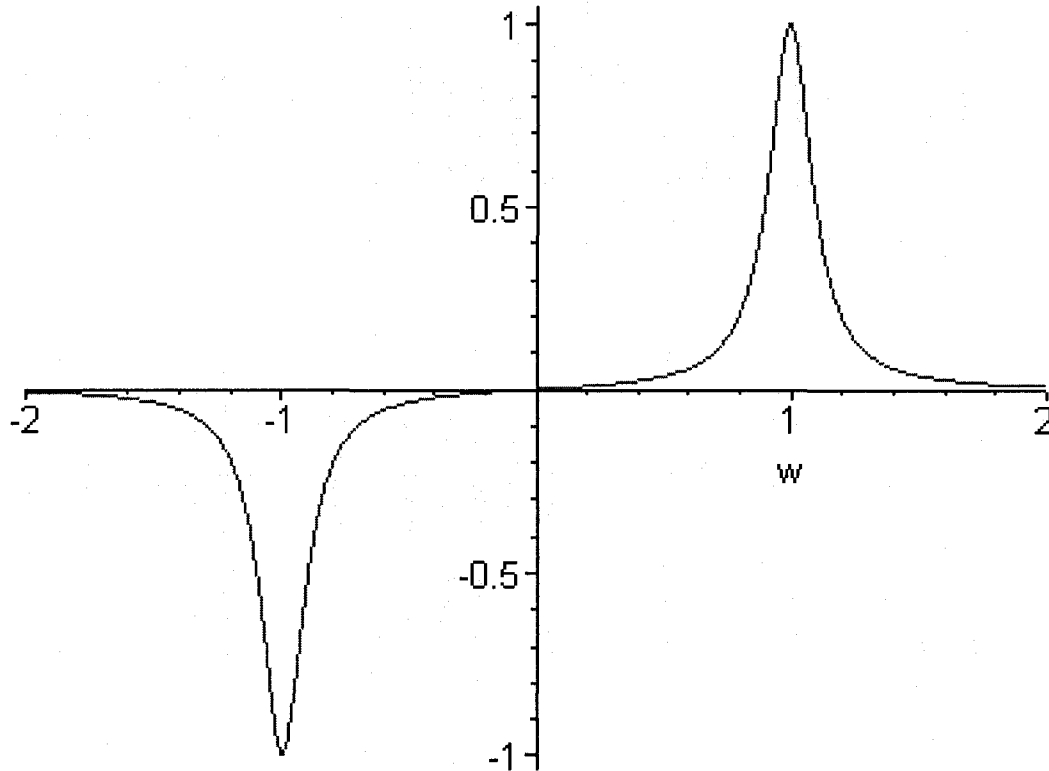
First I will compute the predicted value for Chi double prime by using the Kramers-Kronig Relations, by plugging our Chi prime into the integral. Note here that I have labelled x as w prime as in the notes, and solved for w, using Maple's Cauchy Principal Value scheme, so using a polar distance of 0.0001 was unnecessary, and I have plugged in the appropriate values for w0 and Gamma.

```
> Chi2:=(1/Pi)*int((1-x^2)/(5*((1-x^2)^2)+4*0.01*x^2)*(w-x),x=-infinity..infinity,'CauchyPrincipalValue');
```

$$\text{Chi2} := 3.141592654 \frac{w}{\pi(-49.w^2 + 25.w^4 + 25.)}$$

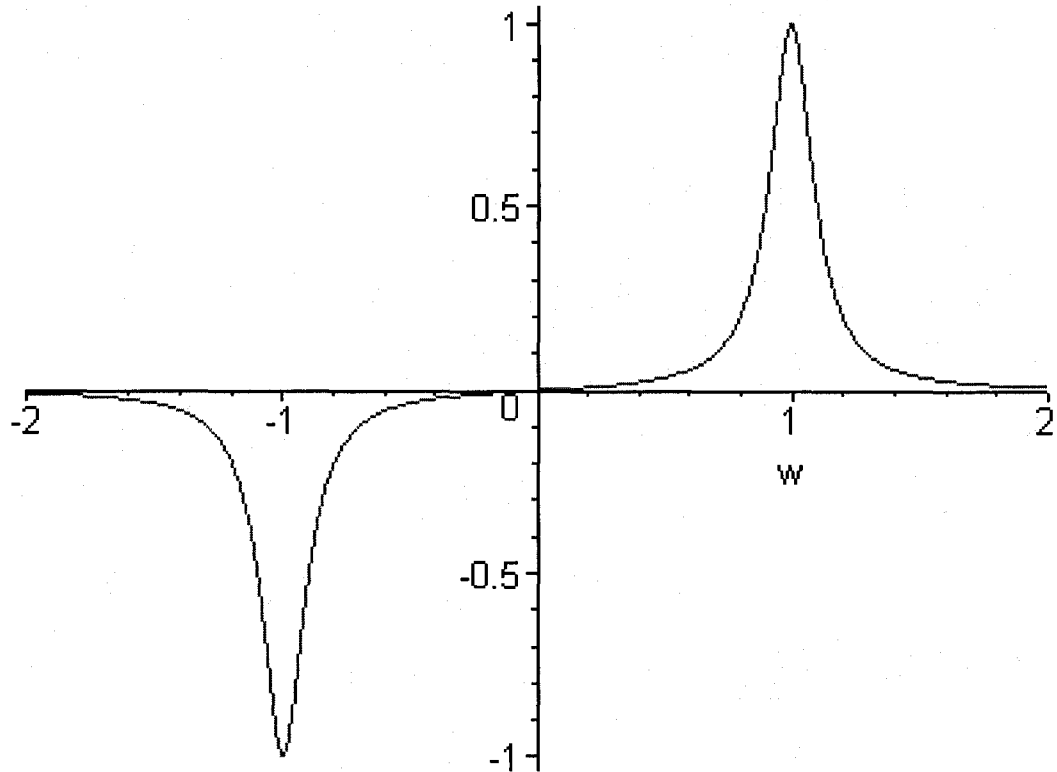
Now, I will plot the result from w=-2 to 2 rad/s

```
> plot(Chi2,w=-2..2);
```



Now let us compare this result by plotting the actual value for Chi double prime.

```
> plot(0.2*w/(5*((1-w^2)^2)+4*0.01*w^2),w=-2..2);
```



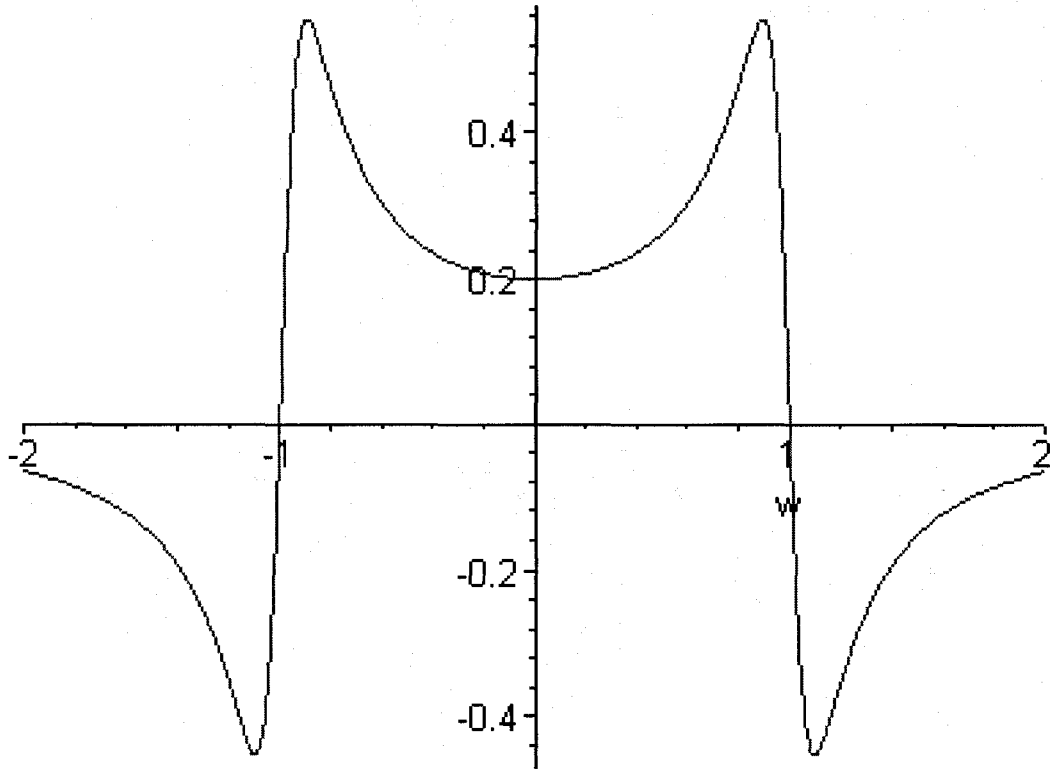
Similarly, let's compute using Kramers-Kronig, the value for Chi prime, by plugging the known Chi double prime into the relation.

```
> Chi1:=(-1/(5*Pi))*int((2*x*0.1)/(((1-x^2)^2)+4*0.01*x^2)*(w-x),x=-infinity..infinity,'CauchyPrincipalValue');
```

$$\text{Chi1} := -15.70796327 \frac{w^2 - 1.}{\pi(-49. w^2 + 25. w^4 + 25.)}$$

Now let's plot the result from w=-2 to 2 rad/s

```
> plot(Chi1,w=-2..2);
```



And now let's compare this result to the known value for Chi 1, by plotting for w=-2 to 2 rad/s

```
> plot((1-w^2)/(5*(((1-w^2)^2)+4*0.01*w^2)),w=-2..2);
```

